

UC San Diego

UC San Diego Electronic Theses and Dissertations

Title

Locomotion of Bioinspired Underwater Soft Robots with Structural Compliance

Permalink

<https://escholarship.org/uc/item/1vb4g3gx>

Author

Ishida, Michael

Publication Date

2022

Peer reviewed|Thesis/dissertation

UNIVERSITY OF CALIFORNIA SAN DIEGO

Locomotion of Bioinspired Underwater Soft Robots with Structural Compliance

A dissertation submitted in partial satisfaction of the
requirements for the degree Doctor of Philosophy

in

Engineering Sciences (Mechanical Engineering)

by

Michael Yoshiharu Ishida

Committee in charge:

Professor Michael T. Tolley, Chair
Professor Shengqiang Cai
Professor Nicholas Gravish
Professor Andrew J. Lucas
Professor Qiang Zhu

2022

Copyright

Michael Yoshiharu Ishida, 2022

All rights reserved.

The Dissertation of Michael Yoshiharu Ishida is approved, and it is acceptable in quality and form for publication on microfilm and electronically.

University of California San Diego

2022

DEDICATION

This dissertation is dedicated to the friends we made along the way, which are essential to any successful piece of research.

EPIGRAPH

Every generation has the obligation to free men's minds for a look at new worlds ... to look out from a higher plateau than the last generation. Your vision is not limited by what your eye can see, but what your mind can imagine. If you accept these past accomplishments as commonplace, then think of the new horizons that you can explore. ... Make your life count, and the world will be a better place because you tried.

Ellison Onizuka

Life shrinks or expands in proportion to one's courage.

Anais Nin

The moving finger writes, and having writ moves on: not all thy piety nor wit shall lure it back to cancel half a line, no all thy tears wash out a word of it.

Omar Khayyam (Rubaiyat)

TABLE OF CONTENTS

Dissertation Approval Page	iii
Dedication	iv
Epigraph	v
Table of Contents	vi
List of Figures	viii
Acknowledgements	x
Vita	xii
Abstract of the Dissertation	xiii
Chapter 1 Introduction	1
Chapter 2 Review of Soft Actuation for Soft Underwater Robots	8
2.1 Actuation in Soft Robotics	8
2.1.1 Soft Materials Actuated by Tendons	8
2.1.2 Fluidic Elastomer Actuators	10
2.1.3 Smart Materials	11
2.1.4 Stiffness Modulation	12
2.1.5 Actuator Characteristics and Selection	12
2.2 Crawling and Swimming in Soft Underwater Robots	14
2.2.1 Crawling	16
2.2.2 Swimming	19
Chapter 3 Morphing Structure for Changing Hydrodynamic Characteristics of a Soft Underwater Walking Robot	28
3.1 Introduction	29
3.2 Robot Design	32
3.2.1 Hydrodynamic Model	32
3.2.2 Robot Components	33
3.3 Methods	35
3.3.1 Water Channel and Flow Generator	35
3.3.2 Measurement	37
3.4 Experimental Results and Discussion	38
3.4.1 Static Characterization	38
3.4.2 Robot Traction	40
3.4.3 Robot Speed	40
3.4.4 Active Body Morphing	41

3.5	Conclusions and Future Work	41
Chapter 4	Tuning the morphology of suction discs to enable directional adhesion for locomotion in wet environments	44
4.1	Introduction	45
4.2	Results and Discussion	49
4.2.1	Testing two mechanisms for directional adhesion.....	49
4.2.2	Contact mechanics at discrete angles during loading	58
4.2.3	Modeling mechanics and contact throughout a gait cycle	60
4.2.4	Adhesion-enabled locomotion	64
4.3	Conclusion	69
4.4	Materials and Methods	70
4.4.1	Fabrication of the discs	70
4.4.2	Experimental evaluation of adhesion	72
4.4.3	Imaging contact	72
4.4.4	Modeling the mechanics of directional adhesion	73
4.4.5	Demonstration of locomotive application	74
Chapter 5	Locomotion via active suction in a sea star-inspired soft robot	77
5.1	Introduction	78
5.2	Actuator Design and Fabrication	81
5.2.1	Design and fabrication of suction discs	81
5.2.2	Design of tube foot actuators	83
5.3	Experimental Results and Discussion	85
5.3.1	Importance of actuator force	85
5.3.2	Characterization of adhesion of suction discs with active suction applied	87
5.4	Applications for a Walking Robot	90
5.5	Conclusions and Future Work	95
Chapter 6	Vectored thrust of a cephalopod-inspired jetting robot with a soft nozzle... ..	97
6.1	Introduction	97
6.2	Robot Design and Fabrication	100
6.2.1	Actuated Flexible Nozzle	100
6.2.2	Drivetrain	102
6.3	Experimental Results and Discussion	103
6.3.1	Characterization of the Nozzle	103
6.3.2	Characterization of the Transmission System	107
6.3.3	Mechanisms Incorporated on a Robot	108
6.4	Conclusions and Future Work	108
Chapter 7	Conclusions	109
7.1	Future Directions	111
	Bibliography	114

LIST OF FIGURES

Figure 1.1.	Crawling modes observed in animals.	3
Figure 1.2.	Swimming modes observed in animals.	4
Figure 1.3.	Crawling modes observed in animals.	5
Figure 2.1.	Soft actuators demonstrated for underwater robots.	9
Figure 2.2.	Plot of the relationship between system velocity and locomotion efficiency.	15
Figure 3.1.	Soft quadruped robot for walking underwater with morphing body that changes shape to be more hydrodynamically advantageous based on force sensor readings.	29
Figure 3.2.	Images of robot design. a) Image of the soft quadruped with morphing body. b) Schematic of the hydraulic system in which four three-way valves inflate and vent the legs and a volumetrically-controlled syringe pump inflates and deflates the morphing structure.	34
Figure 3.3.	Diagrams of the water channel and load cell.	36
Figure 3.4.	Visualization of flow from left to right over the stationary robot with different body configurations.	36
Figure 3.5.	Comparison of lift and drag on the robot at low, medium, and high flow speeds and measurements of critical velocity and walking speed.	39
Figure 3.6.	The robot with force sensor detecting increased flow and morphing its body to compensate.	42
Figure 4.1.	Tuning morphology for directional adhesion. Design parameters of a suction disc cause an adhesive force that is highly dependant on the direction of loading.	50
Figure 4.2.	Experimental investigation into the morphological parameters for anisotropic adhesion.	51
Figure 4.3.	Visualizing the contact between a suction disc and a surface.	59
Figure 4.4.	Finite Element Analysis to model the mechanics of adhesion of a suction disc while attached at various angles of attachment and detachment.	61
Figure 4.5.	Employing suction discs for sea star inspired adhesion-based locomotion.	65

Figure 4.6.	Demonstration of the use of directional adhesion in multi-legged sea star inspired locomotion.	67
Figure 4.7.	Fabrication of the suction discs.	71
Figure 4.8.	Experimental setup for characterization of adhesion.	75
Figure 5.1.	Biological inspiration and experimental prototypes for robot capable of locomotion using an array of soft tube feet.	79
Figure 5.2.	Characterization of the two types of tube foot actuators.	82
Figure 5.3.	Characterization of the adhesion of the active suction discs.	88
Figure 5.4.	Characterization of the adhesion of an active suction discs to a rough surface.	90
Figure 5.5.	Experimental setup for the walking robot.	91
Figure 5.6.	Characterization of the walking behavior of the robot with a simple traveling wave gait.	93
Figure 5.7.	Demonstration of the locomoting robot walking through a confined space between a rail above it and an acrylic surface below it.	94
Figure 6.1.	Experimental prototype and biological inspiration for a jet-propelled swimmer.	98
Figure 6.2.	Schematic of the robot, soft nozzle, and waterproof motor enclosures.	101
Figure 6.3.	Characterization of the bending of the nozzle.	104
Figure 6.4.	Quantification of losses in flow through the soft nozzle and other designs.	105
Figure 6.5.	Characterization of the magnetic coupling for the waterproof servo enclosures.	106
Figure 6.6.	Characterization of the cam that drove the compression of the body.	107

ACKNOWLEDGEMENTS

I would like to acknowledge my committee for their advice and support throughout my time at UCSD. I am especially grateful to my advisor Prof. Mike Tolley for giving me the opportunity to transition from the master's program to the PhD program as well as his mentorship for 6+ years. I would also like to acknowledge Mark Hermes and Prof. Mitul Luhar for being huge collaborators on several projects within the Starbot grant.

My PhD experience would not have been possible without the help and support from my labmates in the Bioinspired Robotics and Design Lab. I would like to acknowledge Jess and Saurabh from my PhD cohort, the PhDs from BRDL 1.0 (Caleb, Dylan, Ben, Adriane, Will, Paul), and Iman and Jiayao. Other shoutouts to Matt and Francis from my MS cohort and all the undergraduate researchers I had the pleasure to work with, especially Sebastian, Billy, Sidney, Ayush, Jayden, and Allyson.

I would like to acknowledge my friends who made my time at UCSD so enjoyable. A special acknowledgement to Chris Morrison, who mentored me on my first academic research project at RPI, Ben Magolan, who convinced me to apply to graduate programs, and to Deepak Trivedi, who introduced me to the field of soft robotics. Other acknowledgements go to my friends James, Lysha, Kevin, April, Alistair, Kayla, Connor, Jason, Shivam who were all a big part of my time in San Diego.

And I'd like to give a final acknowledgement to my family for their unwavering support.

Chapter 1, in part, is a reprint of the material as it appears in: Hermes, M.*, Ishida, M.*, Luhar, M., Tolley, M. T. (2020), "Bioinspired Shape-Changing Soft Robots for Underwater Locomotion: Actuation and Optimization for Crawling and Swimming", In Paley, D. A., Wereley, N. M. (Eds.), *Bioinspired Sensing, Actuation, and Control in Underwater Soft Robotic Systems* (pp. 7-39). The dissertation author was the co-primary investigator and co-first author of the sections of the paper that are reprinted in this chapter.

Chapter 2, in full, is a reprint of the material as it appears in: Hermes, M.*, Ishida, M.*, Luhar, M., Tolley, M. T. (2020), "Bioinspired Shape-Changing Soft Robots for Underwater

Locomotion: Actuation and Optimization for Crawling and Swimming”, In Paley, D. A., Wereley, N. M. (Eds.), *Bioinspired Sensing, Actuation, and Control in Underwater Soft Robotic Systems* (pp. 7-39). The dissertation author was the co-primary investigator and co-first author of the sections of the paper that are reprinted in this chapter.

Chapter 3, in full, is a reprint of the material as it appears in: Ishida M., Drotman D., Shih B., Hermes M., Luhar M., and Tolley M. T. (2019), ”Morphing structure for changing hydrodynamic characteristics of a soft robot walking underwater”, *IEEE Robotics and Automation Letters*, 4 (4), 4163-4169. The dissertation author was the primary investigator and author of this paper.

Chapter 4, in full, is a reprint of the material as it appears in: Sandoval J. A.*, Ishida M.*, Jadhav S., Huen S., Tolley M. T. (2022) ”Tuning the morphology of suction discs to enable directional adhesion for locomotion in wet environments”, *Soft Robotics*, in press. The dissertation author was the co-primary investigator and co-first author of this paper.

Chapter 5, in full, is a reprint of the material as it appears in: Ishida M., Sandoval J. A., Lee S., Huen S., Tolley M. T. (2022) ”Locomotion via active suction in a sea star-inspired soft robot”, *IEEE Robotics and Automation Letters/IROS*, 7 (4), 10304-10311. The dissertation author was the primary investigator and author of this paper.

Chapter 6, in part, is currently being prepared for submission for publication of the material: Ishida M., Wood J., Gaggar A., Tolley, Michael T. ”Vectored thrust of a cephalopod-inspired jetting robot with a soft nozzle”. The dissertation author was the primary investigator and author of this paper.

Chapter 7, in part, is a reprint of the material as it appears in: Hermes, M.*, Ishida, M.*, Luhar, M., Tolley, M. T. (2020), ”Bioinspired Shape-Changing Soft Robots for Underwater Locomotion: Actuation and Optimization for Crawling and Swimming”, In Paley, D. A., Wereley, N. M. (Eds.), *Bioinspired Sensing, Actuation, and Control in Underwater Soft Robotic Systems* (pp. 7-39). The dissertation author was the co-primary investigator and co-first author of the sections of the paper that are reprinted in this chapter.

VITA

- 2016 Bachelor of Science, Rensselaer Polytechnic Institute
- 2018 Masters of Science, University of California San Diego
- 2018–2019 Teaching Assistant, Department of Mechanical Engineering
University of California San Diego
- 2019–2022 National Defense Science and Engineering (NDSEG) Fellow
- 2022 Research Assistant, University of California San Diego
- 2022 Doctor of Philosophy, University of California San Diego

PUBLICATIONS

Ishida M., Drotman D., Shih B., Hermes M., Luhar M., and Tolley M. T. (2019), "Morphing structure for changing hydrodynamic characteristics of a soft robot walking underwater", *IEEE Robotics and Automation Letters*, 4 (4), 4163-4169.

Hermes, M.*, **Ishida, M.***, Luhar, M., Tolley, M. T. (2020), "Bioinspired Shape-Changing Soft Robots for Underwater Locomotion: Actuation and Optimization for Crawling and Swimming", In Paley, D. A., Wereley, N. M. (Eds.), *Bioinspired Sensing, Actuation, and Control in Underwater Soft Robotic Systems* (pp. 7-39).

Sandoval J. A.*, **Ishida M.***, Jadhav S., Huen S., Tolley M. T. (2022) "Tuning the morphology of suction discs to enable directional adhesion for locomotion in wet environments", *Soft Robotics*, in press.

Ishida M., Sandoval J. A., Lee S., Huen S., Tolley M. T. (2022) "Locomotion via active suction in a sea star-inspired soft robot", *IEEE Robotics and Automation Letters/IROS*, 7 (4), 10304-10311.

ABSTRACT OF THE DISSERTATION

Locomotion of Bioinspired Underwater Soft Robots with Structural Compliance

by

Michael Yoshiharu Ishida

Doctor of Philosophy in Engineering Sciences (Mechanical Engineering)

University of California San Diego, 2022

Professor Michael T. Tolley, Chair

Mobile robots are commonly used to perform tasks in underwater environments that are difficult for humans to endure, such as exploration, long-duration measurements, or maintenance and repair of underwater structures. Traditional underwater robots are often bulky and disruptive to the environment around it and are often adapted from engineered systems that were designed for operation in air. However, the underwater fluid environment is significantly different from the in-air environment and motivates the development of new robot paradigms specifically to address the challenges that arise from the surrounding water. I have taken inspiration from nature, which has evolved fast and efficient mechanisms for underwater locomotion, to design soft, bioinspired walking and swimming robots.

In this work, I have explored several ways to design mobile robots specifically for the underwater fluid environment. To mitigate the negative effects of flow on an underwater walking robot, I created a soft inflatable structure that can be attached to the robot to alter the lift and drag forces on the robot and increase traction in flow. To create locomotion independent of the flow on the robot, I designed soft suction discs and soft linear actuators that enable adhesive-based locomotion. By leveraging interactions with fluid, I created a steerable, shape-changing robot that uses vectored jet propulsion to swim through open water. This work has the potential to enable more efficient locomotion in underwater environments more closely resembling the capabilities of biological systems.

Chapter 1

Introduction

The underwater domain is one of the most hostile environments for both humans and engineered systems. To explore these hard-to-reach regions, engineers have created robust and powerful remotely operated vehicles (ROVs) and autonomous underwater vehicles (AUVs). Although these existing systems are well-suited to moving quickly through open water, they are often noisy, exhibit high energy consumption, and are rigid, thus unable to move through tight confined spaces or interact with fragile objects or organisms [1]. To address these problems, we take inspiration from nature. Animals are quiet to avoid predation, energy efficient to reduce the amount of food required to survive, and can use their bodies' compliance to squeeze through tight openings. Although traditional robotics systems are capable of fast and precise motions, they are not well-suited to mimic or reproduce biologically inspired motions because of their lack of flexibility. Soft robotics systems, on the other hand, can create continuous deformations to produce motions that are highly adaptable to changing and unpredictable environmental situations [2]. For this reason, there is a wide overlap between soft robotics and bioinspired robotics.

Soft materials are characterized by low hardness and high elasticity, which can be used for shape-changing behavior. The material properties of the components differentiate soft robotics from traditional rigid robotics. Soft materials have a bulk elastic moduli in the $10^4 - 10^9$ Pa range, similar to those of soft biological materials (i.e., muscle, cartilage, etc), whereas materials used

in traditional robotics have moduli that are generally at or greater than 10^9 Pa (e.g., aluminum, 10^{10} Pa). Deformable structures and stiffness-changing mechanisms, both of which partially consist of rigid materials can also exhibit soft properties in bulk. Thus, soft robots are systems that create autonomous, controllable motions using actuators made of soft materials or with composite structures made of rigid materials that have macroscopic properties similar to those of soft materials [3]. Some underwater organisms such as sea cucumbers consist of only soft materials, which motivates the use of soft materials for creating robots inspired by biology.

Another advantage of a soft robot is that it can change the shape of its body to create advantageous interactions with the surrounding fluid environments. A robot or organism with a soft interface between the inner body and the fluid environment can change macroscopic shape in one of the following ways: 1) by changing its volume e.g., intaking water and expanding and 2) by changing the geometry of its body without changing its volume e.g., undulating the body or rowing with flippers. However, a rigid system can produce similar categories of shape changes: 1) changing its volume by extending an appendage from an internal geometry and 2) changing the geometry of its body by rotating joints between rigid links. However, these examples would not result in continuous deformation in the surfaces interacting with the surrounding fluid, distinguishing it from soft shape changes. Actuators that can continuously deform can create smoother surfaces in contact with flow, which often produces fewer detrimental vortices and flow patterns.

Shape change is a useful mechanism for enhancing or coordinating locomotion through a fluid. We distinguish two primary methods of moving through a fluid: crawling and swimming. The characteristic difference between the two is the presence or absence of interaction with a substrate. Crawling requires a body to be partially attached to semi-solid objects, such as sand or coral. Crawling in nature is accomplished by a synchronous cyclic motion of appendages, exemplified by crustaceans and echinoderms (Fig. 1.1). This strategy has the benefit of continuous attachment to the substrate during locomotion, which reduces the need to control motion perpendicular from the surface e.g., motion vertically through the water column. In

addition, if an organism is moving within a low-velocity boundary layer on the seafloor, assuming the effect from shear stress is minimal compared to drag, crawling can reduce the drag and lift forces from moving in flow. These characteristics aid the stability of the locomotion, but comes at the cost of speed.


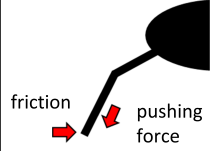
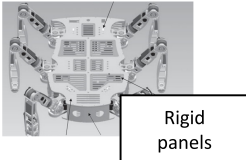

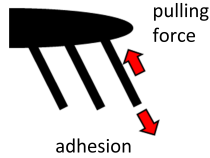

Type of locomotion	Description	Animal	Schematic	Robot
Friction-based crawling (discrete)	<ul style="list-style-type: none"> Friction between appendage and substrate allows appendage to push body Maximum friction force is affected by lift and buoyancy Discretized actuation 	Crustaceans 		Rigid crab-like hexapod 
Adhesion-based crawling (distributed)	<ul style="list-style-type: none"> Adhesion between appendage and substrate allows appendage to pull body Maximum adhesive force is not affected by lift and buoyancy Distributed actuation 	Echinoderms 		Echinoderm-inspired tube feet 

Figure 1.1. Crawling modes observed in animals. Friction-based crawling uses a pushing motion caused by friction between an appendage and the substrate. Adhesion-based crawling creates a separate force, e.g., suction or chemical; to create a pulling motion between the appendage and the substrate. Citations for right-most column: [4], [5]

Natural swimming modes are diverse and make use of a range of different hydrodynamic phenomena, including vortex shedding, jetting, and drag-based propulsion (Fig. 1.2). Swimming is a faster method of locomotion than crawling, but requires control of all six degrees of freedom (three translational and two rotational) instead of three degrees of freedom required for planar crawling motions (two translational and one rotational). However, legged crawling results in a larger configuration space for the robot than swimming does as crawling usually requires multiple legs with multiple degrees of freedom. In addition, swimming often requires energy expenditure to maintain a position in unobstructed flow, rather than using passive friction with a substrate.

Many previous underwater robots have focused on robust operation in murky sea water.



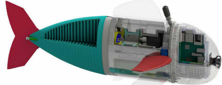


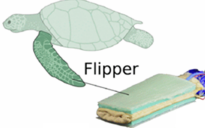




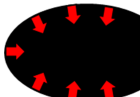
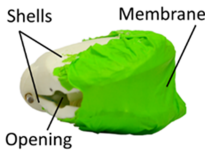
Type of locomotion	Description	Animal	Schematic	Robot
Rear-body undulation	<ul style="list-style-type: none"> Observed in carangiform, sub-carangiform, thunniform, ostraciiform Thrust generated by reverse von Karman street vortex shedding Oscillating motion of tails, flippers 	Cetaceans, most fish 		Soft robotic fish (SoFi) 
Full-body undulation	<ul style="list-style-type: none"> Otherwise named anguilliform swimming Traveling wave produced along entire body accelerates fluid for a net forward thrust Slower motions produced compared to rear-body undulators 	Eels, manta ray pectoral fins 		Eel-inspired soft robot 
Drag-induced swimming	<ul style="list-style-type: none"> Oar-like appendage Thrust generated by drag force opposing direction of motion of appendage Appendage changes orientation to minimize reverse thrust during the recovery stroke. 	Duck, platypus, freshwater turtle 		Turtle-inspired limb 
Jet propulsion	<ul style="list-style-type: none"> Water jet out of rear nozzle Thrust generated by momentum conservation Changing volume of the body increases acceleration via added mass effect 	Jellyfish, octopus 		Scallop-inspired robot 

Figure 1.2. Swimming modes observed in animals. Rear-body undulation and full-body undulation generates thrust through vortex shedding. Drag-induced swimming occurs by exploiting direction dependent drag control. Jet-based swimming is seen in organisms that eject water through a cavity. Citations for right-most column: [6], [7], [8], [9]

However, this means there is a large opportunity to create soft and shape-changing robots that can take advantage of the underwater environment. Traditional robots use dense and heavy materials to create traction and high-strength actuators to withstand lateral forces from currents. On the other hand, soft and bioinspired robots can create favorable interactions with the surrounding environment. Soft, shape changing robots can alter their lift and drag profiles to create more efficient locomotion in changing flow conditions. In addition, soft materials can enable robots to create motions that are more similar to the motions made by animals.

In this dissertation, I explore three different bioinspired locomotion paradigms that are important when designing soft robots for underwater environments: locomotion resisting fluid forces, locomotion independent of fluid forces, and locomotion leveraging fluid forces. These research themes are depicted in Fig. 1.3.

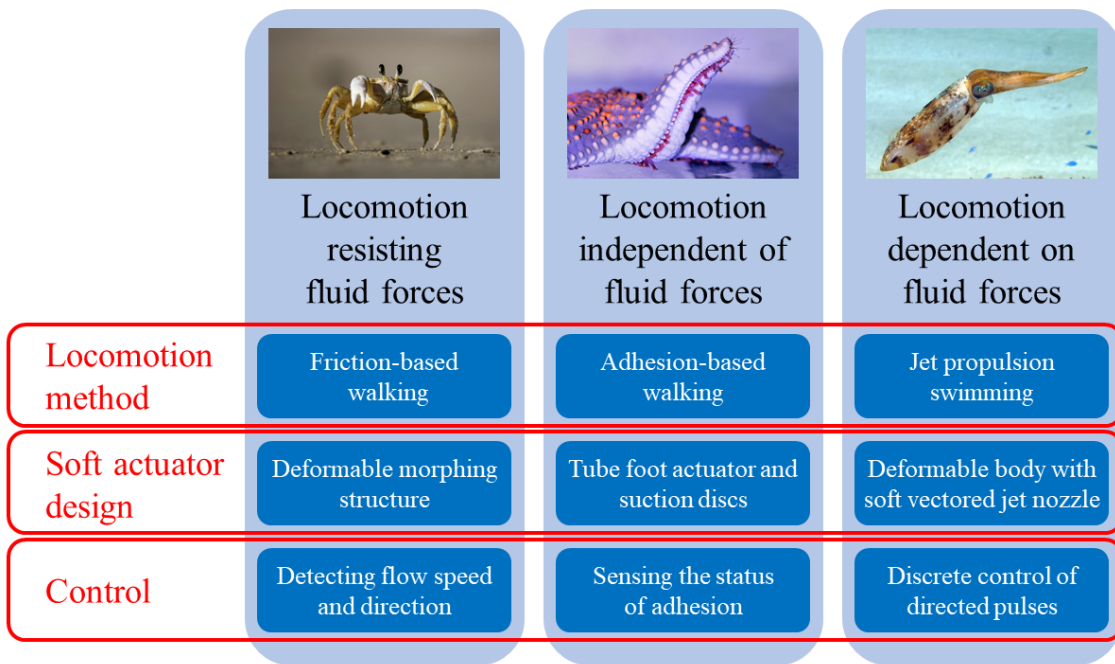


Figure 1.3. Crawling modes observed in animals. Friction-based crawling uses a pushing motion caused by friction between an appendage and the substrate. Adhesion-based crawling creates a separate force, e.g., suction or chemical; to create a pulling motion between the appendage and the substrate. Citations for right-most column: [4], [5]

First, I investigated how simple, morphing structures could improve the performance of a

walking robot by increasing its resistance to the negative effects of fluid flow. The robot, designed for operation on land, uses friction to create traction with the ground for locomotion. However, when placed underwater, that friction is reduced because of upward forces like buoyancy and lift. Instead of adding more mass to the robot to increase its weight and traction at the cost of adding more inertia and creating more compression of the legs, I designed a structure that changed the hydrodynamic profile of the robot. Inflating the structure in one way increased the downward lift on the robot to provide more traction when walking against flow. Inflating the structure in a different way increased the upward lift and the drag to act like a sail when walking in the same direction as flow. The robot also included a flow sensor that could sense the magnitude of the flow to determine whether it was more advantageous to inflate or deflate the morphing structure.

Next, I examined adhesion-based walking of soft robots, a strategy that has the potential to create locomotion independent of the fluid forces on a robot. As shown in the previous chapter and in previous work, a robot that relies on friction for locomotion can be highly susceptible to flow or vortices that can be highly variable in both direction and magnitude. In contrast, a robot that uses adhesion to create attachment to a substrate instead of friction is much less affected by the flow field around it since the adhesion strength is not dependent on the hydrodynamic forces on the robot. Here, I took inspiration for a walking robot from echinoderms such as sea stars that have unique locomotion capabilities enabled by the hydraulic tube foot appendages on the underside of their bodies.

The sea star's adhesive-based locomotion is enabled by its large array of many adhesive tube feet. To translate this to a practical robotic system, each tube foot actuator would require a mechanism to engage adhesion at the start of a step and to disengage the adhesion at the end of the step to allow the actuator to retract. Including this capability as a controlled degree of freedom in a fluidic soft robot would double the total number of control lines, making it difficult to create a robot with many tube foot actuators. Expanding on previous work, I showed that asymmetric soft suction discs can be used to create adhesion that is dependent on the direction at which the pull-off load is applied. Thus, the actuator had high adhesion when loaded in one

direction at the start of a step and had low adhesion when loaded in the other direction at the end of a step. This embodied intelligence in the adhesive element of the tube foot modules reduced the fluidic control complexity for controlling a simple walking gait by programming the attachment and detachment conditions into the morphology of the suction discs.

In addition, I combined soft suction discs with soft linear actuators to create a walking motion inspired by sea stars. This work moves away from the asymmetric suction discs to symmetric suction discs with active vacuum lines. This was necessary to enable the use of soft linear actuators as the active vacuum lines that create negative pressure in the suction discs reduce the need for the soft actuators to press the discs into the substrate to engage adhesion. By using a set of these combined adhesion and actuation modules in one robotic system, I showed that having an array of simple actuators can create locomotion that is robust to failures of individual modules, which allows the robot to traverse small obstacles.

Finally, I looked at ways to leverage the fluid forces to create a maneuverable swimming robot using jet propulsion. Inspired by the squid,

Chapter 1, in part, is a reprint of the material as it appears in: Hermes, M.*, Ishida, M.*, Luhar, M., Tolley, M. T. (2020), "Bioinspired Shape-Changing Soft Robots for Underwater Locomotion: Actuation and Optimization for Crawling and Swimming", In Paley, D. A., Wereley, N. M. (Eds.), *Bioinspired Sensing, Actuation, and Control in Underwater Soft Robotic Systems* (pp. 7-39). The dissertation author was the co-primary investigator and co-first author of the sections of the paper that are reprinted in this chapter.

Chapter 2

Review of Soft Actuation for Soft Underwater Robots

2.1 Actuation in Soft Robotics

Soft robots are distinguished from rigid or traditional robots by the compliance of their constituent materials. These soft materials can perform continuum motions that allow them to form complex shapes, make large deformations, and use their passive material properties to adapt to their environment. Actuators made from soft materials have similar elastic moduli to soft biological tissues such as skin or muscle and are more suitable than rigid structures to mimic biological materials [3]. We previously distinguished soft materials from rigid materials through the use of elastic modulus, where in general soft materials fall between 10^4 and 10^9 Pa as compared to rigid materials, which have moduli from 10^9 Pa and above. This section details common soft actuators that can be used to create shape changes and shows examples of these actuators applied to soft robots for underwater applications or inspired by aquatic animals.

2.1.1 Soft Materials Actuated by Tendons

Tendon-driven soft robots consist of a soft material with tendon-like cables anchored at various points within the bulk material. The tendons are then connected to an actuator at the base of the soft material. When the actuator at the base applies tension to the cable, it pulls the anchoring point toward the base, causing the desired deformation [15]. The base actuator that

Type of soft actuator and previous uses	Description	Schematic	Robot
Tendon-driven Carangiform-swimming	<ul style="list-style-type: none"> Bulk soft material pulled by a cable Cable actuated by motors, smart materials, or other soft linear actuators Good for high power applications 		Robotic fish
Fluidic elastomer: pneumatic network carangiform-swimming, jetting	<ul style="list-style-type: none"> Pressure input causes deformation constrained by inextensible layer Commonly used to create bending Requires heavy valves and pumps 		Soft robotic fish (So-Fi)
Fluidic elastomer: bellows friction-based crawling	<ul style="list-style-type: none"> Pressure input causes linear deformation from unfolding material Bellows can use materials with low strain Requires heavy valves and pumps 		Soft walking robot
Smart material: dielectric elastomer anguilliform-swimming, carangiform-swimming, jetting	<ul style="list-style-type: none"> Maxwell stress causes compression in one plane and extension in the other Including a strain-limiting layer causes the actuator to bend High efficiency but requires high voltage and thin composite layers 		Soft eel-inspired robot
Smart material: shape memory alloy friction-based crawling	<ul style="list-style-type: none"> Deformable at low temperatures, Restores to a trained shape at high temperatures Lightweight but has significant time delays due to cooling 		Soft starfish-inspired robot
Smart material: liquid crystal elastomer Distributed-crawling	<ul style="list-style-type: none"> External stimulus changes cross-linking in polymer, creating deformation Easily reversible Small form-factor, actuation slow to reverse without heat sink 		Soft echinoderm-inspired robot

Figure 2.1. Soft actuators demonstrated for underwater robots. Tendon-driven actuators use a bulk soft material actuated through tension. Pneumatic networks create bending using inflation constrained by a strain-limiting layer. Bellows produce an extending motion when pressurized as the material unfolds. Dielectric elastomers use Maxwell stress to create deformation in multiple planes. Shape memory alloys and liquid crystal elastomers use heat to trigger deformation. Citations for right column: [10], [6], [11], [12], [13], [14].

pulls the tendon is often a traditional electromechanical component like a motor that can provide large forces [10], which can provide significant velocity or power while the bulk soft material produces continuum deformation or passive compliance. The electromechanical component can alternatively be replaced with a soft linear actuator [16] or smart material [17] to reduce the rigid components required. If a soft surface is attached to tendons at discrete nodes, displacement of the tendons creates a corresponding displacement of the node in a direction determined by the tendon routing. The known displacement of the node can allow control of the surface shape via a model of the soft surface's deformation [18].

2.1.2 Fluidic Elastomer Actuators

Fluidic elastomer actuators (FEAs) are a class of soft actuators powered by fluid pressure [19]. These actuators consist of a hyperelastic material with one or more internal cavities into which fluid pressure is applied and can be fabricated by through a molding and curing process [20] or by directly 3D printing the soft material [21] [22]. Constraining elements like fibers or sheets are made from flexible but inextensible materials and pattern the deformation of the actuators (Fig. 2.1). When the constraining elements are asymmetric, the actuator creates a bending or twisting motion e.g., pneumatic networks that bend toward an inextensible layer as the extensible material stretches [23]. Bending actuators can be used to change the shape of a soft robot from a flat contour to a curved surface. When the elements are symmetric, it creates an elongating or contracting motion e.g., fiber-reinforced actuators that extend axially without expanding radially [24]. Extension or contraction actuators are used as artificial muscles in shape-changing mechanisms as they can change the height of nodes in an array to actively create a predictable surface [25].

Other fluidic actuators forgo an inextensible constraining layer to create unique geometries and motions. Bellowed fluidic actuators have no constraining layer and take advantage of the folding and unfolding of the bellows when pressure is applied to create contraction and extension with minimal straining of the material [26] [27]. Soft tentacles use multiple fluid channels in

the bulk cylindrical elastomer cast around a stiffer elastomer core to creating a complex coiling motion when pressurized [28]. Pouch motors take advantage of laminate fabrication methods and can be used to create either a linear motion or a rotational motion around a joint [29]. Inflating a soft pouch can also be used to alter the shape of a body interacting with flow [11].

2.1.3 Smart Materials

Smart materials are a broad class of materials with properties that respond to an external stimulus such as heat or electrical fields. Those that are capable of significant deformation or stiffness change with a controllable and localizable stimulus can be used to create motion. Smart materials can be soft themselves or alternatively used to actuate soft materials. To create a complete actuator, the smart materials are packaged with components that provide the controllable stimulus, such as an embedded heater, a light source, or a high voltage supply [30].

Dielectric elastomer actuators (DEAs) are a type of smart material that uses Maxwell stress to create deformation in a soft material [31]. A soft dielectric polymer is sandwiched between two compliant electrodes, which can be made from conductive metals [32], polymers [31], and fluids [12]. When a voltage is applied to the electrodes, the voltage differential causes the Maxwell stress to compress the elastomer, creating planar extension in both directions perpendicular to the compression direction. The compression force is a function of the dielectric constant, the applied voltage, and thickness of the layer. A DEA can use either or both the compression force [33] and the stretching motion to create actuation [34]. The planar expansion of DEAs can be used to create shape change in similar ways to the FEAs. The inclusion of a flexible but inextensible layer creates a bending motion and can change the shape of a curve interacting with flow [35].

Other smart materials use thermal energy to drive actuation, often created electrically using Joule heating. Shape memory alloys (SMA) are materials that are programmed to deform to a certain shape or pattern at high temperatures. When heat is removed, these materials then restore to the unactuated shape (usually a minimal restoring force is required) [36]. Shape

memory polymers (SMP) are a class of polymer-based soft materials that typically deform under a heat stimulus, but are often not able to restore to the unactuated state without additional energy input [30]. Liquid crystal elastomers (LCE) are networks of polymers that organize their structure in predetermined orientations when a temperature threshold is met. This deformation is reversible, as the polymer will return to the original configuration when temperature is decreased [37]. These materials are coupled with resistive heating elements that create the controllable temperature change needed for actuation.

2.1.4 Stiffness Modulation

Active stiffness modulation couples actuation with controllable material properties that can be adjusted on a short time scale. Tunable stiffness can be accomplished by creating a phase change in the actuator materials e.g., by using embedded heaters to melt a thermoplastic material, thereby softening the actuator [38] [39]. Pressure-induced tunable stiffness, also called jamming, can be accomplished by applying a negative pressure to small granules or high-friction layers within a membrane. This compresses the constituent materials together creating an effective phase change from a fluid-like to a solid-like bulk material. Previous work has shown the use of jamming actuators for applications such as locomotion [40], haptic feedback [41], and a shape-changing surface [42]. Magnetic field-induced tunable stiffness can be accomplished by subjecting an elastomer with dispersed magnetic particles to a magnetic field, creating a change in stiffness [43]. These stiffness-changing mechanisms cannot create a shape change by themselves, but can be useful alongside the previous actuators. Active control of the stiffness of the surface allows it to be either deformable when the surface must change from one shape to another or rigid when the surface must withstand external forces.

2.1.5 Actuator Characteristics and Selection

The wide range of soft robotic actuators have different properties and each type of actuator is suitable for different applications (see Fig. 2.1). Tendon-driven components are often directly

actuated by traditional electromechanical actuators like motors and servos, which can give them higher power relative to other soft actuators. However, the electromechanical components are generally bulky and heavy and the tendon routing becomes complex for actuators with many degrees of freedom. In addition, tendons pulling on a soft material often create deformations local to the tendon anchoring point rather than distributed along the continuum, which is not beneficial for operation in fluid. Fluidic elastomer actuators balance efficiency with speed and power, but similarly require valves and pumps, which are typically rigid, heavy and expensive. Jamming actuators are well-suited for using stiffness to hold a position, but often require another actuator to create the motion to transfer between different states. Both of these actuation strategies require changing the amount of fluid in the actuator; for operation underwater, this generally necessitates using oil or water to maintain a constant buoyancy.

Smart materials have different strengths and challenges since they do not require the same electromechanical actuators like motors or pumps. Dielectric elastomers are capable of rapid actuation and can create large strains. To create high efficiency with a DEA, the actuator requires high voltage and a thin membrane that is susceptible to puncture. These require soft electrodes that can be challenging to fabricate, so robots designed for underwater operation have capitalized on the surrounding fluid to create electrodes [7]. Shape memory alloys are often challenging to fabricate and train. Although shape memory polymers can be relatively easy to fabricate, they usually do not create reversible deformations, requiring energy input for restoration to their original position. Liquid crystal elastomer actuators create reversible motions, but can exhibit hysteresis and low actuator bandwidth due to the thermal actuation. When operated underwater, both SMA and LCE actuators benefit from increased cooling rates (shorter relaxation time) due to the heat transfer with the water, at the cost of slower heating rates (longer actuation time). The success of a soft robot is greatly dependent on the matching of the actuation type to the application and the corresponding advantages or disadvantages as discussed here.

2.2 Crawling and Swimming in Soft Underwater Robots

We characterize underwater locomotion broadly into swimming and crawling. As defined in Section 1, crawling occurs when a body remains in contact with a substrate (see Fig. 1.1), whereas swimming relies on hydrodynamic forces for propulsion. We further classify swimming based on the mechanism used for thrust generation: jetting, appendage-based propulsion, and undulatory swimming, which generally relies on the generation of vortices (Fig. 1.2). Many propulsive strategies in nature are characterized by deforming a soft continuum surface that interacts with the fluid environment. Using these soft materials often leverages the elasticity of the material to reduce energy consumption during the recovery portions of the robot’s or animal’s gait [44]. In addition, the soft actuators produce continuum surfaces that are more desirable for interacting with flow than sharp edges. Thus, application of new soft technologies can enhance and optimize motion for underwater travel. Animals have inspired many underwater soft robots, which have reproduced characteristic locomotion methods with varying degrees of success (see Fig. 2.2).

Here we plot locomotion efficiency against overall system velocity. Efficiency is defined as the reciprocal of cost of transport (COT), a commonly-used metric for quantifying the effectiveness of biological locomotion techniques:

$$efficiency = \frac{1}{COT} = \frac{mv}{P}, \quad (2.1)$$

where m , v , and P are the animal or robot mass, velocity, and power input, respectively. In general, animals are both faster and more efficient than their robotic counterparts with the exception of commercially-available propeller-driven crafts. These large scale systems such as submarines, AUVs, and ROVs can reach high speeds and efficiencies through large power usage. The penalty for high power usage in the cost of transport metric can be offset if the robot is moving a large amount of mass or at a high velocity. Furthermore, these propeller-driven systems are established

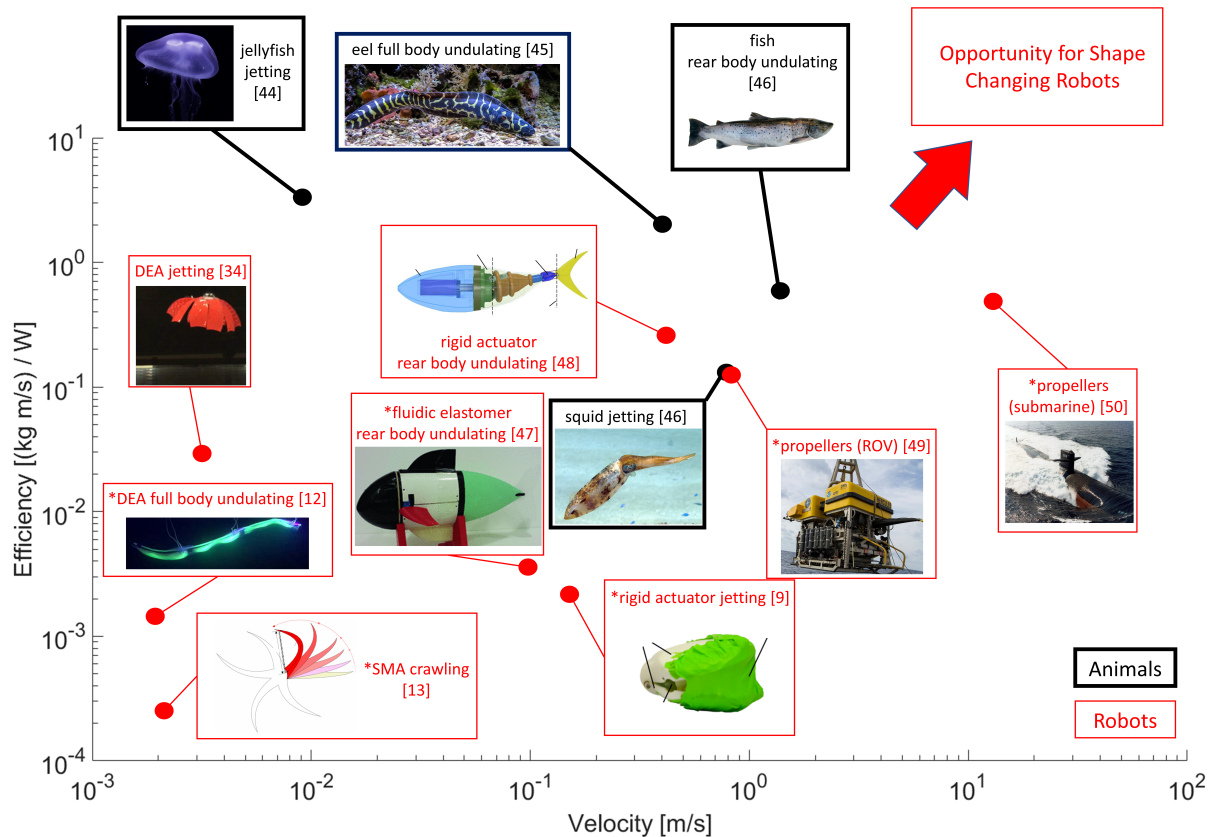


Figure 2.2. Plot of the relationship between system velocity and locomotion efficiency defined as $1/COT$ for animals (black text and outline) and underwater robots (red text and outline). All velocity values taken directly from papers cited. Cost of transport values taken directly from papers when given; otherwise, values were calculated from other listed values or representative public data and are denoted with *. Citations for animal metrics: jellyfish [44], eel [45], squid and fish [46], all images open source. Citations for robots: DEA jetting [34], SMA crawling [13], DEA full body undulating [12], fluidic elastomer rear body undulating [47], rigid actuator jetting [9], rigid actuator rear body undulating [48], propellers (ROV) [49], propellers (submarine) [50].

technologies that powertrain and energy efficiency optimizations. However, the high efficiency and speed exhibited by animals shows the effectiveness of soft materials and bioinspired gaits at meso or small scales.

The robots that use established rigid, electromechanical actuators are in general both faster and more efficient than their soft robot counterparts. While rigid swimming robots currently outperform soft robots, this is not necessarily an indictment of soft robots or the locomotion modes enabled by soft actuators. Soft robotics is a relatively new field and soft actuators are not

as developed and optimized as rigid actuators like motors. We think that with more development, soft materials can be used to create high-efficiency propulsion, especially at small and low-power scales. One example of this can be seen in the cases of jetting using soft DEAs [34] and a DC motor [9]. The jellyfish robot that uses soft actuators is 13 times more efficient than the scallop robot that uses a rigid actuator, whereas the scallop robot is 50 times faster than the jellyfish robot. This illustrates the future potential usage of soft actuators for creating efficient locomotion.

Note that the examples given are what we consider to be representative of both locomotion strategies and actuators. There are many animals and robots that employ each type of locomotion, so each example lies within a range of demonstrated efficiencies and velocities for that category. When cost of transport calculations were not included in the publications, we calculated COT using other information such electrical power or flow rate and pressure. We also acknowledge that there are other metrics that measure efficiency, such as Froude efficiency (fraction of thrust creating motion over total thrust produced) and we chose cost of transport to incorporate total input (measured by power) normalized by system size (measured by mass) and performance (measured by speed).

2.2.1 Crawling

Crawling is a common method of locomotion for both terrestrial and aquatic animals. Although there are parallels between crawling in air and water, the difference in density between the two media creates significant differences in the crawling motion. Because fluid forces such as lift and buoyancy have a lower magnitude in air than in water, terrestrial animals rely mainly on friction with a substrate to move. In contrast, underwater crawlers such as echinoderms with hydrostatic skeletons that are close to being neutrally buoyant cannot primarily rely on friction forces. In general, neutrally buoyant crawlers use adhesive actuators arranged in a distributed pattern, whereas aquatic crawlers that are not neutrally buoyant use discrete appendages and rely on friction to create a crawling motion similar to terrestrial crawlers.

Friction-based Crawling

Underwater friction-based crawling is similar to terrestrial friction-based crawling. The organism uses friction between its appendages and the substrate to push forward against the substrate. The friction between the appendage and the substrate can be modeled as $F_f = \mu N$, where μ is the coefficient of friction and N is the normal force. In terrestrial locomotion where extreme air-currents are absent, the normal force is equivalent to the weight W of the animal or robot. However, in aquatic locomotion, there are additional fluid forces to consider. The normal force includes both buoyancy $F_B = \rho V g$ and lift $\frac{1}{2}\rho C_L A U^2$, where ρ is the density of water; g is the acceleration due to gravity; V , C_L , and A are the volume, lift coefficient, and planform area of the animal or robot; and U is the velocity of the surrounding flow. So for underwater crawlers, friction is defined as

$$F_f = \mu \left(W - \rho V g - \frac{1}{2} \rho C_L A U^2 \right). \quad (2.2)$$

Friction is the force that generates locomotion. If other lateral forces opposing motion such as hydrodynamic drag or gravity (when the crawler is on a slope) are greater than the friction force, the crawler will not be able to move. Thus, to improve locomotion performance, a crawler can reduce the upward lift or buoyancy on its body or it can reduce the drag opposing its motion [11].

Crustaceans such as lobsters and crabs represent the majority of benthic animals that use friction-based crawling [51], though brittle stars and other echinoderms can produce this type of locomotion for land-based motion [52]. Since these animals rely on friction to move, they have adaptations or behaviors that influence the lift and drag on their bodies (see Eq. 2.2). In high-flow environments, crabs improve their locomotion by changing their orientations with respect to flow, thereby decreasing their drag profiles [53] and crayfish change their body posture to create downward lift (i.e., downforce) to enhance the normal force and therefore the friction at the substrate [54]. On a longer timescale, sea stars displaced from a low-flow to a high-flow

environment change the aspect ratio of their arms, perhaps because this reduces drag and lift, thus increasing the force needed to dislodge their bodies [55].

Friction-based locomotion is commonly used in underwater crawling robots. Rigid hexapods *Little Crabster* (pictured in Fig. 1.1) [4] and *AQUAROBOT* [56] were both developed for crawling along the sea floor and exploring benthic environments. Jin et al. used SMA wires to actuate soft arm actuators around a central disc to create a robot inspired by the arm motion of sea stars [17]. Cianchetti et al. created an octopus-inspired robot using cable-driven actuators that deformed soft tentacles to create a walking motion robust to varying terrains [57]. Most recently, the concept of changing body shape in flow to aid friction-based locomotion was incorporated into a fluidically actuated soft quadruped robot using a morphing body capable of adjusting lift and drag [11]. The continuous deformation created by soft actuators allows the robot to change its buoyancy (by changing its volume), its lift (changing its area and lift coefficient), and its drag (changing its area and drag coefficient).

Adhesion-based Crawling

Adhesion-based crawling is an alternative to friction-based crawling where a separate active mechanism is used to create traction with the substrate. Because active adhesion generates contact forces independent of friction, buoyancy and lift considerations (Eq. 2.2) become less important. Thus, adhesion creates much more versatile locomotion patterns capable of traversing steep slopes as well as moving in an inverted orientation. To maximize these advantages, adhesion-based crawlers have many adhesive elements spread over a large area. Unlike friction-based crawlers that push off a substrate with their appendages, adhesion-based crawlers reach forward with their appendages, secure themselves to the substrate, and pull their bodies forward [58].

Animals use two primary methods of distributed adhesion. Echinoderms such as sea stars and sea urchins use many appendages called tube feet to perform adhesion-based crawling. Each tube foot has a single adhesive disc that secretes a chemical adhesive to secure the tube foot to

the substrate; it subsequently secretes a second substance to counteract the adhesive as needed during the crawling gait [59]. In contrast, the octopus uses suction generated by many suckers distributed along a few appendages to perform a crawling-like motion [60]. These suckers attach to a substrate by using muscles that create a region of very low pressure inside the sucker (up to 800 kPa lower than the ambient pressure) to produce an adhesive suction force [61].

Due to the technical challenges involved with chemical adhesives, underwater bioinspired robots have focused on the use of suction mechanisms to produce reversible adhesion [62]. For example, dielectric elastomers have been used to create an octopus-inspired sucker where the bending motion of the DEA creates the region of low pressure [63]. A similar adhesive mechanism inspired by the sea urchin used a fluidic piston to create the deformation of the sucker [64]. Another adhesive disc inspired by the clingfish was developed with additional soft geometries specifically to improve performance on rough and non-planar surfaces [65]. However, none of these adhesive systems have been integrated into a crawling robot.

Limited work has been done to replicate adhesive crawling in soft robotics from either a distributed actuation or an underwater adhesion standpoint. He et al. created LCE tubular actuators similar to the tube feet of echinoderms for use in a quadrupedal crawling robot [14]. However, these tubular actuators were not incorporated into a large, distributed array and did not integrate adhesive mechanisms. Previous work also includes an urchin-inspired robot comprising an array of rigid spines and tube feet made from soft fluidically actuated bellows [66] and a sea star-inspired robot with bi-stable buckling actuators [5]. Although these echinoderm-inspired robots used biologically inspired appendages, using magnetic tips for adhesion restricts their crawling to ferrous surfaces. Further development of distributed actuation coupled with reversible adhesion is an open area of research for mobile underwater robots.

2.2.2 Swimming

As noted earlier, we classify swimming locomotion into three broad categories. Jetting takes advantage of momentum conservation as expelling water backwards causes forward motion

of the body. Appendage-based swimming relies on the net drag and lift produced by the cyclic motion of an oar-like appendage (e.g., pectoral fins) to push the body. Finally, undulatory swimming uses a traveling wave passing through the body to interact with the surrounding fluid to create motion [67]. Steady swimming is usually accomplished by cyclic actuation. However, the transient hydrodynamic effects associated with shape change are often critical for short-term bursting or maneuvering. The incorporation of soft actuators or bodies has the potential to improve efficiency, speed, or maneuverability for each of these swimming modes.

Swimming via Jetting

Jet propulsion is a locomotion technique in which water first is slowly drawn into a chamber (intake stroke) and quickly expelled from the chamber (thrust stroke). During the intake stroke, the body increases in volume as water enters. During the thrust stroke, a mechanism contracts the chamber, reducing the volume and pushing the water out in a jet. The body thus moves forward in accordance with the conservation of linear momentum. The amount of thrust produced and the energetic efficiency depend both on the velocity of the jet produced by the contraction and the structure of the vortices formed by the ejected water [68, 69]. The sudden decrease in body volume also creates an acceleration due to the added mass effect as the cross-sectional area of the body decreases [70, 71]. In nature, this method of swimming is used prominently by cephalopods, bivalves, and jellyfish.

Jet propulsion is often modeled by the following equation, which takes into account the thrust created by the jet, the drag acting on the body, as well as any inertial or gravity effects:

$$F_g + m_{eff} \frac{dU}{dt} + \frac{1}{2} C_D \rho A U^2 + q \frac{dm}{dt} = 0, \quad (2.3)$$

where F_g is any net force caused by gravity in the direction of motion, $m_{eff} \frac{dU}{dt}$ is the inertial force caused by acceleration of the body, taking into account the added-mass effects, $\frac{1}{2} C_D \rho A U^2$ is the drag force on the body, and $q \frac{dm}{dt}$ is the jet thrust [72]. Here, $\frac{dU}{dt}$ is the time rate

of change of the body's velocity, m is the mass of the body, m_{eff} is the effective mass including contributions from the added-mass effect, q is the velocity of the jet with respect to the body, and $\frac{dm}{dt}$ is the time rate of change of the mass of the body plus enclosed water. From this equation, we can see that during horizontal swimming, the motion of swimmer at steady-state is balanced by the drag force on the body and the jetting force caused by the outflow of fluid.

Jet-propulsion mechanisms among animal species are similar in method but very different in performance. Both squids and octopuses have antagonistic muscles around their mantles that expand the mantle to draw in water and contract the mantle to rapidly expel water [73]. This mechanism creates large bursts of speed that can exceed the speed of fish at the expense of locomotion efficiency [74]. Similarly, a jellyfish uses the muscles around its bell to force water out, forming the jet. However, once the thrust stroke is over, it releases its muscles and the bell returns to its large-volume configuration through the elasticity in the bell itself rather than additional musculature. Thus the jellyfish only expends energy during the thrust stroke and not during the intake stroke, greatly increasing its swimming efficiency [44].

Soft robots use various mechanisms to create locomotion via jet propulsion. RoboScallop, a bivalve-inspired robot, used a motor-powered hinge to open and close rigid shells to expel water [9]. A Hoberman sphere covered in a flexible skin has also been used to create jet-based thrust, taking advantage of the mechanism's large capability for volume change [75]. Another octopus-inspired soft robot used a hyperelastic skin pressurized with water in which the elastic restoring force of the skin forces the jet of water out of the body [76]. Finally, Serchi [77] developed a cephalopod-inspired pulsed propulsion robot that first demonstrated the advantages of combining soft actuation with pulsative jet thrust. Several different approaches have been used to create jellyfish-inspired robots, in an attempt to reproduce the lightweight and efficient mechanisms found in nature. Hydraulic actuators [78] and SMA actuators [79] have been used to create jellyfish-like robots, but neither have been able to reproduce the high locomotion efficiencies characteristic of biological jellyfish. Recently, DEA actuators were used to create the most efficient untethered jellyfish robot to date [80].

Appendage-driven Swimming

For the purposes of our analysis, we describe the primary hydrodynamic forces associated with appendage-based propulsion as lift and drag. Though both forces may be present on a body as it moves in the water, animals will generally rely on one of the two forces for the purpose of generating motion. A discussion of how lift-based swimming emerged in terrestrial animals to increase speed and efficiency can be found in Fish [81]. This section provides a brief discussion of lift-based propulsion using appendages. Lift forces are also important for swimmers that rely on body undulations for locomotion.

In simple terms, the key difference between lift-based and drag-based swimming is in the direction of the fluid forces generated relative to the direction of appendage movement. In either case, the hydrodynamic thrust is in the direction of net animal motion. If the appendage is primarily moving perpendicular to the direction of the animal's net motion, it is considered lift-based swimming; if the appendage is moving parallel to the direction of the animal's net motion, it is considered drag-based swimming. By changing the angle of attack of the appendage, the animal can change the shape of its appendage interacting with flow and thus its hydrodynamic profile throughout the strokes of the gait. Lift and drag forces are often modeled by the quasi-steady drag and lift equations

$$F_D = \frac{1}{2}C_D\rho AU^2 \quad (2.4)$$

$$F_L = \frac{1}{2}C_L\rho AU^2 \quad (2.5)$$

where C_D and C_L are the coefficients of drag and lift, respectively, which depend on the shape of the appendage, ρ is the density of the fluid, A is the characteristic area of the appendage, and U is the fluid speed with respect to the appendage. A swimmer can change the forces generated by its appendage by changing the angle of attack with respect to its body motion, thus changing the shape of the appendage interacting with the surrounding fluid. This changes both the coefficients

of lift and drag, as well as the reference area (depending on its formulation). The quasi-steady empirical formulations (see Eq. 2.4, 2.5) are often used with time-varying velocities, areas, and lift or drag coefficients to estimate the net forces generated over a cycle. For example, Vogel [82] used the quasi-steady lift and drag equations (see Eq. 2.4, 2.5) to estimate thrust by assuming constant speed, hydrodynamic coefficients, area, and a specific duty cycle of 50% (thrust is produced during half of the gait cycle) for drag-based and 100% (thrust is produced during the entire gait cycle) for lift-based (no reversal delay) motion.

Drag-based swimming operates on a similar principle to oar mechanics for boat travel. The two phases that characterize drag-based swimming are the recovery stroke and the power stroke. The animal or robot moves an appendage through the water and the drag force opposing that motion pushes the body forward. For net travel, the thrust produced by the power stroke must be greater than that produced by the recovery stroke. There are various ways to accomplish this. For example, freshwater softshell turtles twist their fore-flippers so that the cross-sectional area of the flipper interacting with flow is smaller during the recovery stroke than the power stroke, leading to lower drag on the recovery stroke [83]. Platypus propel themselves using directionally-compliant fins. The fins flex on the upstroke and, once at maximum forward extension, expand and push backward. Frogs, on the other hand, actively pull their legs in after the power stroke and glide until an optimal velocity is reached before beginning the cycle again.

Drag-based propulsion has been used for several swimming robots. A whirligig beetle-inspired robot made by Jia et al. that used the principle of directional compliance [84] was found to be very energy efficient at low velocities. A robot developed by Tang et al. used dielectric elastomer actuators [85] to create a frog-like burst-coast motion. This locomotion strategy can often generate high accelerations but lacks maneuverability. Kramer et al. developed variable-stiffness limbs to showcase a morphing design that creates both a flipper for paddling and a leg for crawling [8]. Compared to other swimming strategies, drag-based locomotion is demonstrated more by amphibious or terrestrial animals because land-based appendages can be readily adapted to this method [81]. This type of propulsion can be very efficient, as demonstrated

by the whirligig beetle [86], and rapid, as seen in platypus and frogs. However, according to Fish [81], drag-based propulsion is a less efficient strategy for fully aquatic mammals, partly due to the drag generated by the non-streamlined body arrangements associated with such propulsion. Despite the disadvantage of potential drag increase by having these appendages, drag-based swimming is a widely used method for soft robot swimming and can be an energy-efficient design solution, particularly for amphibious locomotion.

An inexhaustive list of animals that use more lift than drag to propel themselves with appendages include species in the Pinniped clade (walrus, sea lions, fur seals), humans (kicking in front crawl), and Spheniscidae (penguins). The mode of propulsion is similar to flapping for flying animals; however, in aquatic animals gravitational forces are offset by buoyancy. Lift-based swimming typically relies on the shedding of a vortex ring in the direction opposite to the direction of motion. Sea turtle-inspired limbs are an example of biological lift-based propulsion, and have also been used to showcase soft actuators with multi-modal actuation. For example, a limb made from SMA wire was designed to be capable of both bending and twisting motions, allowing different cross-sections of the limb to interact with flow during the power and recovery phases of the stroke [87].

Undulatory (Body-driven) Swimming

Many swimming organisms propel themselves through the water by generating undulatory traveling waves along their bodies. Dominant underwater undulation motion strategies can be broken into anguilliform (i.e., eel-like swimming), carangiform (i.e., mackerel-like swimming), and thunniform (i.e., tuna-like swimming). Though there is a continuum of behavior between these three categories, they serve as useful boundaries for classification. The differences between the three categories can be explained based on the percentage length of the body involved in the traveling wave. Fish that primarily generate thrust with their caudal segments are considered thunniform swimmers. Fish that generate thrust with their entire bodies are considered anguilliform swimmers, and fish between the two would be considered carangiform

swimmers [82].

Most soft robots operate in the high Reynolds number regime where inertial rather than viscous fluid forces are dominant. For this inertial regime, two main explanations have been proposed for how traveling waves interact with the fluid to create propulsion, i.e., how body waves impart directional momentum to the fluid. The first theory suggests that propulsive thrust is generated by reactive forces acting on the body [88, 89]. Fluid parcels next to the body are accelerated toward the rear of the body because of the pressure variations generated by the traveling wave. This imparts backwards momentum to the fluid thereby generating a forward propulsive force on the body. Though this explanation provides some insight into the fluid forces responsible for propulsion, the fluid accelerations are tightly coupled to vortex shedding at the tail. This vortex shedding also provides a propulsive force. Specifically, evidence suggests that vortex rings are generated twice per cycle, which, through their interactions, create a reverse von Kármán vortex street (RvKVS), where rearward momentum is imparted to the fluid [90, 91]. According to von Kármán [92, 93], the thrust generated by a RvKVS can be predicted using

$$T = -\frac{\Gamma^2}{2\pi a} + \frac{\Gamma b}{a}(1 + 2v), \quad (2.6)$$

where T is thrust, Γ is the vortex intensity, a is wavelength, b is wake width, and v is the vortex traveling velocity. The first component is an induced-drag element, whereas the second term is the propulsive element. Thrust can be enhanced by increasing the coefficient $\frac{b}{a}(1 + 2v)$: increasing the undulation frequency will decrease wavelength a ; increasing the amplitude of oscillation will increase the wake width b ; finally, the induced velocity is also proportional to b/a , thus increasing oscillation frequency and amplitude will also increase v and, correspondingly, thrust T .

Previous work also suggests that there exists an optimal oscillation frequency for swimming that can be expressed in terms of the dimensionless Strouhal number, $St = fL/U$, where f is the oscillation frequency, L is the characteristic length (often the amplitude of the caudal fin

oscillation for fish), and U is the velocity. Fish typically travel with Strouhal numbers of 0.25 to 0.35 [94] and similarly robotic undulating fish are also designed to operate in this Strouhal number range [95].

The physical principles that relate vortex shedding to propulsion are complex. Not only does the body oscillation generate thrust, it can also serve as a drag-reduction mechanism by ensuring optimal vortex arrangements in the wake behind the body and potentially re-laminarizing the turbulent boundary layer formed on the body [96]. Further, because of the complex and interdependent nature of the fluid-structure interactions involved in undulatory swimming, researchers often have difficulty distinguishing between the various mechanisms involved, e.g., reactive forces, added mass effects, vortex-based propulsion, and drag reduction. However, despite the challenges associated with modeling these phenomena, many robots have been developed that successfully exploit undulatory swimming motions.

Undulatory swimming is successful in part because it can be accomplished using streamlined body shapes with few external appendages. This characteristic can be replicated in robots using soft materials to actuate and connect segments. For instance, a recent study used DEA segments to create a robot capable of anguilliform propulsion [12]. Similarly, electro-active polymer actuators have been used to generate undulations in a ray-inspired robot [97]. For faster propulsion, researchers have developed carangiform-type swimming robots by discretizing the traveling wave into a limited number of actuated body segments. These segments are wrapped in a deformable skin, generally made from a synthetic rubber such as latex or silicone. *RoboTuna* [98], the first successful robotic fish, was developed at MIT in 1995 and used foam and lycra to create a soft deformable interface. Since this seminal work was published, many more robotic fish have been developed with various actuation components, such as servo motors encased in corrugated rubber tubing [99], a silicone bidirectional pneu-net actuator powered by a miniature hydraulic pump [6], as well as a motor driving antagonistic tendons around a free-to-rotate tail joint capable of high actuation frequency [48]. These examples demonstrate that soft, deforming materials are advantageous for developing bioinspired robots and implementing the motion

strategies that make animals successful.

Chapter 2, in full, is a reprint of the material as it appears in: Hermes, M.* , Ishida, M.* , Luhar, M., Tolley, M. T. (2020), "Bioinspired Shape-Changing Soft Robots for Underwater Locomotion: Actuation and Optimization for Crawling and Swimming", In Paley, D. A., Wereley, N. M. (Eds.), *Bioinspired Sensing, Actuation, and Control in Underwater Soft Robotic Systems* (pp. 7-39). The dissertation author was the co-primary investigator and co-first author of the sections of the paper that are reprinted in this chapter.

Chapter 3

Morphing Structure for Changing Hydrodynamic Characteristics of a Soft Underwater Walking Robot

Existing platforms for underwater exploration and inspection are often limited to traversing open water and must expend large amounts of energy to maintain a position in flow for long periods of time. Many benthic animals overcome these limitations using legged locomotion and have different hydrodynamic profiles dictated by different body morphologies. This work presents an underwater legged robot with soft legs and a soft inflatable morphing body that can change shape to influence its hydrodynamic characteristics. Flow over the morphing body separates behind the trailing edge of the inflated shape, so whether the protrusion is at the front, center, or back of the robot influences the amount of drag and lift. When the legged robot (2.87 N underwater weight) needs to remain stationary in flow, an asymmetrically inflated body resists sliding by reducing lift on the body by 40% (from 0.52 N to 0.31 N) at the highest flow rate tested while only increasing drag by 5.5% (from 1.75 N to 1.85 N). When the legged robot needs to walk with flow, a large inflated body is pushed along by the flow, causing the robot to walk 16% faster than it would with an uninflated body. The body shape significantly affects the ability of the robot to walk against flow as it is able to walk against 0.09 m/s flow with the uninflated body, but is pushed backwards with a large inflated body. We demonstrate that the robot can detect changes in flow velocity with a commercial flow sensor and respond by morphing into a

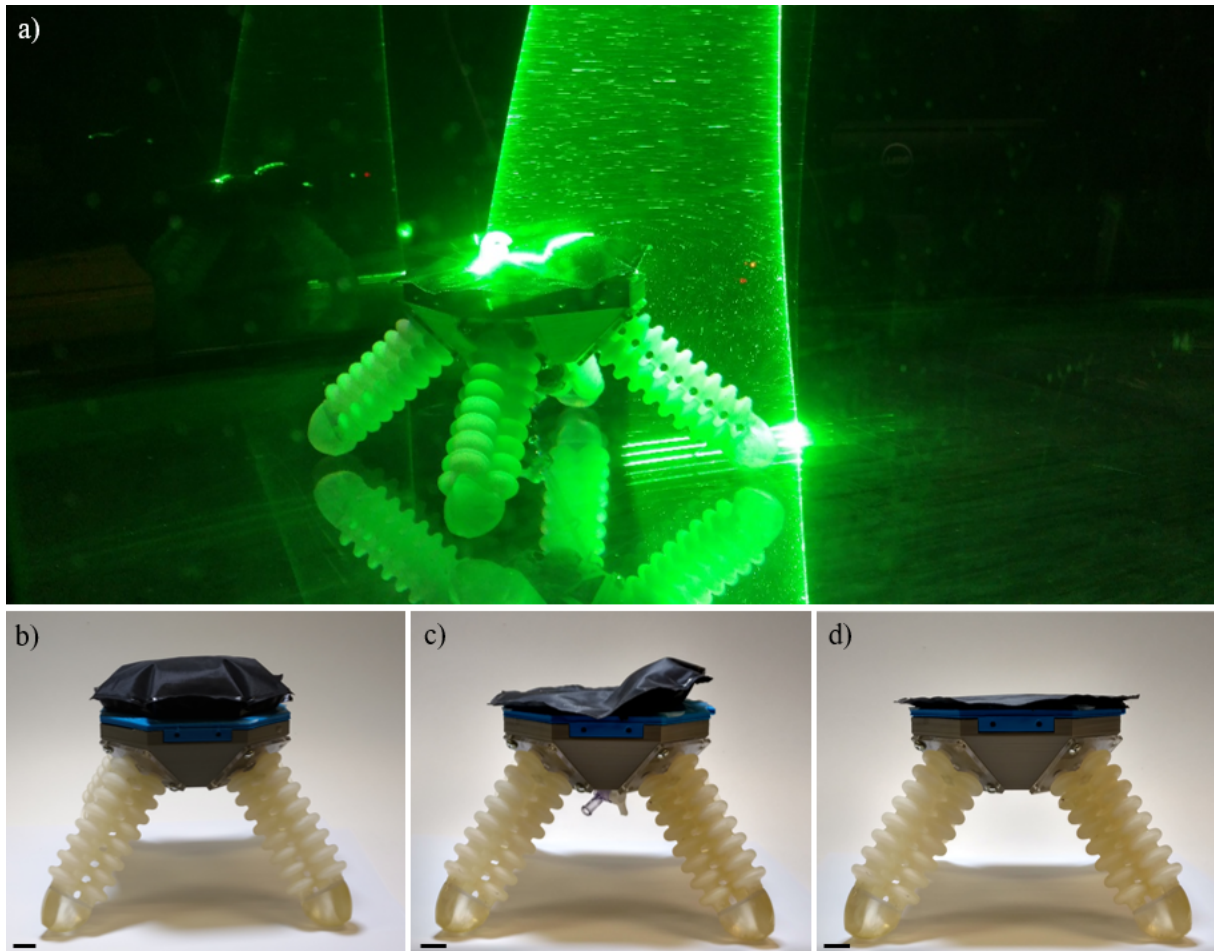


Figure 3.1. Soft quadruped robot for walking underwater with morphing body that changes shape to be more hydrodynamically advantageous based on force sensor readings. a) Robot with morphed body in flow illuminated by laser for flow visualization. b) Robot with symmetrically inflated body. c) Robot with asymmetrically inflated body. d) Robot with flat body. All scale bars are 15 mm.

hydrodynamically preferable shape.

3.1 Introduction

Techniques for locomoting underwater differ significantly between man-made and biological systems. Manned submersibles and remotely operated vehicles (ROVs) often use jets [100] or rotating propellers [101] for propulsion. These strategies work well in open water, but are bulky and noisy compared to biological counterparts and have difficulty navigating through

confined spaces. Some organisms use shape change to create jet propulsion [102], but many more use an undulating body or oscillating fins to swim [103]. Regardless of the swimming method, active station-keeping in flow (eg. for examining a surface or taking long-duration measurements) is energy intensive. Many marine organisms that live on underwater surfaces like reefs or tidepools employ a form of legged locomotion using rigid [104] or soft appendages (eg. hydraulic tube feet [105]) to locomote and reduce the energetic cost of station-keeping.

The morphology and locomotion behaviors of animals suggest the importance of hydrodynamic characteristics in underwater walking. Unlike on land, stability in water is affected by fluid forces like buoyancy, lift, and drag, which influence underwater walking [106]. For example, amphibious newts alter their gaits when transitioning from land to water to reduce the drag on their legs [107, 108]. In addition, crabs searching for food orient themselves toward an odor source when walking in low flow, but orient themselves in the hydrodynamically preferable direction when walking in high flow, even if that inhibits their olfactory senses [109].

Morphing structures can actively change shape during system operation and many marine organisms use them to dynamically change their interactions with fluid [110]. Small fish have fins that deform as they swim [111] while octopi and squids create large body deformations to both propel and maneuver their bodies [112]. Similar morphing structures have been used in robotics such as the octopus-inspired PoseiDRONE [113] and in robots designed by artificial evolution [114]. Octopus-inspired soft skins have changed the 2D shape and texture of a surface into a preprogrammed 3D Gaussian structure [115]. Morphing elements were used in the flippers of a turtle-inspired swimming robot [116] and in the wings of a bat-inspired flying robot to increase lift and decrease drag during various sequences of the actuator's motion [117].

Soft robotics is a growing subfield of intelligent systems that leverages inherent material compliance to create highly adaptable robots [118]. These systems often use fluidic elastomer actuators (FEAs), which are enclosed chambers made of hyperelastic materials that change shape when actuated with fluid [119]. Flexible but inextensible materials constrain and determine actuator movement when the actuator is subjected to internal pressure, while maintaining system

compliance [120, 121, 122, 123]. The material flexibility of soft actuators gives them infinite degrees-of-freedom and allows continuous deformation [124] to form smooth surfaces that are advantageous for interactions with fluids. Robots using these components can adapt to their environments, which allows them to perform actions like conforming to irregular surfaces and objects [125]. This behavior is especially beneficial for a legged system as a soft actuator can bend to various different shapes that would require many joints to replicate in a rigid system [126].

Previous work on underwater walking robots has primarily focused on rigid jointed walkers. The six-legged AQUAROBOT was developed for measuring seabottom roughness via pressure sensors in the feet of the robot [56]. An inexpensive autonomous legged underwater vehicle was created for physically locating mines as a largely independent agent of a swarm [127]. Little Crabster, another robot with six rigid legs was developed specifically for exploring shallow water in high tidal environments [4]. To test an underwater walking gait based on the punting gait of a crab, a one-legged robot was designed to show a self-stabilizing locomotion mode combining swimming and pushing gaits [128], while another bioinspired crab robot was created to analyze the underwater dynamics and fluid forces on the gaits of a hybrid swimming-walking robot [129]. However, the aforementioned underwater walking robots have difficulty walking over uneven terrain and adapting to enclosed environments, which could be addressed with soft robotics components.

Here we present a soft robot capable of sensing local flow conditions and morphing a portion of its body to maintain a hydrodynamically advantageous profile (Fig. 3.1). The shape of the body is altered using soft fluidic actuators that switch the body profile between different states to change hydrodynamic characteristics. A commercial off-the-shelf force sensor is used to determine large changes in flow speed, allowing the robot to opportunistically change its body shape. When walking in the same direction as the flow, the robot can increase the drag on its body and when walking in still water or against flow it can reduce the drag. In addition, under higher velocity flow the robot can decrease lift to give it additional traction.

In Section 3.2, we describe the design of the soft hydraulic quadruped robot and the morphing body. In Section 3.3, we detail the experimental methods used and in Section 3.4, we discuss the effect of different robot bodies attached to the same legged base on hydrodynamic forces, robot traction, and robot walking speed in flow. We also demonstrate a soft robot that can sense changes in flow speed and morph its body shape in response.

3.2 Robot Design

The underwater walking robot consists of four soft hydraulic legs and a morphing body attached to a rigid frame. Each leg is made of three chambers with bellows. Pressurizing a chamber causes a net bending motion and actuating the chambers in a prescribed sequence creates a walking gait [130]. Similarly, the robot changes the shape of its morphing body by pressurizing separate pouches with water. This produces a reversible shape change to improve the robot's hydrodynamic profile. Morphing the body changes the shape of the surface interacting with flow which affects both the lift and drag and morphing into an asymmetric shape creates an orientation dependence. Because different flow conditions necessitate different body shapes, the robot must know when to morph its body so we include a sensor that provides information about the flow around the robot.

3.2.1 Hydrodynamic Model

The fluid forces of drag and lift on the body are functions of the body shape, the density of the fluid, the cross-sectional area of the body in contact with the flow, and the fluid velocity around it. By inflating and deflating the morphing body on top of the robot, the robot alters its shape and its cross-sectional area, changing both drag and lift. Increasing drag will increase the walking speed of the robot when walking in the same direction as flow, but will decrease walking speed when walking against flow. Decreasing lift will increase the normal force applied by the ground, which increases the friction between the ground and the robot; increasing lift will lower the friction between the ground and robot, causing it to more easily slip or move upward.

To predict the critical velocity U_C at which the underwater walking robot begins to slip, we consider a simple force balance. At the leg-substrate interface, we assume that the drag force generated by the fluid $F_d = \frac{1}{2}C_D\rho AU_C^2$ and the static friction $F_f = \mu N$ are in balance at the point of incipient motion. From this we obtain

$$\frac{1}{2}C_D\rho AU_C^2 = \mu N = \mu \left[(M - \rho V)g - \frac{1}{2}\rho C_L AU_C^2 \right] \quad (3.1)$$

where C_D and C_L are the drag and lift coefficients for the morphing body (respectively), A , V , and M are the planform area, volume, and mass of the robot (respectively), μ is the static friction coefficient for the leg-substrate contact, N is the normal force on the robot from the substrate, ρ is the density of the surrounding fluid, and g is the acceleration due to gravity. We used the planform area for both the lift and drag calculations because the planform and frontal area were similar and would simplify notation. Rearranging the above expression yields the following relationship for the critical velocity:

$$U_C = \sqrt{\frac{2\mu(M - \rho V)g}{\rho A(C_D + \mu C_L)}} \quad (3.2)$$

To increase the critical velocity, a soft robot capable of morphing could decrease planform area A or alter its shape to decrease $C_D + \mu C_L$. Along with minimizing the drag coefficient C_D by morphing into a smooth hydrodynamically-efficient shape, another viable strategy is to alter its shape to reduce lift.

3.2.2 Robot Components

We have previously presented a soft quadrupedal robot capable of navigating unstructured terrain on land [131]. In this work, we made a new version of this robot to use hydraulics instead of pneumatics for walking underwater. We fabricated the soft fluidic elastomer actuators that

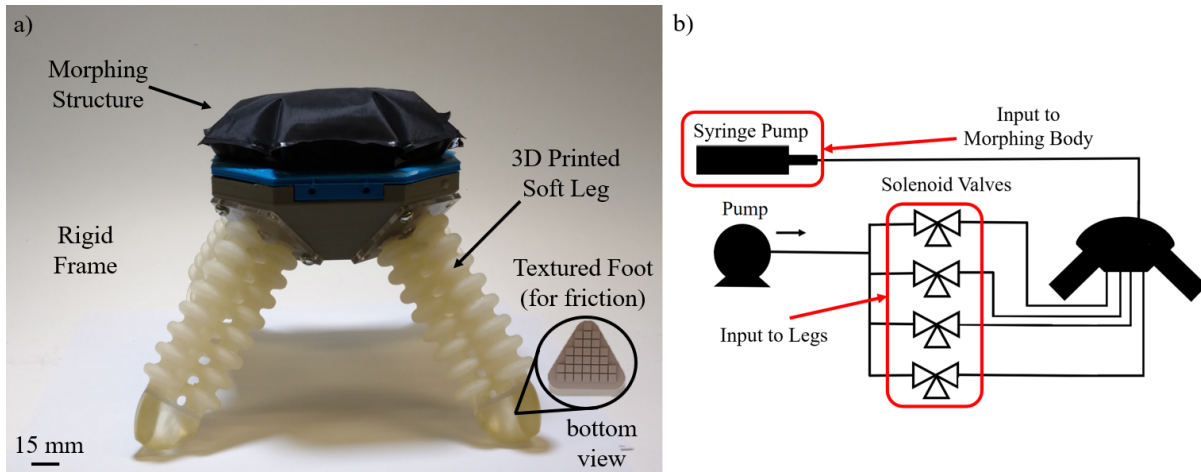


Figure 3.2. Images of robot design. a) Image of the soft quadruped with morphing body. b) Schematic of the hydraulic system in which four three-way valves inflate and vent the legs and a volumetrically-controlled syringe pump inflates and deflates the morphing structure.

make up the legs of the robot using a commercially available multimaterial 3D printer (Connex3, Stratasys) out of a photocured elastomer (TangoPlus and VeroClear mixture). Each flexible actuator consisted of three chambers with bellows that extended when internal pressure was applied, causing a net bending motion [131] (see Supplementary Video).

Since operation of the legs required a consistent connection to a hydraulic pressure source, a tether of tubing connected the robot to a land-based pump and solenoid valve system. We connected the tether only during the experiments that involved walking or active body morphing. Four three-way solenoid valves switched between pressurizing and venting chambers of each leg and two other valves switch between pressurizing and venting the morphing body (Fig. 3.2). The valves were cyclically opened to inflate the chambers of the leg to create the walking gait (see Supplementary Video).

A rigid, 3D-printed frame held the four legs at a 45° angle relative to the ground. An inflatable pouch formed a soft morphing body on top of the 3D printed frame that changed the hydrodynamic characteristics of the robot when pressurized. To fabricate the pouch, we attached two sheets of taffeta fabric together with a heat-activated adhesive using an impulse sealer to form an enclosed volume. We then punctured one sheet to insert a tube and fitting for

the hydraulic line and we used a thermoplastic epoxy to seal the opening around the fitting. We then adhered the bottom of the pouch to a rigid cover that could be reversibly attached to the top of the frame.

We created a morphing body with two pouches capable of taking three shapes to explore different hydrodynamic profiles. When inflated, the large pouch spanned the entire top surface of the robot (Fig. 3.1b) and the small pouch spanned half of the top surface of the robot (Fig. 3.1c). When both pouches were deflated, they formed a flat top (Fig. 3.1d); in no configuration were both pouches inflated simultaneously. The smaller pouch was 62 mm in length and 43 mm in height while the larger pouch was 125 mm in length and 55 mm in height. The mass of the rigid robot frame and legs combined was 356 grams and the underwater experiments were performed with 267 grams of ballast for an underwater weight of 293 grams when accounting for buoyancy. The pouches were inflated and deflated with a volumetrically-controlled syringe pump system [132]. To detect flow speed changes, we attached a commercial off-the-shelf flow meter (Adafruit) to the body of the robot. Sensing the changes in flow allowed the robot to respond to unfavorable flow conditions by morphing its body.

3.3 Methods

3.3.1 Water Channel and Flow Generator

We conducted experiments with the robot remaining stationary for visualizing flow, measuring the lift and drag on the robot, and measuring the critical velocity causing sliding in a freshwater channel with a length of 762 cm, a width of 91 cm, and a water depth of 48 cm (Fig. 3.3). The maximum flow velocity of the channel was 60 cm/s with a background turbulence level of less than 1%. The ambient fluid temperature in the channel was 23 °C, corresponding to a kinematic viscosity of $0.93 \times 10^{-2} \text{ cm}^2/\text{s}$. The flow parameters differed by a maximum of 5% across the width of the channel. We conducted the tests of the robot walking and of the active response with the flow sensor in another similar freshwater flow channel.

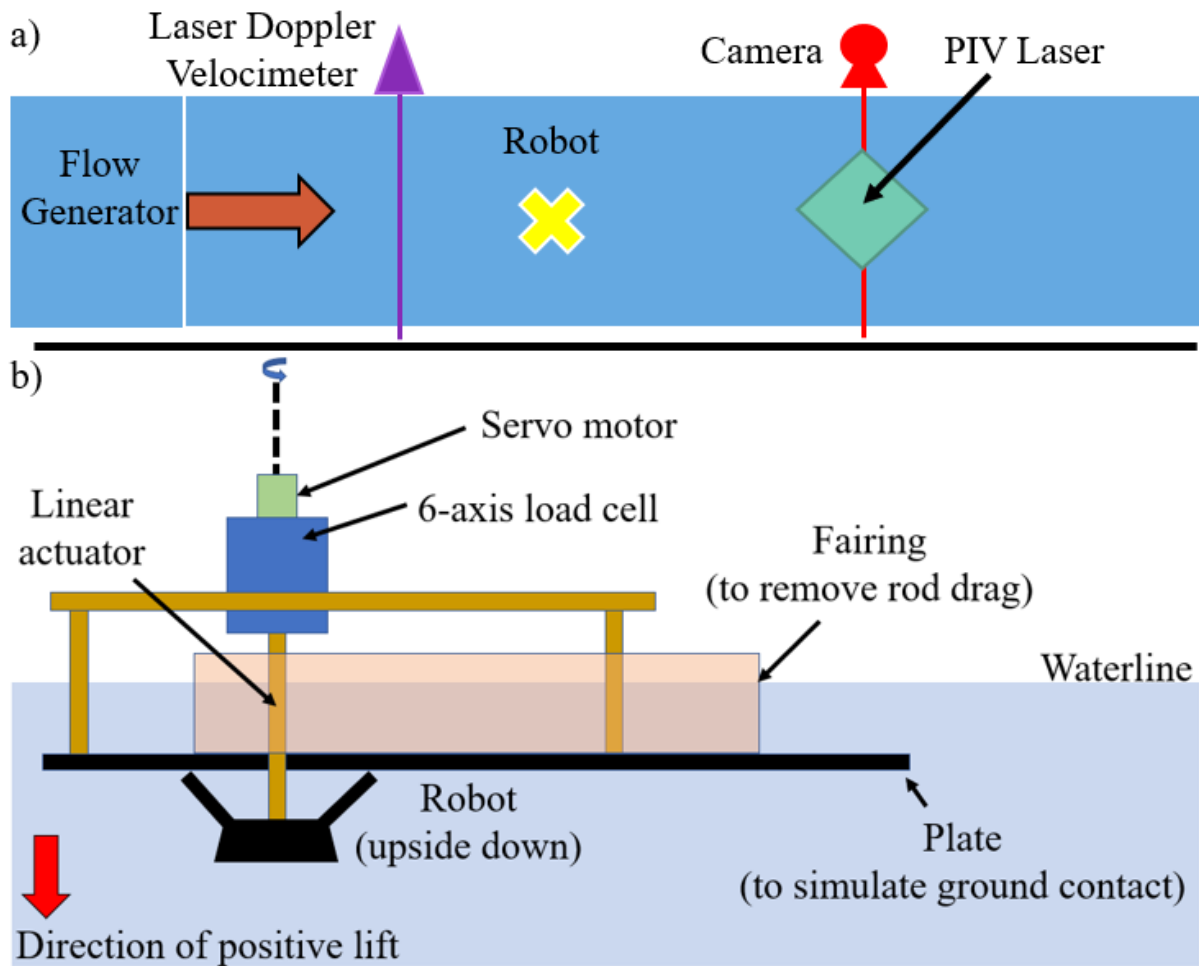


Figure 3.3. Diagrams of the water channel and load cell. a) Layout of the water channel with instrumentation for imaging and measuring flow over the robot. b) Configuration of six-axis load cell for measuring hydrodynamic forces on the robot in flow.

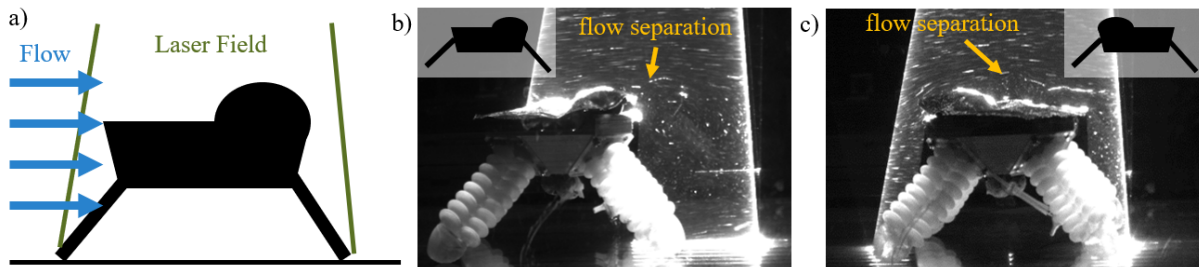


Figure 3.4. Visualization of flow from left to right over the stationary robot with different body configurations. a) A schematic of the imaging process. b) Visualization of flow with the inflated half on the trailing edge. c) Visualization of flow over the body with the inflated half on the leading edge.

3.3.2 Measurement

We measured flow velocity using Laser Doppler Velocimetry (LDV) near the bottom of the channel at the height of the robot to capture boundary layer effects. We subjected the three morphed configurations to increasing flow speeds to determine the critical velocity at which the stationary robot would begin to lose traction and slide. Stationary cameras recorded the robot from the side to track the position of the robot in the direction of desired motion and from the bottom to track the out-of-plane motion. We then used open-source optical tracking software (Tracker, Open Source Physics) to determine the walking speed of the robot with different body configurations when in still water and when in flow. We also estimated the friction coefficient between the robot and the glass channel by tilting a glass pane in the water and measuring the angle at which the robot slid due to gravity.

To measure the effect of shape change on the hydrodynamic forces experienced by the body, we attached the static robot to a six-axis load cell in the water channel (Fig. 3.3b). We measured the lift and drag on the four configurations of the morphing body (flat, inflated half on the leading edge, inflated half on the trailing edge, and symmetrically inflated) with and without the legs to isolate the specific contribution of the body shape. Because the robot was not walking, we did not attach the hydraulic tether to the robot for these experiments, which would have interfered with measurement of the forces on the body. For each of these cases, we recorded baseline forces with the robot in still water so we could subtract out the effects of gravity. After increasing the flow speed to the desired level, we waited two minutes for the flow speed transients to subside and collected and averaged lift and drag data at 100 Hz for sixty seconds at three different flow speeds.

We also imaged the flow around the robot using a Particle Image Velocimetry (PIV) system with a laser field projected into the water from above the channel. Light scattered by particles in the water was tracked by software from frame to frame to create a visualization of the flow field surrounding the robot with the assumption that the particles moved at the same

velocity as the fluid. The flow around the static robot was approximately 20 cm/s and 150 images were taken at rates ranging from 5 to 30 frames per second.

3.4 Experimental Results and Discussion

3.4.1 Static Characterization

We used the PIV images to examine the flow over the tops of the different morphed bodies. Since the flow closely followed the continuous contour created by the soft morphing body, the flow over the morphed body was smooth and did not separate until the trailing edge of the inflated pouch. When the inflated body was on the trailing edge of the robot (Fig. 3.4b), the shape induced turbulence behind the robot. However, with the inflated body on the leading edge (Fig. 3.4c), the flow separation occurred over the center of the robot, which led to increased fluid drag on the robot.

Changing the shape of the robot body significantly affected the hydrodynamic forces (Fig. 3.5). The drag was lowest on the flat configuration and highest on the symmetrically inflated configuration. After calculating the lift and drag coefficients for the robot with legs (Fig. 3.5c), we see that the flat shape has a high drag coefficient, indicating that the reduction in drag is because of its small frontal area. Although the asymmetrically inflated bodies had the same frontal area, there was more drag when the inflated half was on the leading edge, likely due to the turbulence generated over the robot. Furthermore, the robot experienced the most lift when the inflated half was on the leading edge and experienced the least lift when the inflated half was on the trailing edge. Using an inflatable body, it was easier to reduce the lift on the robot than to reduce the drag. In the highest flow condition, we decreased the lift force up to 40% (from 0.52 N to 0.31 N) while increasing drag by only 5.5% (from 1.75 N to 1.85 N) compared to the uninflated body. We also saw that including the legs in the highest flow condition increased the lift on the body by up to 85% (from 0.28 N to 0.52 N) and increased the drag by up to 200% (from 0.58 N to 1.75 N).

We combined the effects of lift and drag scaled by the friction coefficient as detailed in Section II B to predict which body configuration would be most resistant to sliding in flow. We determined a static coefficient of friction $\mu = 0.65$ by placing the robot in water on an inclined glass plate, increasing the angle of inclination, and recording the angle of the plate at the point that the robot began to slide. From these results, we predicted that the robot would be most resistant to sliding when the inflated half was on the trailing edge and least resistant to sliding when the inflated half of the body was on the leading edge (Fig. 3.5). In the next section we describe the results of experiments directly testing this ability to manipulate the traction of the robot.

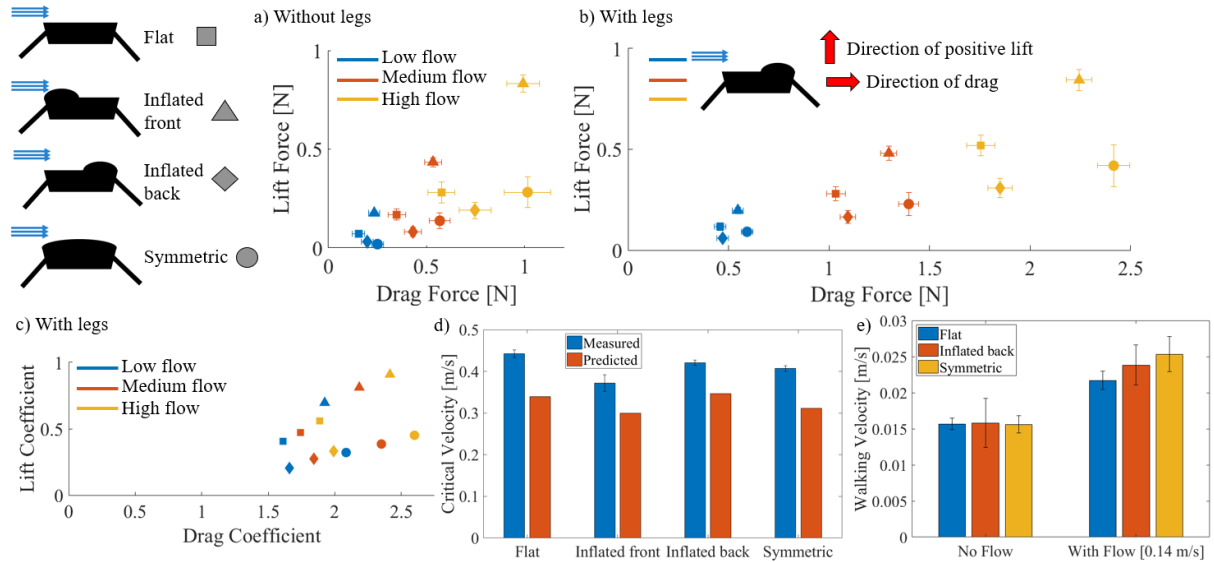


Figure 3.5. Comparison of lift and drag on the robot at low (0.204 m/s, $Re = 2.56e4$), medium (0.295 m/s, $Re = 3.71e4$), and high (0.369 m/s, $Re = 4.64e4$) flow speeds and measurements of critical velocity and walking speed. a) Lift and drag forces on the different body configurations without legs at three flow velocities. b) Lift and drag forces on the robot with legs. c) Coefficients of lift and drag on the robot with legs. d) Critical flow velocities causing the robot to slide calculated from the measured forces compared to direct measurements. e) Robot walking velocity in still water and in water flowing in the direction of motion of the robot. Reynolds number is calculated using the equation $Re = uD_H/\nu$ where u is the water velocity, \sqrt{A} is the characteristic length of the body of the robot, and ν is the kinematic viscosity of the water. Error bars represent one standard deviation.

3.4.2 Robot Traction

To measure robot traction in flow, we slowly increased the flow speed in the channel until the point at which the robot began to slide. The flat body required the highest flow speed to induce sliding, while the symmetric body required a lower flow speed to induce sliding because of the increased drag (Fig. 3.5d). The ability of the asymmetric body to resist sliding was dependent on its orientation. When the inflated half was on the leading edge of the robot, it had the least resistance to sliding of all the body configurations as flow separation occurred over the center of the body leading to increased lift and drag. When the inflated half was on the trailing edge, it had more resistance to sliding than the symmetric inflated configuration and the other asymmetric configuration. Since there was less lift when the inflated half was on the trailing edge, there was more friction resisting sliding. This experiment shows that the model predicts the trend between body shape and critical flow velocity well, although there are some differences in magnitude which we attribute to unmodeled interactions between the friction pads of the feet and the underwater glass surface. Because the discrepancy is so large, we believe that our experiment to determine the friction coefficient does not capture these effects.

We attribute some of the variance in the results to unintended asymmetry of the pouches caused by deformation in flow. This asymmetry could have led to an unintended orientation dependence or contributed to rotation of the robot or off-axis forces on the robot. The flow acceleration could have caused brief transients in flow speed. In addition, there is uncertainty in the calculated friction coefficient which could have affected the predicted values.

3.4.3 Robot Speed

In still water, the robot's walking velocity of 15 mm/s was too slow for the different bodies to affect the hydrodynamic forces and thus there was no change in robot speed. However, when walking in the direction of flow, the morphing body had a noticeable effect on the walking speed of the robot (Fig. 3.5e). The robot walked slowest with the flat, uninflated body that

had the lowest drag, fastest with the symmetric inflated body that had the most drag, and at an intermediate speed with the asymmetric inflated body.

We show that the body significantly affects the ability of the robot to walk against flow, as the flat, low-drag body is able to walk in 0.09 m/s flow while the symmetrically inflated body is pushed backwards (see Supplemental Video). Variances in these experiments were likely due to the drag on the hydraulic tether.

3.4.4 Active Body Morphing

Finally, we simulated a robot able to actively deform the shape of its body to adjust to flow conditions. Using a flow sensor, the robot sensed flow above or below predetermined thresholds and then morphed its body into a more desirable configuration (see Supplementary Video). We demonstrated this response with a simple experiment. When the asymmetric inflated body was on the leading edge of the non-walking robot, we increased the flow speed above the critical flow velocity at which the robot began sliding. The robot sensed the flow speed exceeding the threshold to begin sliding and morphed to the flat state that was more resistant to sliding and the robot was able to stop its sliding motion (Fig. 3.6).

This demonstrates how a robot capable of morphing its body can adapt to changing flow. We can imagine that a robot walking in the same direction of flow would want a large body with increased drag and lift that can be pushed along by the flow. However, if the flow were to change directions, the robot would want to decrease drag and lift to either walk against flow or avoid being pushed backward when not walking (see Supplementary Video).

3.5 Conclusions and Future Work

In this work, we present a robot with soft legs and a morphing body, capable of operation underwater, that can change its shape when a change in flow is encountered. We have shown that a morphing body that can actively respond to flow conditions will create favorable hydrodynamic characteristics. The morphing body can be advantageous both in helping the robot maintain a

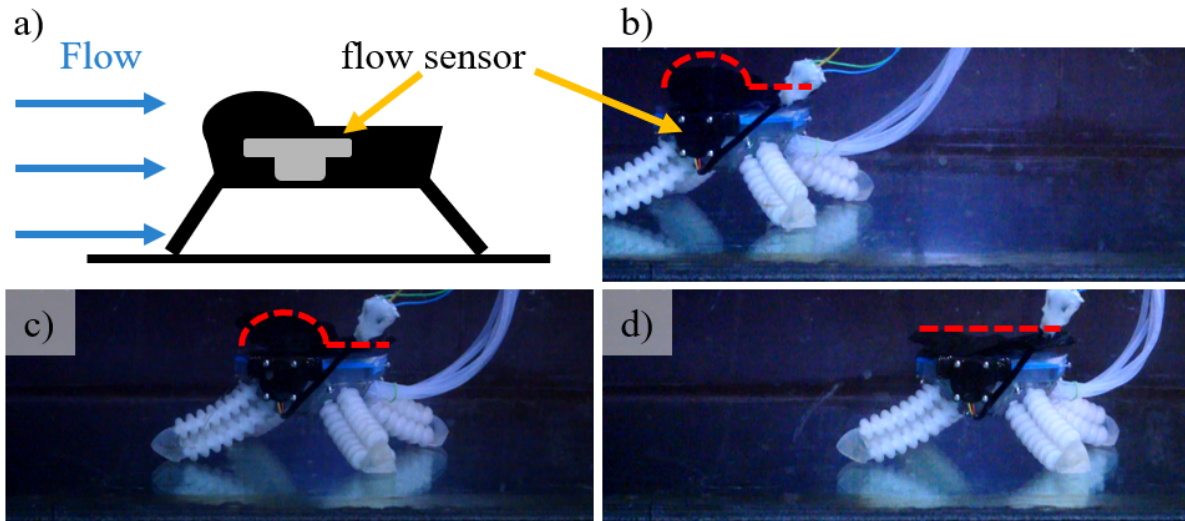


Figure 3.6. The robot with force sensor detecting increased flow and morphing its body to compensate. a) A schematic of the sensor experiment b) Robot with asymmetric body on the leading edge begins sliding in flow. c) Flow sensor with moving average filter determines flow is high enough to be detrimental. d) Robot stops sliding when the inflated body is deflated to the flat body.

stationary position in flow as well as aiding walking. This concept is applicable to other underwater systems that wish to adapt to changing flow characteristics and leverages the advantages of soft actuators to form a continuous surface for interaction with flow.

Future work could address improving the robot design using what we have learned about its hydrodynamic characteristics. More investigation is needed to model the friction and adhesion forces between feet and the bottom substrate. The legs are a major contributor to lift and drag, indicating that reducing the height of the robot or creating more streamlined leg designs will improve robot performance. Developing increased levels of feedback control by incorporating additional sensing elements will allow the robot to better measure the surrounding flow. Having sensors mounted at different angles will allow the robot to determine the direction of flow. In addition, creating a waterproof enclosure to store the electronics and hydraulic components will allow the removal of the tether.

Active shaping of an underwater walking robot can generalize to many different systems. Other underwater crafts like ROVs and unmanned underwater vehicles (UUVs) could also benefit

from adaptable hydrodynamic characteristics. With active control of lift and drag on the body, robots can be more successful both moving and holding a constant position. Morphing structures have the potential to increase the efficiency of underwater systems.

Chapter 3, in full, is a reprint of the material as it appears in: Ishida M., Drotman D., Shih B., Hermes M., Luhar M., and Tolley M. T. (2019), "Morphing structure for changing hydrodynamic characteristics of a soft robot walking underwater", *IEEE Robotics and Automation Letters*, 4 (4), 4163-4169. The dissertation author was the primary investigator and author of this paper.

Chapter 4

Tuning the morphology of suction discs to enable directional adhesion for locomotion in wet environments

Reversible adhesion provides robotic systems with unique capabilities, including wall climbing and walking underwater, and yet the control of adhesion continues to pose a challenge. Directional adhesives have begun to address this limitation, by providing adhesion when loaded in one direction, and releasing easily when loaded in the opposite direction. However, previous work has focused on directional adhesives for dry environments. In this work, we sought to address this need for directional adhesives for use in a wet environment by tuning the morphology of suction discs to achieve anisotropic adhesion. We developed a suction disc that exhibited significant directional preference in attachment and detachment without requiring active control. The suction discs exhibited morphological computation—i.e. they were programmed based on their geometry and material properties to detach under specific angles of loading. We investigated two design parameters - disc symmetry and slits within the disc margin - as mechanisms to yield anisotropic adhesion and through experimental characterizations, we determined that an asymmetric suction disc most consistently provided directional adhesion. We performed a parametric sweep of material stiffness to optimize for directional adhesion and found that the material composition of the suction disc demonstrated the ability to override the effect of body asymmetry on achieving anisotropic adhesion. We modeled the stress distributions within

the different suction disc symmetries using Finite Element Analysis, yielding insights into the differences in contact pressures between the variants. We experimentally demonstrated the utility of the suction discs in a simulated walking gait using linear actuators as one potential application of the directional suction disc.

4.1 Introduction

Reversible adhesion, the ability to attach to and detach from a surface in a controlled manner, has gained specific interest in the field of robotics, ranging from manipulation to locomotion [133]. In the area of robotic locomotion, adhesion can be advantageous for generating traction (i.e. for maintaining contact between a robot and a surface throughout a walking gait cycle). Reversible adhesion can therefore enable unprecedented locomotion capabilities, such as scaling glass walls [134].

The adhesive strategies of animals have inspired a new generation of bioinspired adhesives to be paired with locomotion [135]. Many organisms employ adhesion to effectively locomote across a surface or to counter environmental disturbances. Animals ranging from lizards [136] to insects [137] use adhesive foot pads to walk on a wide variety of surfaces, including inverted surfaces. By coupling adhesion and locomotion, animals can attain novel locomotion strategies while countering high disruptive forces. For instance, sea stars locomote using hundreds of tube feet to contact and chemically adhere to a substrate [59]. This distribution of adhesion across a large quantity of attachment points allows echinoderms to locomote and remain attached to a substrate all the while countering wave surges, currents, and other marine disturbances. The coordination of a highly distributed network of actuators and adhesion allows sea stars to achieve a steady crawling locomotive gait [138]. Our goal is to develop a directional adhesive that could in the future enable sea star inspired locomotion while minimizing the complexity of control.

Reversible adhesives developed for use in engineered systems include microstructured dry adhesives, interlocking devices, electroadhesives, magnetism, phase-change based adhesives,

vibration-based adhesives, and negative static pressure devices (e.g. suction cups). Microstructured dry adhesives (i.e. gecko-inspired adhesives) take advantage of van der Waals forces to attach to a surface [139]. Previous work has used these adhesives to endow robots with wall-climbing capabilities [134, 140]. Roboticists have also explored the use of attachment devices composed of interlocking structures, ranging from rigid hooks [141] to *ex vivo* shark skin [142], on the foot pads of locomoting robots to provide greater frictional resistance to slippage while walking. Such interlocking devices may however limit the surface type to which locomotion would be successful. Electroadhesion based on electrostatic attraction between two surfaces has been used to achieve robotic locomotion [143], including on inverted and vertical surfaces [144]. However, the presence of water generally leads to weak electrostatic adhesion due to Debye shielding [145]. Adhesion using magnetism provides strong attachment during locomotion, yet is limited to ferromagnetic surfaces [146, 147]. Adhesion mediated by a material such as gallium that changes phase from solid to liquid at a temperature just above the robot's normal operating temperature allows for switchable attachment dependent on temperature [148]. Such adhesion occurs when a phase-change material partially covers and solidifies to an object once its temperature is decreased. Use of phase-change material to adhere requires control of its local temperature and may result in the deposition of residue. Additionally, adhesion generated by the vibration of a thin flexible membrane near a surface has recently been demonstrated for adhesion by mobile robots to curved, vertical, and inverted surfaces [149]. This vibration-based adhesion functions by forming a low-pressure region in a lubricating air film beneath the vibrating disk. However, this form of adhesion requires constant energy expenditure to attach and remain adhered to a surface and has not been shown to work in incompressible fluids (e.g. underwater). The use of suction has been explored in wall-climbing tasks in legged [150], tracked [151], and soft, inchworm-inspired [152] robots for use in air and underwater. However, suction discs currently used in locomoting robots are generally limited to use on smooth, flat surfaces and require active control for attachment and detachment [153].

In addition to reversibility, controllability of an engineered adhesive is critical for robotic

applications [154, 155]. Control can be achieved by including an actuator to engage with and detach from a surface or by morphologically programming the structure of the adhesive. Active actuation requires an energetic input to achieve attachment and detachment, thereby adding complexity to a design that could potentially reduce the scalability of a design to smaller sizes or larger number of adhesion points. An alternative form of adhesive control includes the use of morphological computation [156] to encode the conditions for attachment and detachment into the physical body of the adhesive. Morphological computation leverages the shape, design, and material composition to offload computational complexity into a physical structure of an object while producing a predictable behavior [157, 158, 159]. The use of morphological computation for adhesive control is not unique to engineered solutions but is also found in naturally occurring adhesive systems [156, 160]. For instance, geckos utilize a dense array of branched, anisotropic microstructures [161] to adhere via van der Waals forces [162]. Moreover, the setae of the gecko demonstrate sensitivity to angle such that once a threshold in angle is reached, the setae detach with minimal pull-off force [136, 162, 163]. Similarly, gecko-inspired adhesives developed with anisotropic profiles, such as angled stalks or wedges, result in directional adhesion in artificial systems [164, 165]. Pads expressing gecko-inspired adhesives can therefore be removed from a surface by peeling when adhesion is only required in one direction (e.g. in the case of climbing against gravity) [164]. The morphological computation exhibited by these microstructures therefore creates controllable adhesion without necessitating additional methods of actuation to attach to and detach from a surface [154].

Directional, microstructured adhesives which enable novel robotic locomotion are limited by the environment in which they are applied. Dry adhesives are most effective for adhering in dry environments and are significantly less effective in a wet environment. A thin, lubricating layer has been reported to form between a substrate and the tip of a dry adhesive microstructure when submerged in a water, leading to 50% lower pull off forces [166]. Modifications of the dry microstructured adhesives, such as the use of polymer coatings [167], changes to the material composition [168], and incorporation of cupped terminations [169], have been used to adapt the

microstructures for wet environments. These advances in microstructured adhesives have yielded strong normal and shear adhesion in a wet environment, yet lack anisotropy for directional adhesion or a controllable mechanism for detachment.

Many underwater creatures employ some form of reversible adhesion [170], including the use of chemical secretions in echinoderms [59], mechanical interlocking in the remora [171], and suction in the octopus [172] and intertidal fish [173]. Inspiration from these biological systems yield promising steps towards the development of successful engineered adhesives for use underwater [174]. Mechanical interlocking has been coupled with suction in the development of a biomimetic suction disc that is capable of withstanding high shear detachment forces [175]. Inspired by the clingfish, we have previously demonstrated the ability to modify the material composition of a suction disc to adhere to rough substrates [65, 176]. Soft artificial suckers inspired by the octopus [177] and an array of vacuum-driven suckers have demonstrated the utility of suction for underwater manipulation and locomotion [178]. However, these previous approaches to suction-based adhesion necessitated a separate, actively controlled mechanism to reversibly attach to and/or detach from a surface. In these studies, detachment required a separately controlled set of actuators to disengage the suction disc from a surface [179, 180]. For instance, detachment of the suction cups via peeling requires the outer perimeter of the disc to be lifted using tendons, thereby releasing the seal of the suction cup [150]. Other works have explored actively controlling the shape of the suction cup [152] or controlling pressure in a suction cup with a separate vacuum line for attachment and detachment, adding to the complexity of the pneumatic circuitry [181].

Here, we introduce a reversible suction disc that leverages morphological computation to detach at predetermined angles without necessitating a separate mechanism for detachment. Such a design would advance the field of directional adhesives, achieving anisotropic adhesion in a wet domain. We demonstrate that the detachment angle can be encoded into the body of the disc through a combination of factors - geometric asymmetry, disc margin morphology, and material stiffness. We generalized the types of design factors that yield directional adhesion

in suction discs and by applying the directional adhesives to linear actuators, we demonstrated their utility in sea-star inspired walking. To the extent of our knowledge, this work presents the first directionally adhesive suction disc to be reported and demonstrated for use in multi-legged robotic locomotion.

4.2 Results and Discussion

4.2.1 Testing two mechanisms for directional adhesion

We designed suction discs to achieve passive, reversible adhesion with adhesive strength based on the angle of applied tensile loading. We considered a sea star inspired walking scenario in which we attached the disc to the end of a linear actuator which was mounted to a body constrained to move parallel to the surface (Fig. 4.1b). To achieve translation of the body, we desired high adhesion at what we defined as a negative angle of the tube foot-inspired actuator relative to the body (angle, $< 0^\circ$), corresponding to a tube foot that had reached out and engaged its suction disc with a horizontal surface. After pulling on the surface to move the body forward, causing the actuator to pass through the neutral axis (angle, 0°), we desired low adhesion allowing the suction disc to release at a positive angle of the tube foot relative to the body (angle, $> 0^\circ$).

A suction disc was composed of a suction chamber that was lined by a disc margin (Fig. 4.1c), a design that we found previously to adhere well to surfaces with a variety of roughnesses in air and in water [65]. The disc margin was composed of silicone that was softer than that of the body cavity and served to seal the suction chamber against the substrate. A load was applied to the suction disc through a stem located at the top of the suction chamber. For all disc designs, the width of the disc (w) was twice the radius of the suction chamber (r) and the length of the disc (l) was four times the radius (Fig. 4.2a).

To compare various approaches to achieve directional adhesion, we investigated the role of two parameters – symmetry and slits within the disc margin – to achieve anisotropic adhesion (Fig. 4.2a-d). We then performed a parametric sweep of the material stiffness of the disc to

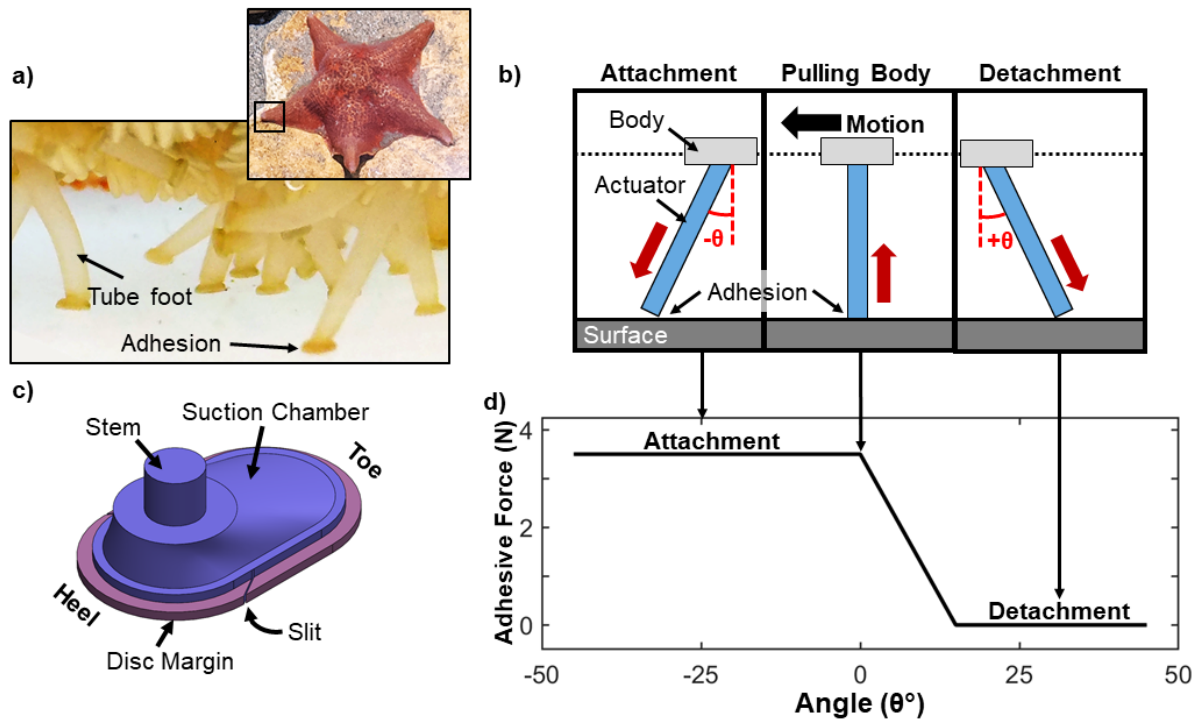


Figure 4.1. Tuning morphology for directional adhesion. Design parameters of a suction disc cause an adhesive force that is highly dependant on the direction of loading. a) Sea star inspired locomotion. Sea stars use an array of tube feet coupled with adhesive secretions to adhere and pull/push themselves along a surface. b) Schematic demonstrating idealized, angle-dependent attachment and detachment conditions for sea star inspired locomotion. c) Computer-generated rendering of suction disc, with key features labeled. d) Model of the idealized performance of a suction disc with adhesion mechanically “programmed” as a function of the angle of an applied tensile load (relative to vertical).

optimize anisotropic performance.

Parameter I: Symmetry for anisotropic adhesion

In the first set of prototypes, we varied the symmetry of the body of the disc. Symmetry was dependent on the location of the applied load, which we indirectly controlled with the position of the stem along the body of the disc. We then applied either a tensile or compressive load to the stem. We hypothesized that an uneven distribution of load across the body of the suction disc would adversely affect the seal around the disc margin for some (i.e. positive) angles of applied load relative to the surface, thereby reducing the adhesive stress. Accordingly, we

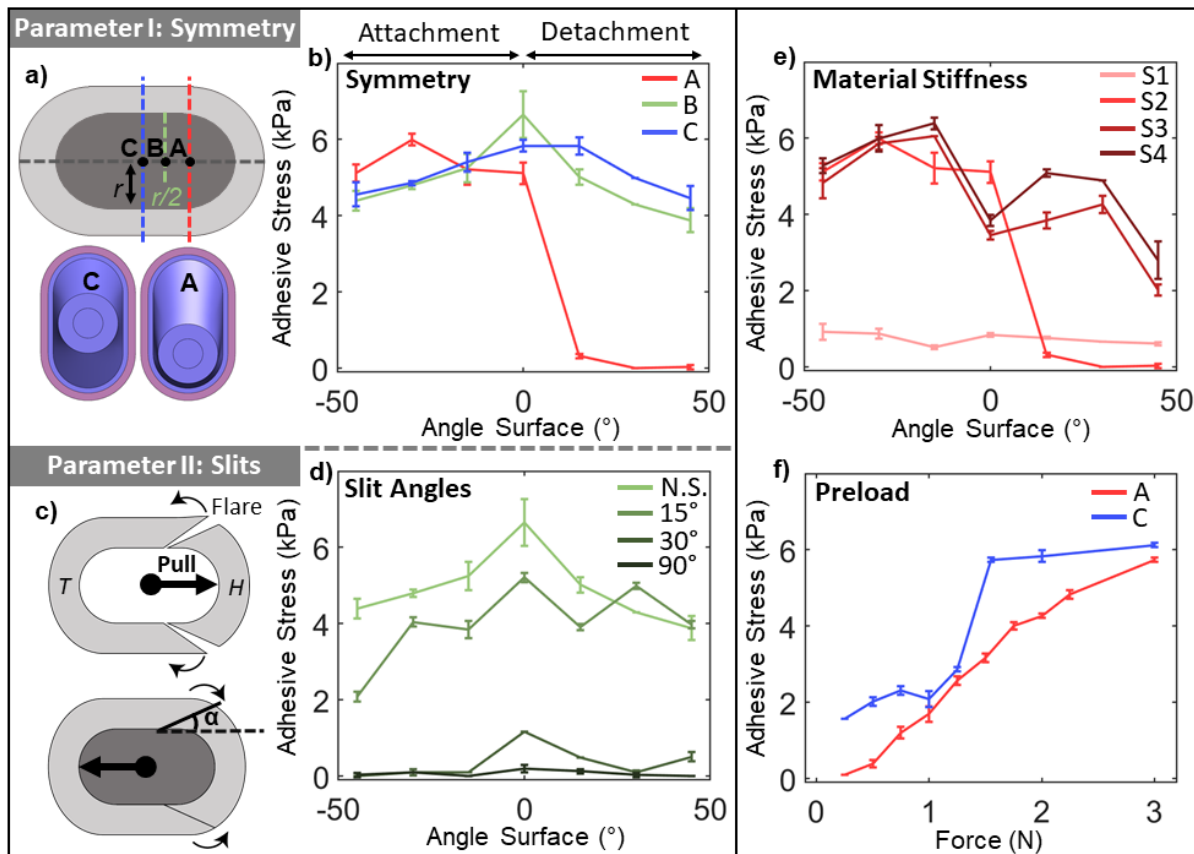


Figure 4.2. Experimental investigation into the morphological parameters for anisotropic adhesion. a) Investigations into the first parameter, disc symmetry, on anisotropic adhesion. We tested three possible load placements for suction discs: discs A and B were asymmetric, with loads offset from the center and discs C were symmetric, with a load applied to the center of the disc. b) Effect of disc symmetry on adhesion, where adhesive stress (kPa) is plotted with respect to the angle of the surface. c) Investigations into the second parameter, slits within the disc margin, on anisotropic adhesion. A schematic demonstrates the function of the slits. Top: Slits flare when the disc is pulled towards the heel, breaking the seal of the suction chamber. Bottom: Slits come together, forming a continuous seal, when the disc is pulled towards the toe. Representation of slit placement in the disc margin, angles with respect to the longitudinal axis. d) Effect of slit angle on adhesion (body type, B), where adhesive stress (kPa) is plotted with respect to the angle of inclination of the surface. The discs with slits were compared to a disc without slits (*N.S.*). e) Effect of material stiffness on adhesion for an asymmetric body type (A). Materials tested with platinum cured silicone with a moduli of elasticity at 100% strain of 68.9 kPa (S1, light red), 338 kPa (S2), 593 kPa (S3), and 662 kPa (S4, dark red). f) Effect of the magnitude of preload (N) on adhesion (kPa). Experiment performed on A and C body types (no slits). The angle of the surface relative to the discs was zero degrees for preload tests. All pull tests were performed in triplicate, error bars indicate standard deviation.

hypothesized that a greater offset of the load would result in a more pronounced asymmetric performance of adhesion.

The load placement ranged from the center of the disc (Body Type C) to offset from the center (Body Types A and B). For body types A and B, a load was applied to the stem which was offset by a distance of half the radius, ($r/2$, Body Type B) or by one radius (r , Body Type A) from the center of the disc (Fig. 4.2a). We refer to the positions of the load as either symmetric, for the centered condition, or asymmetric, for the offset conditions, about the transverse axis. To evaluate how the adhesive force generated by the discs varied with the direction of the applied load, we performed pull tests with a universal mechanical testing machine across the sets of suction disc variants. We changed the angle of the substrate with respect to the direction of travel of the mechanical testing machine.

We found that the symmetry of the body significantly affected adhesive stress as a function of angle (Fig. 4.2b). At negative angles of inclination in which attachment was desired, all three discs body types (A-C) exhibited significant adhesion (> 5 kPa), with only small differences in adhesive stress. All of the discs maintained adhesion across the neutral axis, perpendicular to the surface. However, the discs varied greatly on their performance at positive angles of inclination where detachment was desired.

The most asymmetric body type (A) with the largest offset had the largest difference in adhesive stress from attachment to detachment angles. Body Type A demonstrated nearly zero adhesive force in the angles associated with detachment. Conversely, the suction discs with a centered (Body Type C) and mildly offset load (Body Type B) maintained their adhesive strength (> 4 kPa) in positive angles of inclination, corresponding to the desired detachment orientations. Overall, a high degree of asymmetry resulted in a dependence on the angle of the loading (i.e. in directional adhesion).

Parameter II: Slits in the disc margin for anisotropic adhesion

In the second set of disc variants, we evaluated the effect of slits in the disc margin to yield anisotropic adhesion. The incorporation of slits in the disc margin was inspired by the clingfish, an intertidal fish that uses a ventral suction disc to attach to rocky surfaces [173]. The adhesive disc of the clingfish is formed by the union of the pelvic and pectoral fins, resulting in the formation of two bilateral slits in the disc margin. The clingfish can moderate the amount of suction by modifying the position of its fins [182], effectively changing the angle of the slits in its disc margin. Inspired by the clingfish, we included two slits in the disc margin to passively achieve directional adhesion. The slits were intended to flare (Fig. 4.2c) thereby disrupting the seal of the disc margin when pulled or loaded from specific angles. We varied the angles of the slits with respect to the longitudinal axis of the disc from 15° to 90° for a moderately offset body type (B).

Similar to our tests of adhesion based on disc symmetry, we tested the discs with slits with a universal mechanical testing machine at a variety of angles of loading relative to the surface to determine whether the slits contributed to anisotropic adhesion. We hypothesized that the addition of slits would act as a valve to facilitate direction-dependent adhesion. To answer this hypothesis, we compared designs with slits (angles; 15° , 30° , 90°) to the design without slits (0°) for body type B (Fig. 4.2d).

Overall, we found that the addition of slits did not yield the intended directional adhesion. The disc variant with a 15° slit in the disc margin adhered in an angle-dependent manner, but opposite of the anticipated adhesive curves. We observed that while the slits (15°) flared as anticipated while experiencing a compressive load, they did not fully close when pulled to form a completely continuous disc margin in the attachment orientation. The variant with slits of 15° exhibited directional adhesion, where the adhesive stress increased from 2.09 ± 0.12 kPa at -45° inclination to 3.98 ± 0.09 kPa at 0° and 45° inclinations. The magnitude of the dependency on the angle of the surface, however, was small. Thus while we were able to produce an anisotropic

adhesive response in a disc with slits, the difference in adhesive stress between a negative and positive angle of the surface was lower than alternative disc variants (i.e., changing the symmetry of the disc).

The variant with a slit of 30° achieved lower adhesive stresses in comparison to the disc with slits of smaller angles (15°). The slits of 15° exhibited more overlap in the disc margin, in comparison to the 30° variant. Our interpretation of these results is that the greater amount of overlap corresponded to a better seal and thus higher adhesive stress. This trend continued for the suction disc with a slit of 90°, for which no adhesion was achieved across all angles of inclination. We attributed the ineffective adhesion of the 90° slits to the inability of the disc margin to seal the suction chamber.

The incorporation of slits was a less reliable design parameter than asymmetry and was therefore less practical for applications in locomotion. During detachment, the slits were intended to flare open, dependent on the angle and direction of the pulling force (Fig. 4.2c), thereby reducing adhesion. However, the slits were more sensitive to the initial loading conditions, such as the alignment of the disc with respect to the surface and with respect to the clamp from the load cell. Suction discs that were misaligned to the slope of the experimental substrate would result in an uneven flaring of the slits (Fig.S1). This inconsistent behavior left slits either partially or fully closed, thereby keeping the suction chamber sealed during detachment.

We performed a quantification of the effect of misalignment on the overall adhesive stress of a disc (Body Type B) with slits (15 °). This disc was either inline (0°) or misaligned by 45° or 90° to the slope of the surface (Fig. S1 b). Given that the surface and the load cell were fixed in position, we created a misalignment by rotating the disc within the clamp of the load cell. The degree of misalignment directly affected the adhesive stress, where a 45° misalignment resulted in up to a 31% drop in adhesive stress (2.77 ± 0.05 kPa), in comparison to the disc when inline with the slope of the surface (4.04 ± 0.12 kPa). A 90° misalignment resulted in up to a 45% drop in adhesive stress (2.73 ± 0.07 kPa), when compared to the disc inline with the slope (4.99 ± 0.07 kPa). Thus, the adhesive performance of the discs with slits was highly dependent on its

alignment with the slope of the surface.

We clarified how the performance of the disc was affected by its misalignment with respect to the clamp by testing against a flat surface without a slope (0° ; Fig. S1 a). A misalignment (45° and 90°) of the suction disc relative to the clamp resulted in a $\sim 24\%$ reduction in adhesive stress for the disc against a flat surface. We attributed this to an uneven distribution of compressive stress across the body of the disc caused by its misalignment with the clamp (Fig. S1 b). Misalignment would non-uniformly deform the suction chamber of the disc. We observed that this uneven distribution of stress caused by misalignment with the clamp resulted in an uneven flaring of the slits and therefore a reduced adhesive stress.

The considerable sensitivity of the slits to alignment made them less reliable for practical implementation in a locomoting robot. Future work could explore the use of different materials or geometries of the slits to yield more predictable flaring that is less sensitive to misalignment. We anticipate that we could modify the location of the slits and orientation (i.e., 180° to their current orientation) to help tune their anisotropic adhesive performance.

In conclusion, of the design parameters investigated (symmetry and slits), the modification of the symmetry of the suction disc yielded the most predictable, repeatable anisotropic adhesion. We therefore chose to use a suction disc with a large geometric asymmetry (Body Type A) without slits for further experiments.

Impact of stiffness on anisotropic adhesion

We investigated the impact of material stiffness of the suction chamber on adhesion of a highly asymmetric suction disc (Body Type A), in which the offset load has already demonstrated the ability to yield anisotropic adhesion (Fig. 4.2e). We hypothesized that increasing the stiffness of the body of the suction disc would help to maintain the integrity of the suction chamber when deformed, allowing for greater adhesive stresses to be achieved. We changed the stiffness of the suction chamber while maintaining a constant stiffness of the disc margin. The types of silicone used spanned across one order of magnitude of stiffness (moduli of elasticity at 100% of strain

of 68.9 kPa for S1, 388 kPa for S2, 593 kPa for S3, and 662 kPa for S4).

We tested the discs of different stiffnesses on the universal mechanical testing machine by applying loads at different angles relative to the surface to determine how stiffness of the disc affects anisotropic adhesion. The relatively stiff elastomers, such as S4, adhered more strongly to a substrate in comparison to the softest elastomer tested (S1). However, stiff elastomers (S3 and S4) adhered with adhesive stresses greater than 5 kPa and 2.5 kPa for negative and positive angles of the surface, respectively. We considered this behavior to be insufficient anisotropy as we desired minimal adhesion at positive angles with respect to the surface. We found that by decreasing the stiffness of the suction chamber, the disc was able to preferentially, directionally adhere. We found that an intermediate stiffness (S2) of 338 kPa (100% modulus) demonstrated adhesion that corresponded to the angle of the surface (Fig. 4.2e). S2 adhered with a high adhesive stress (> 5 kPa) at negative angles and did not adhere (0 kPa) at positive angles, corresponding to the desired attachment and detachment orientations, respectively. However, we observed a limit to this trend as the disc composed of the softest of the silicones tested (S1) adhered with the lowest adhesive stress (< 1 kPa) across all angles of the surface. Thus, intermediate stiffnesses (0.38 MPa, S2) created directional adhesion, while the stiffest (> 0.5 MPa, S3 and S4) and softest (< 0.06 MPa, S1) elastomers did not produce both high adhesion at negative angles and low adhesion at positive angles. These results show that optimization of directional adhesion in suction discs requires a balance of material properties and geometric asymmetry.

We concluded that the differences in adhesive performances of the prototype variants resulted from the deformation experienced by the suction chamber. Decreasing the stiffness of the disc resulted in a reduced resistance to deformation, and a low structural integrity that compromised the suction chamber, resulting in low adhesive stress at all load angles. In contrast, increasing the material stiffness of the disc reduced the deformation under the same compressive load, avoiding the collapse of the suction chamber.

This is consistent with previous work [183], which found that increased stiffness of the

suction chamber increased the adhesive force of the disc. However, to create directional adhesion, the disc must create minimal adhesive forces under certain loading conditions, dependent on the angle of the surface. A disc composed of high stiffness material would thereby create high adhesion forces at all angles of detachment. For predictable, directional adhesion, the suction chamber must be of an intermediate stiffness to be compliant enough to collapse the front of the suction chamber during detachment while being stiff enough to maintain its integrity during attachment. We envision that additional optimizations of the structure of the discs could be used to combine the effects of shape and material stiffness on the directionality of the adhesion.

Impact of preload on symmetric and asymmetric discs

Lastly, we tested the effects of preload on the adhesion of symmetric and asymmetric discs using a universal mechanical testing machine to first load the disc against a surface perpendicular to the axis of travel of the machine and then pull the disc away from the surface. The geometric asymmetry affected the amount of force that should be applied as a preload to achieve the maximum adhesive force (Fig. 4.2f). The preload caused the disc to deform, which forced fluid out from the enclosed chamber and created a pressure differential responsible for adhesion. As the force of the preload increased, the adhesive stress increased until the disc was fully deformed and the maximum pressure differential was reached. After this point, a further increase to the preload resulted in a minimal increase of the adhesive stress, as demonstrated in the symmetric suction disc. Conversely, the increasing preload for the asymmetric disc led to a gradually decreasing slope, resulting in a point of inflection in the curve around 3 N. We observed that the symmetric disc achieved an inflection point in the maximum adhesive stress at about half the preload required by the the asymmetric disc (1.5 N for Body Type C, 3 N for Body Type A; Fig. 4.2f). We concluded that the reduced preload required by the symmetric disc was due to a more uniform deformation of the disc. Conversely, the asymmetric disc required a greater amount of force to fully evacuate the suction chamber as the shorter heel of the disc was more resistant to deformation.

4.2.2 Contact mechanics at discrete angles during loading

To understand why different discs demonstrated orientation-dependent adhesion, we imaged the contact made between the suction disc and a surface during preload and pull-off conditions using frustrated total internal reflection (FTIR; Fig. 4.3a). FTIR is a contact-visualization technique in which light is internally reflected within a sheet of acrylic [184]. Contact with the acrylic sheet allows light to escape, which can then be imaged by a camera and serves as an indicator of contact with a surface. However, FTIR does not provide the magnitude of the contact pressure, only whether or not there is contact with the surface.

During FTIR, both asymmetric (A) and symmetric (C) discs were imaged under a 2 N compressive load when the imaging surface was rotated to -30° , 0° , and 30° with respect to the suction disc. We then imaged the contact at the point of failure (*PoF*) of the suction disc when pulled from the imaging surface at a displacement rate of 150 mm/min.

As visualized during compressive trials using FTIR, the symmetric disc always maintained a seal between the disc margin and the substrate, irrespective of the angle of the surface (Fig. 4.3a). At both -30° and 30° rotations, a full preload of 2 N caused the outer perimeter of the disc margin to flare upwards, thereby reducing the area in contact with the imaging surface but still retaining the seal around the perimeter of the disc. This flaring behavior was not observed in the zero degree condition, suggesting a more uniform distribution of stress along the perimeter of the disc margin. Additionally, a compressive preload of 2 N caused the suction chamber to deform such that the inner surface of the top of the suction chamber (beneath the stem) contacted the imaging surface, shown as a circle in the frames from FTIR (arrow; Fig. 4.3a). We interpreted the contact of the top of the suction chamber with the imaging surface to be indicative of the strain in the disc; that is, a larger area of contact with the upper cavity implied a larger deformation of the disc.

The behavior of the asymmetric disc when in contact with the surface differed from the symmetric disc. At a negative angle of inclination, the asymmetric disc completely sealed its

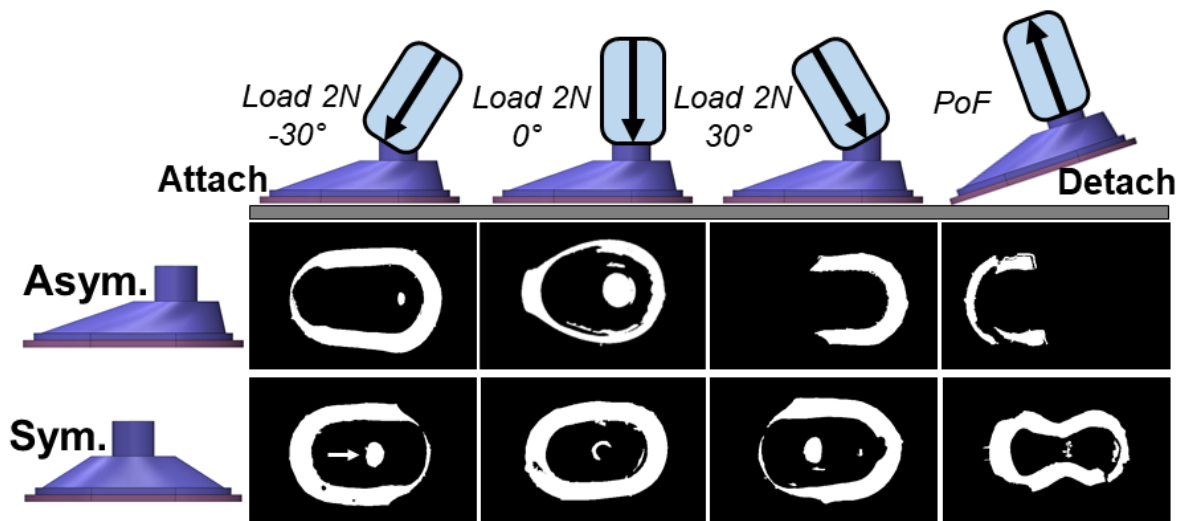


Figure 4.3. Visualizing the contact between a suction disc and a surface. a) Visualization of the contact area of the asymmetric disc (Body Type A, top row) and symmetric disc (Body Type C, bottom row) for four angles of contact using frustrated total internal reflection (FTIR). Column 1: a compressive load of 2 N was applied to the suction disc on a surface at an angle of -30° . Column 2: a compressive load of 2 N was applied to a disc perpendicular to a surface. Column 3: a compressive load of 2N was applied to a disc at an angle of 30° . Column 4: the suction disc was then pulled away from the surface (angle, 30°), FTIR images correspond to the point of failure (PoF), or the moment before the disc detached from the surface. For all FTIR images, the white regions indicate contact with the imaging surface.

suction chamber. However, when loaded in compression from a positive angle (the low adhesion orientation), the asymmetric disc did not maintain a full seal. When loaded by a compressive force in this orientation, the front of the disc lifted from the surface, while the heel was still in contact with the surface. As the suction disc was gradually pulled away from the surface in this orientation (first decreasing the magnitude of the compressive force to zero, then increasing the tensile load), the contact of the asymmetric disc would roll from heel to toe. Thus, at positive angles of inclination, the asymmetric disc did not adhere because the suction chamber was not sealed and hence did not maintain a pressure differential.

The FTIR results showed that a compressive preload concentrated about the heel of the asymmetric suction disc resulted in adhesion to a surface. However, as the compressive load changed to being centered about the toe, the front of the disc would lift and thereby break the seal of the suction chamber. We concluded that asymmetry resulted in an uneven distribution of stress across the disc, corresponding to reduced adhesion at angles associated with detachment in a locomotive gait cycle. On the other hand, symmetry yielded high adhesion, irrespective of if the load was centered over the heel or the toe.

4.2.3 Modeling mechanics and contact throughout a gait cycle

The FTIR results provided an understanding of the behavior of the discs when loaded at discrete angles against an imaging surface. However, when in use during a walking gait, the disc would be subjected to loading under a continuous change of angles relative to the surface (see Fig. 4.1). To examine the behavior of the disc during a gait cycle, we used finite element analysis (FEA) to model the effects of body symmetry (Types A and C) on the mechanics due to loading while cycling from an angle of -30° to an angle of 30° . (Fig. 4.4). To simulate the angle change, we loaded the suction discs to a virtual surface that rotated about an axis orthogonal to the stem and the long axis of the suction disc. The simulations neglected environmental conditions and effects of the fluid in the suction cavity and focused on how contact with the surface affected the mechanics of the disc.

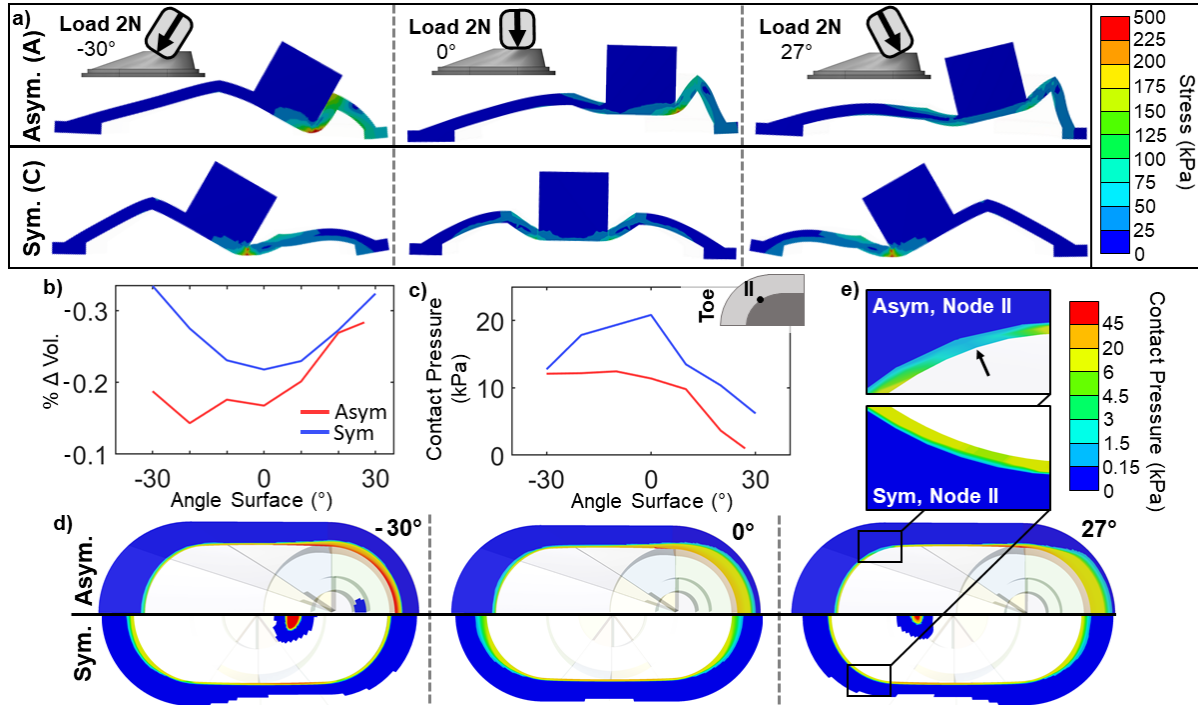


Figure 4.4. Finite Element Analysis to model the mechanics of adhesion of a suction disc while attached at various angles of attachment and detachment. a) Top panel: Visualization of the distribution of Von Mises stress (kPa) across a vertical cross-section through the center of suction discs A. Stress plotted when a load (2 N) was applied at an angle of -30° , 0° , and 30° . Bottom panel: Stress plotted for a symmetric suction disc C when a load (2N) was applied at an angle of -30° , 0° , and 30° . b) Plot of percent reduction in the internal volume within the suction chamber with respect to the internal volume for the case of no preload, as a function of the angle of the surface. Measurement of internal volume performed at seven angles during the simulation. c) Plot of the contact pressure (kPa) of node II, located along the innermost perimeter of the disc margin, with respect to the angle of the surface. Measurement performed at seven angles during the simulation for both asymmetric (red) and symmetric (blue) discs. d) Results from FEA visualizing contact pressure (kPa) of the suction disc with respect to angle of the surface. e) Inset images of Node II for the asymmetric (top) and symmetric (bottom) discs. Node II was determined to be the location of lowest contact pressure for the asymmetric disc (see SI Fig. 4 for details).

Distribution of stress within the body of the discs

The distribution of stress within the body of the suction disc differed between the body types (Fig. 4.4a). The symmetric disc (C) exhibited a symmetric distribution of stress with respect to the angle of the applied preload. Furthermore, the symmetric disc experienced a symmetric change in internal volume across angles tested in the simulation (Fig. 4.4b). Conversely, the asymmetric disc (A) experienced a greater concentration of stress within the body (> 175 kPa) during the angles associated with attachment ($<0^\circ$) than in comparison to the angles associated with detachment ($>0^\circ$). The stress was concentrated at the heel when loaded at -30° , which was distributed throughout the body of the suction disc when rotated. The asymmetric disc experienced the greatest reduction in internal volume at angles associated with detachment ($>0^\circ$; Fig. 4.4b). A low internal volume corresponded to the collapse of the front of the asymmetric suction disc ($>0^\circ$; Fig. 4.4a).

Distribution of contact pressure along the disc margin

We simulated the spatial distribution of contact pressure around the disc margin for the asymmetric (Body Type A) and symmetric (Body Type C) discs (Fig. 4.4c-e). The minimum contact pressure around the inner perimeter of the suction chamber provided a measure of the integrity of the seal of the suction chamber [183] (i.e. localized points of low contact pressure indicate a low adhesive strength). The asymmetric disc experienced a contact pressure that was nonuniform across the inner perimeter of the disc margin. A compressive preload on the asymmetric disc generated a high contact pressure on the heel of the disc and lower contact pressure at the toe, which was a consistent trend across all angles tested (Fig. 4.4d). In contrast, the symmetric suction disc demonstrated a more uniform distribution of contact pressure across the inner perimeter of the disc margin for all angles of inclination of the surface. To quantify the integrity of adhesion throughout the motion simulated, we probed five nodes along the inner perimeter of the disc margin, ranging in position from the toe to the heel (Fig. S5). We found that the node along the arc transitioning from the toe to the middle of the suction disc (Node

II) experienced the lowest contact pressure (0.9 kPa) for the asymmetric suction disc at 27° inclination of the surface (Fig. 4.4c). Visually, this region of localized low contact pressure can be compared between the symmetric and asymmetric disc cases (Fig. 4.4e). The minimum contact pressure of the asymmetric disc dropped from 3.6 kPa at a 20° inclination to 0.9 kPa at 30° of inclination. In comparison, all nodes for the symmetric disc experienced a contact pressure that was greater than 5 kPa across all angles of inclination of the surface. The symmetric disc had a comparatively higher minimum contact pressure (5.6 kPa) across all angles of the simulation in comparison to the asymmetric disc, and most notably during positive angles of inclination. Overall, we concluded that angles of inclination of the surface $>20^\circ$ were shown through simulation to be predictive of low adhesion for the asymmetric disc due to localized points of low contact pressure.

Modeling to inform anisotropic adhesion

To successfully predict directional adhesion of a suction disc using a computational model, we found it important to characterize both the internal stresses and contact pressures of a disc rather than the change in internal volume. From our FEA model, we found that a change in volume, which is generally a predictor for adhesion using suction cups, was not a good indicator of directional adhesion. Adhesion of a suction cup is caused by a pressure differential between the internal suction chamber and the ambient fluid. The maximum limit of adhesion would correspond to when all the fluid is expelled from the internal chamber during preload. By this logic, a suction disc would adhere better given a larger decrease in internal volume during preload.

However, we found this that this heuristic did not accurately predict adhesion due to directional loading. In our FEA model, the asymmetric suction disc had its greatest change of internal volume at angles that were experimentally determined to result in no adhesion to the surface. Predicting suction disc performance by the change in internal volume would oversimplify the mechanics involved in directional adhesion. As previously found, adhesion is

also dependent on the contact pressure between an adhesive and a surface [183]. For a suction disc, contact pressure is a function of various parameters, including geometry, deformation due to preload, material stiffness, and size. Thus, investigating the differences in spatial distribution of contact pressure between the discs in simulation allowed us to better predict their behaviors.

From the combination of the results from FTIR, FEA, and pull test experiments, we concluded that a disc would detach when the minimum contact pressure along the innermost perimeter of the disc margin in contact with a surface dropped to near zero. As demonstrated by the asymmetric disc, although it underwent large internal changes in volume, the disc did not adhere due to a low contact pressure around the rim of the disc. Given that the quality of the seal is only as strong as its weakest point, when the contact pressure around the innermost perimeter of the disc margin dropped to near zero, this corresponded to a compromised seal, allowing the pressure of the fluid inside the suction chamber to equilibrate with the surrounding fluid. An understanding of the changes in internal volume (determines theoretical maximum adhesion) coupled with changes in contact pressure distribution (determines ingress of fluid into the disc) were required to provide a more complete understanding of the anisotropy of adhesion. Using this information, we can design a disc to have a nonuniform contact pressure to design for greater directionality in suction discs.

4.2.4 Adhesion-enabled locomotion

To demonstrate sea star-inspired adhesion-based locomotion, we incorporated the directional suction discs into a proof-of-concept walking system. We attached a suction disc to the end of a pneumatic linear actuator (a syringe) attached by a rotational joint to a linear slider (with a counterweight to reduce the effects of friction on the slider). The syringe—which plays the role of the tube foot of the sea star (see Fig. 4.1)—was free to rotate with respect to the slider and could be made to extend and contract with air pumped into/out of the syringe by an off-board programmable syringe pump [132]. To simulate sea star-inspired walking, we started the syringe at one end of the linear track with an initial angle, θ , relative to the vertical (Fig. 4.5a). We then

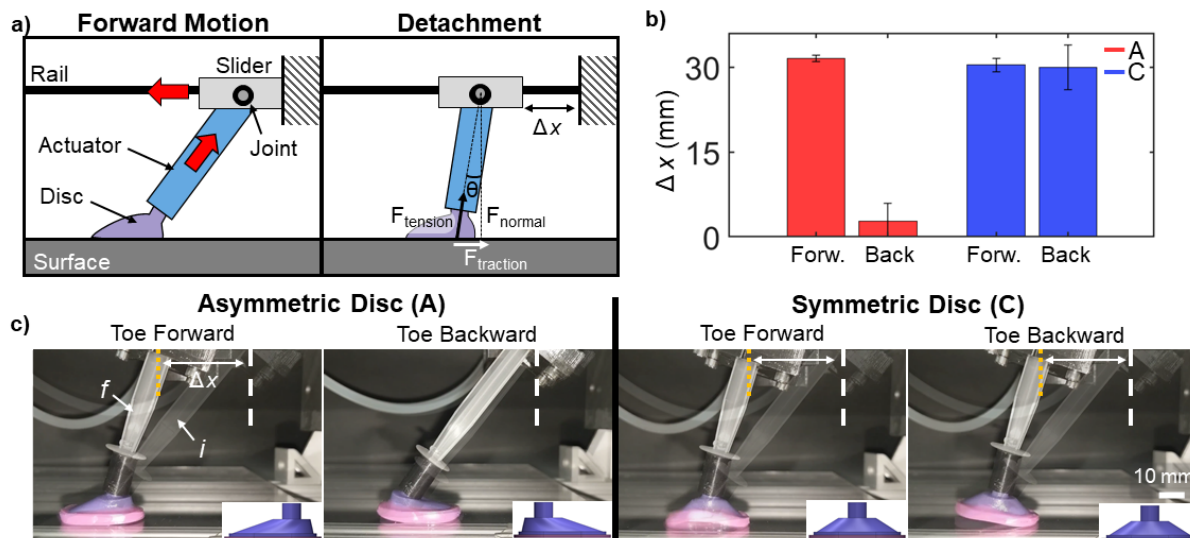


Figure 4.5. Employing suction discs for sea star inspired adhesion-based locomotion. a) Schematic of experimental setup. A suction disc attached to the end of a pneumatic linear actuator (a syringe) engaged with a surface, and upon contraction of the actuator, served as an anchoring point to pull the body forward. The translated distance (δx) was measured from the initial position at the start of the linear track to its final position upon detachment of the suction disc. The tensile force ($F_{tension}$) was composed of the component of force in the direction of motion ($F_{traction}$) and the component normal to the surface (F_{normal}), dependent on the angle (θ) of the actuator. b) Bar graph of the distance traveled by the body (δx) while varying the orientation of the suction disc. The suction disc was either oriented with the toe in the direction of motion (“Forw.”), or with the heel in the direction of motion (“Back.”). Asymmetric disc (A) shown in red; symmetric disc (C) represented in blue. Trials performed in triplicate, error bars represent standard deviation. c) Images from the locomotion demonstration. An image of the initial position of linear actuator (i) was overlaid onto the image of its final position (f). Scale bar, 10 mm.

extended the syringe until the disc contacted and preloaded against a smooth acrylic surface, generating adhesion. Subsequent retraction of the syringe pulled the slider forward along the track (given sufficient friction at the disc to prevent the disc from slipping along the surface).

We found that the symmetric suction disc and the asymmetric suction disc in the attachment orientation (toe facing the direction of desired locomotion) were both able to adhere to the surface and remain adhered to pull the slider forward (Fig. 4.5b) before detaching at approximately the same angle. As the angle θ approached zero, the component of the tensile force in the direction of motion also approached zero ($F_{traction} = F_{tension} \sin \theta$), while the component

normal to the surface increased ($F_{normal} = F_{tension} \cos \theta$), eventually leading to adhesion failure. However, when the asymmetric disc was attached in the reverse orientation (heel facing the direction of desired locomotion), the disc created negligible motion along the track before pulling off of the surface due to the directionality of the asymmetric disc.

We further demonstrated that this walking capability can be extended to take multiple steps with a second syringe mechanism (Movie S1). With a single disc, subsequent extensions of the syringe to create a preload force also pushed the slider backward since it was no longer at the start of the track. However, if a second disc was adhered at the same time, the second disc could react the preload force on the first disc. With the two disc-syringe pairs actuating out-of-phase, one disc was always adhered to the surface when the other was being preloaded, resulting in forward locomotion. Note that this locomotion gait bore some similarity to adhesion-based locomotion observed in sea stars, although sea stars typically walk using hundreds of tube feet (instead of two), using a gait in which each tube foot contracts only once per three steps of the sea star [185].

We demonstrated that the directionality of the adhesive disc is useful for creating a walking motion (Movie S1 and Fig. 6). In this demonstration, we adhered one disc to the surface and used it to pull the slider forward on the track, stopping when the disc was about to detach from the surface (as described above) and the syringe was close to vertical. Then, without continuing to actuate the front syringe, we extended the rear syringe to adhere the rear disc to the surface, and pulled the slider forward. This forced the front syringe to continue to rotate toward the vertical position while still in contact with the surface. We took two steps with the rear syringe to ensure that the front syringe was rotated to the detachment angle. We ended the rear step just before the rear disc detached from the surface and slightly retracted the front syringe. This slight retraction was enough to pull the asymmetric disc from the surface to restart the gait cycle, while the symmetric disc remained attached to the surface, inhibiting further motion.

The overall locomotion speed of the robot during the demonstrated gait cycle was 0.98 mm/s with the asymmetric discs and 0.94 mm/s with the symmetric discs, both with a 2.5 mm/s

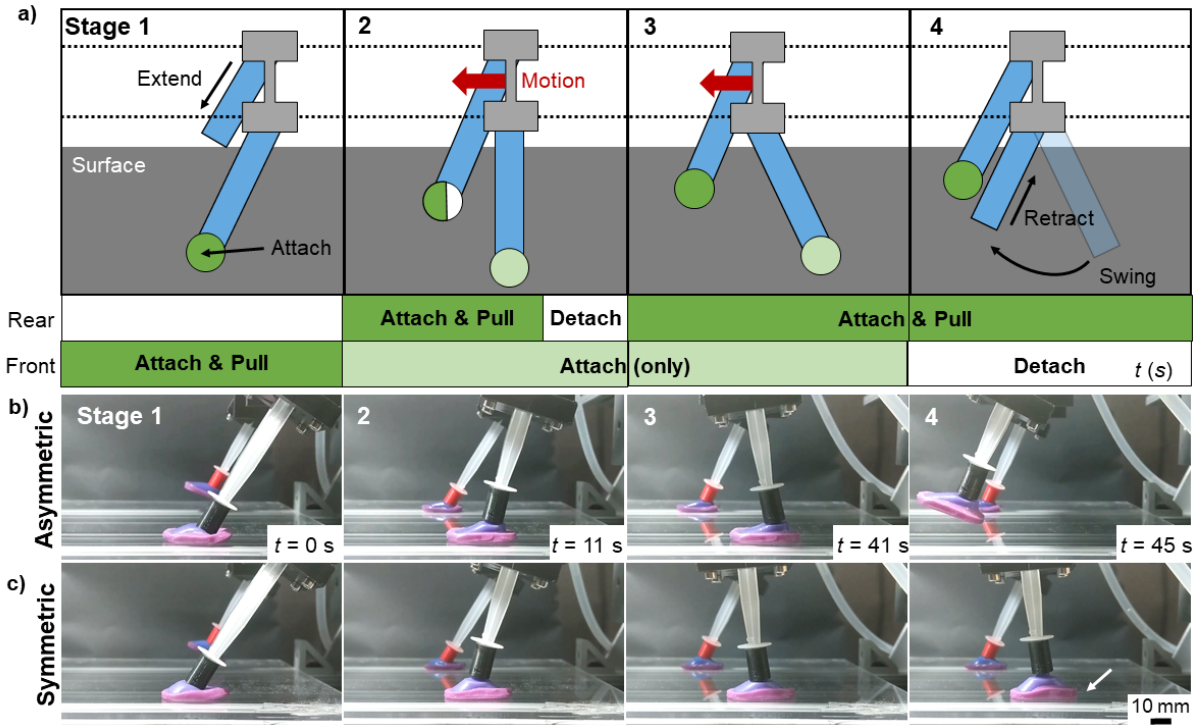


Figure 4.6. Demonstration of the use of directional adhesion in multi-legged sea star inspired locomotion. a) Schematic of a multi-legged gait cycle where locomotion is aided by the programmed detachment of the suction disc. Stage 1) The front disc is preloaded against a surface, resulting in attachment. The front actuator pulls on the disc, resulting in forward translation. 2) After the front actuator has been pulled forward, a second disc attached to the rear actuator is preloaded against the surface. The rear actuator is retracted, causing the the body to move forward and eventually detach. 3) The rear actuator is extended again to engage the suction disc with the surface, pulling the body forward for the second step. This second step pulls the front actuator into the preprogrammed detachment angle. 4) The front disc disengages from the surface and allows for retraction of the front actuator, restarting the walking gait cycle. b) Image sequence of the multi-legged gait cycle for the asymmetric disc. The front suction disc detached from the surface in stage 4, returning to its initial position at the start of the gait cycle. c) The image sequence of the multi-legged gait cycle for the symmetric disc. The front suction disc did not detach from the surface in stage 4, given the same degree of retraction as the asymmetric disc (i.e. more effort, or active control of adhesion, would be required to reset the front actuator to its original position). Scale bar, 10 mm.

retraction speed of the syringe.

We further demonstrated similar performance of these discs in a locomotion scenario where the discs were submerged in 1.5 inches of water (Movie S2 and Fig. S7).

This demonstrated that the asymmetric disc was beneficial for sea star inspired legged locomotion because it can predictably detach from the surface with reduced effort as compared to symmetric discs.

In robotics, when scaling the use of adhesion to a large array of actuators, control complexity becomes critical. By adding to an actuator a suction disc that can conditionally adhere, we have demonstrated that we can offload part of the complexity required to control the system into the morphology of the suction discs. Minimizing the force required for detachment places lower force requirements on the actuators that engage the discs with the surface. The use of directional suction discs is also scalable. Because the suction discs do not require additional actuators for adhesion, we can envision more easily scaling to arrays of many small suction discs controlled by many actuators, to achieve locomotion similar to the sea star.

In addition, the size of the suction disc can be scaled down to be closer to the size to the tube foot of a sea star (*Asterias rubens*; diameter, $\sim 1300 \mu\text{m}$; length, up to 20 mm [59]). Although the sea star uses chemical adhesion to attach to surfaces [59], we took inspiration from its large array of adhesive tube feet used to achieve locomotion. For an robot of many actuators, we can envision smaller discs with similar geometric ratios, appropriately scaled wall thicknesses, and analogous material stiffnesses to behave similarly to those discs presented in this work.

Large arrays of actuators have the potential to provide provocative abilities to locomoting walking robots in both wetted and submerged domains. For instance, a locomoting robot that will be subjected to directional flow may need to be stabilized to shear forces. Our current designs have not been optimized to withstand shear forces, yet such a goal may be achieved through an array of suction discs with appropriate coordination. Other environmental parameters, such as surface roughness, may be accounted for by the material softness of the disc margin, which has

been demonstrated to allow for attachment to rough surfaces such as sandpapers [65].

While we have yet to fully characterize the walking performance of the robot over macroscale surface features, we anticipate that the discs would be effective against uneven, inclined, and coarse surfaces. We have demonstrated in previous work [65] that the use of a soft, elastomeric layer on a suction disc allowed for high adhesion to irregular (i.e., concave) and rough surfaces (i.e., coarse sandpaper). Given that we have designed these anisotropic suction discs with a soft elastomeric layer in the disc margin, we would expect these discs to provide high adhesion to uneven and irregular surfaces.

Overall, the development of a directional suction disc can be applied to provide locomoting robots with traction in a wet environment, while minimizing actuation complexity.

4.3 Conclusion

Directional adhesives that exhibit morphological computation can reduce the complexity of control in robotic systems. In this work, we presented a way to design directional adhesives to adhere based on angle in a wet environment. We demonstrated that we can tune the performance of the suction disc by modifying the symmetry of the body, material composition, and incorporation of slits in the disc margin. Careful selection of body asymmetry, in coordination with material stiffness of the suction discs, produced the most successful and repeatable form of directional, anisotropic adhesion.

By tuning the morphology of the adhesives, we incorporated behaviors (i.e. attachment/detachment at appropriate points in a gait cycle) into the body of the suction disc that would otherwise necessitate controlled actuation. We demonstrated that the suction discs can be applied to a linear actuator to achieve a pulling motion, helping to pull a body forward as mechanism for locomotion inspired by the sea star. Based on the approach and analyses presented here, future work could use these anisotropic suction discs to enable sea star inspired robots capable of robust locomotion in wetted and submerged environments to achieve traction and novel gaits

with minimum system complexity.

4.4 Materials and Methods

4.4.1 Fabrication of the discs

We designed the suction discs using computer-aided design (Solidworks, Dassault Systems). We modified the disc symmetry, material stiffness, and presence of slits in the disc margin to determine which were successful in yielding directional adhesion. Across all prototype variants, the constraining dimensions of the body remained constant. The footprint of the suction chamber was an oval of 16 mm diameter, 28 mm length. The suction chamber was terminated by a disc margin that was 1 mm thick, 1.5 mm offset from the footprint of the suction chamber. The height of the suction chamber was 5.5 mm across all variants. We designed the discs to have cylindrical handles of 5 mm height, 6 mm diameter to provide a gripping surface during adhesive pull tests. For experiments varying the symmetry of the discs, we fabricated two asymmetric discs (Body Type A and B) and a symmetric disc (Body Type C). The asymmetric discs varied by degree of asymmetry. Body type A had the largest degree of asymmetry, where the upper cavity was centered at one full radius from the center of the suction disc (Fig. 4.7c). The upper cavity of Body Type B was centered at one half the radius from the center of the suction disc. The upper cavity of Body Type C was located directly above the center of the suction disc.

We manufactured the suction chamber using a platinum cured silicone with an elastic modulus at 100% strain of 338 kPa (Dragon Skin 20, Smooth-On, Inc.), which we dyed with silicone pigment (Silc-Pig, Smooth-On, Inc.). The main body of the suction discs across all prototypes were composed of this silicone, except for those manufactured to test the impact of material stiffness on adhesion, in which case we fabricated a suction disc of Body Type A with a suction chamber composed of silicone of 100% modulus of 662 kPa (MoldStar 30, Smooth-On, Inc.), 593 kPa (Dragon Skin 30, Smooth-On, Inc.), 338 kPa (Dragon Skin 20, Smooth-On, Inc.), or 68.9 kPa (Ecoflex 00-20, Smooth-On, Inc.). Each silicone was dyed with a pigment

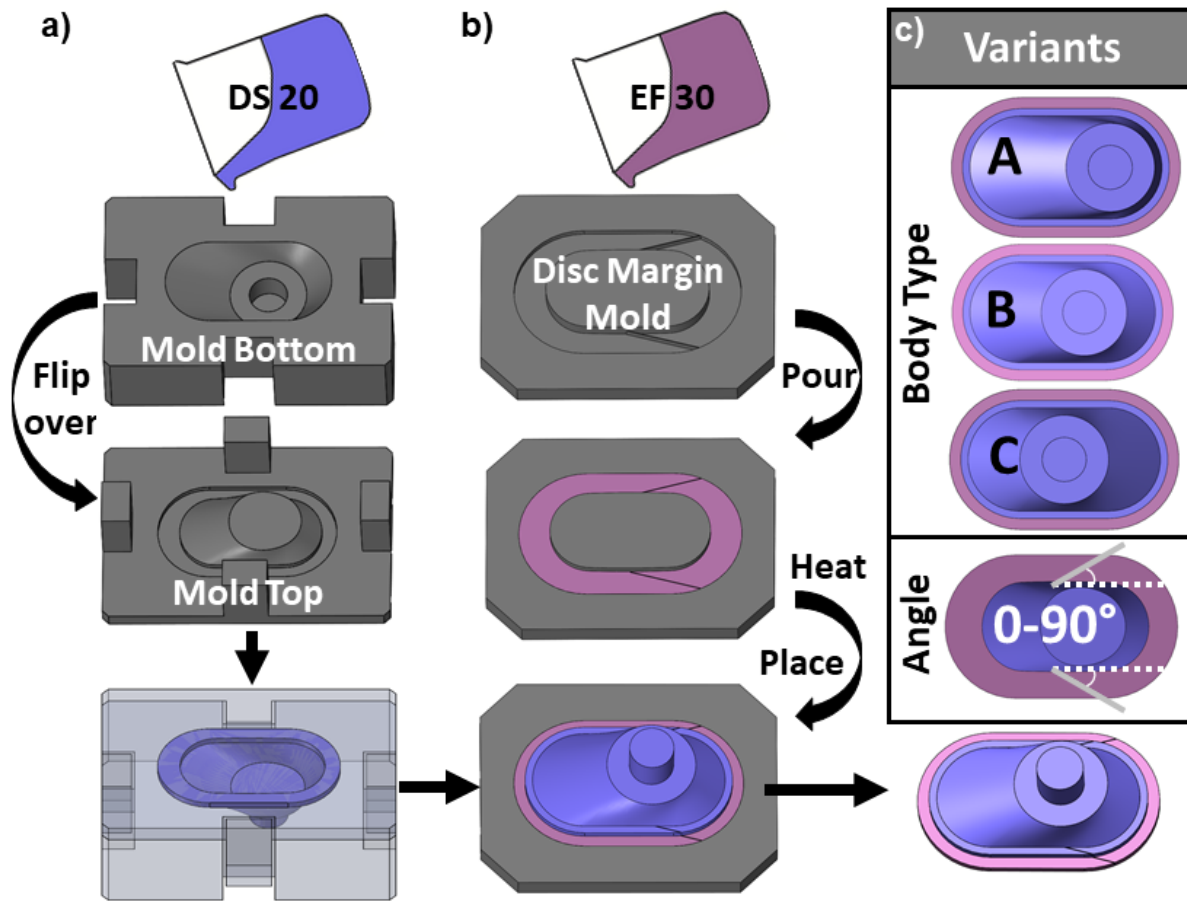


Figure 4.7. Fabrication of the suction discs. a) Molding process of the suction chamber using Dragon Skin 20. b) Molding process of the disc margin, using EcoFlex 20. c) Variations of the suction disc based on body type and angle of slits in the disc margin.

corresponding to its stiffness. Lastly, we varied the presence and angle of slits in the disc margin. The slits were angled at either 15° , 30° , or 90° with respect to the longitudinal axis.

For each disc variant, we fabricated the molds using a rigid, photocurable resin (VeroClear, Stratasys Inc.) in a multimaterial 3D printer (Objet350 Connex3, Stratasys Inc.). To ensure the parts were fully cured, we aged the molds in an oven at 40°C for 4 hours. The molds containing uncured silicone were degassed in a vacuum chamber for 10 min and then fully cured in an oven for 1 h 30 min at 40°C (Fig. 4.7a). We then added a soft layer of silicone to the disc margin to provide a sealing layer, following the approach described in previous work [65]. To apply a soft layer, we first partially cured a mold of the elastomer (Ecoflex 00-30, Smooth-On Inc.) at 40°C for 3 min, then applied the suction disc backing to the mold (Fig. 4.7b). We then fully cured the assembly for 1 hr at 40°C .

4.4.2 Experimental evaluation of adhesion

We experimentally tested the adhesives at a fixed velocity. We conducted the pull tests using a universal tensile testing machine (force gauge, 100 N limit, 0.02 N resolution; M7-20, Mark-10 Co.). We mounted the handles of the discs into a clamp that was then held in the upper grips of the tensile testing machine. All pull tests were performed against an angled acrylic plate (angles; 0° , 15° , 30° , 45°) in a tank of water (Fig. 4.8). We engaged the suction disc to the acrylic surface with a preload of 2 N. We performed the pull tests in triplicate, using a rate of retraction of $150\text{ mm}\cdot\text{min}^{-1}$ for all prototypes and trials. The adhesive stress was calculated by normalizing the adhesive force by the surface area of the footprint of the suction disc. We evaluated the effect of preload on the different body symmetries. We varied the preload between 0.25 N and 3 N for body types A and C at angles of inclination of -30° and 0° .

4.4.3 Imaging contact

We imaged the contact of the suction disc with a surface using FTIR [184]. The setup of the FTIR station was custom-built, where a 9.7 mm thick acrylic plate internally reflected the

light emitted from diodes (natural white light-emitting diodes, 3528-24VDC, Super Bright LEDs, Inc.) that were mounted along the perimeter of the plate. The FTIR plate was statically angled at either -30° , 0° , or 30° to visualize contact throughout three distinctive phases of the gait cycle (Fig. S2 a). To remove background noise, we dyed the suction discs black using silicone pigment (Silc Pig, Smooth-On, Inc.). We imaged the acrylic surface using a camera (1280 X 780 pixels, 140 pixels cm^{-1} , 40 frames per second, EXILIM EX-FH25, Casio Computer Co., Ltd.). The suction discs were engaged with the surface to a preload of 2 N, and the surface was wetted during the FTIR trials. When the surface was angled to 30° of inclination, we retracted the upper grip of the mechanical testing setup at a rate of $150 \text{ mm}\cdot\text{min}^{-1}$, thereby pulling the suction disc from the imaging surface. The point of failure (PoF) was determined to be the last frame of the image sequence during which the suction disc was adhered to the imaging surface.

4.4.4 Modeling the mechanics of directional adhesion

Finite Element Analysis (FEA) was performed using ANSYS Mechanical Version 2019R1. We experimentally determined the material properties of Dragon Skin 20 by performing a tensile test (3342, Instron Inc.) and fitting the Yeoh 3rd order hyperelastic model to the experimental data. Parameters for the Yeoh 3rd order model (C10, C20, C30, D1, D2, D3) were 99 161 Pa, -1604 Pa, 1065.2 Pa, 0 Pa^{-1} , 0 Pa^{-1} , and 0 Pa^{-1} , respectively. Due to the bilateral symmetry of the suction discs, we modeled half of the suction disc using symmetry boundary conditions in FEA to reduce the computation time. The suction discs were predominantly meshed using 20-node brick elements with an average element size of 0.5 mm. The suction discs were preloaded on an inclined steel plate to obtain a vertical reaction force of $\approx 0.28 \text{ N}$. Frictionless contact was assigned between the suction discs and the steel plate. We neglected the effects of the change in fluid pressure inside the cavity of the suction disc as the plate was rotated. We performed a quasi-static simulation and neglected the effects of surface energy and friction at the interface of the suction discs and the steel plate. Simulating the attachment of the suction disc at a -45° angle of the plate, corresponding to the angle of the surface in the experimental setup, is

complex due to the large-scale deformation, in addition to the contact and material non-linearities required to model the physics of the suction disc. The simulation for the attachment of the suction disc at an angle of the plate of -45° was unable to converge in our case. Hence, we simulated the suction disc to attach to a plate that rotated from -30° (attachment) to 30° (detachment). The angle of inclination for the steel plate was then varied from -30° to 30° with the horizontal (with $+10^\circ$ increments) and the response of the suction discs was recorded. The vertical reaction force, strain energy, Von-Mises stress, deformed shape, contact pressure, and contact status was recorded for variation in the angle of the steel plate between -30° to 30° with 10° increments. The volume of the internal cavity of the suction disc as the plate was rotated was calculated numerically. The internal surface of the suction disc cavity was extracted using Meshmixer 3.3. This extracted surface was then imported to Unity 5.6.7f1 and the volume enclosed by the cavity was numerically calculated.

We quantified the contact pressure of five nodes along the inner perimeter of the suction disc (Fig. S4). We probed the contact pressure at the nodes along the plane of symmetry intersecting the inner perimeter (Fig. S4, Node I and Node V), the node along the axis of rotation of the plate intersecting the inner perimeter (Fig. S4, Node III), and the nodes where the geometry of the inner perimeter transitions from a straight line to a circular arc (Fig S4, Node II and Node IV).

4.4.5 Demonstration of locomotive application

The locomotion demonstrations were performed using a linear slider with Delrin surfaces sliding on an extruded aluminum rod. For the single-syringe demonstrations, a counterweight of 37 grams on a pulley was attached to the slider to counteract friction between the slider and the rail. The syringe was driven using a fluid transmission from an offboard motor and lead screw (part number). The syringe was extended to the surface at $5 \text{ mm}\cdot\text{s}^{-1}$ to preload the disc, then retracted at $2.5 \text{ mm}\cdot\text{s}^{-1}$ to create the forward motion of the slider.

For the double-syringe demonstrations in air, the counterweight was increased to 47.3

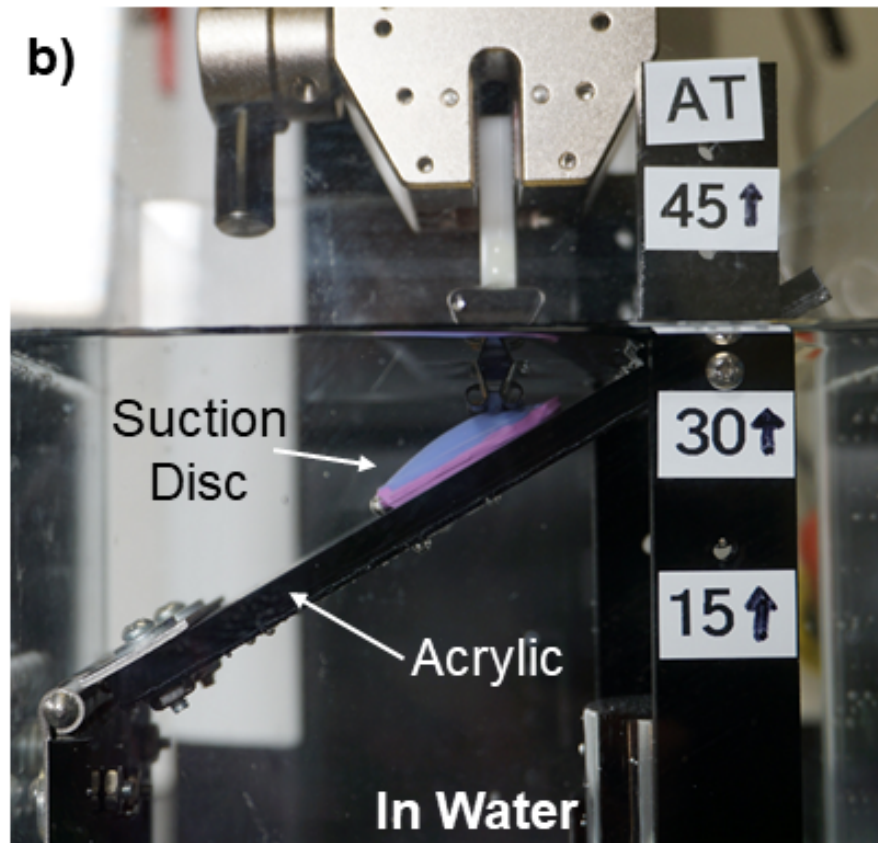
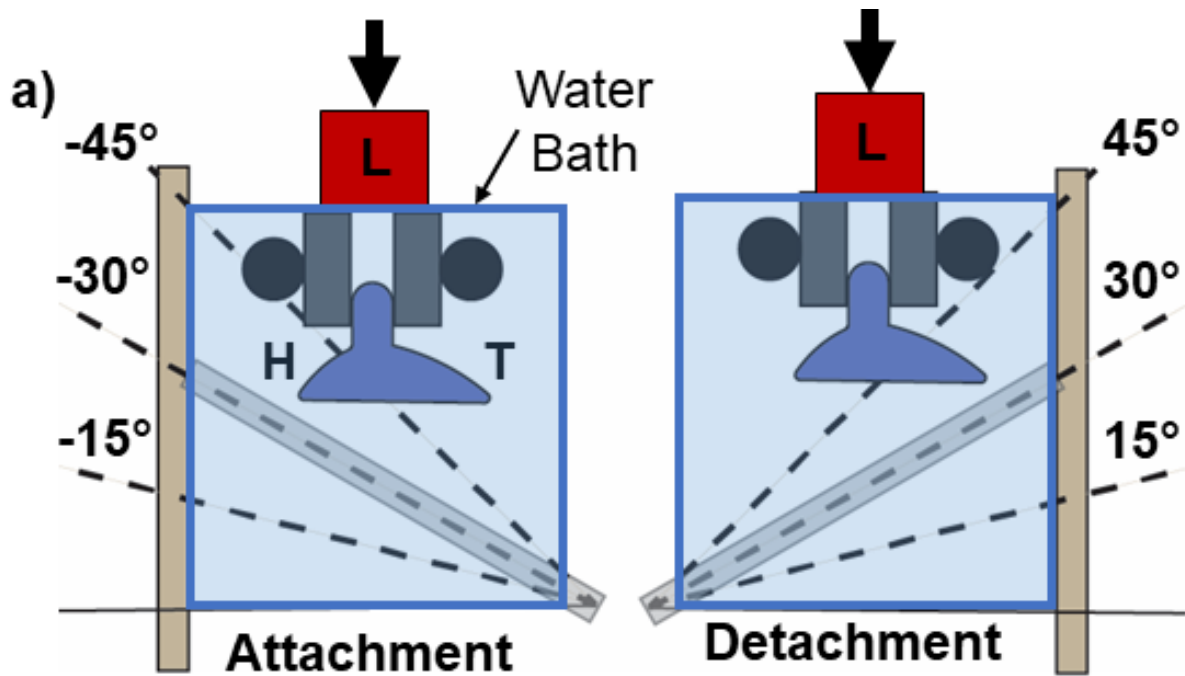


Figure 4.8. Experimental setup for characterization of adhesion. a) Schematic demonstrating that each adhesion test was performed in a water bath against an acrylic surface. *H* denotes heel, *T* denotes toe of the suction disc. b) Image of experimental setup.

grams to account for the additional friction in the system. The second syringe was mounted on the slider free to rotate with respect to the slider and the first syringe and was driven by a second motor and lead screw. In this demonstration, the first syringe was extended and preloaded against the surface and then retracted. The second syringe was then extended and preloaded against the surface and retracted the same amount as the extension. The second syringe was then extended and preloaded again, retracted until the first syringe passed the crossover point, and then the first syringe was retracted a small amount to attempt to detach the disc from the surface.

For the submerged double-syringe demonstrations, the front syringe was extended and preloaded against the surface and then retracted to pull the body forward. The rear syringe was then extended and preloaded against the surface and retracted the same amount as the extension, to again pull the body forward. The front syringe was then retracted a small amount more to attempt to detach the disc from the surface.

Chapter 4, in full, is a reprint of the material as it appears in: Sandoval J. A.*, Ishida M.*, Jadhav S., Huen S., Tolley M. T. (2022) "Tuning the morphology of suction discs to enable directional adhesion for locomotion in wet environments", *Soft Robotics*, in press. The dissertation author was the co-primary investigator and co-first author of this paper.

Chapter 5

Locomotion via active suction in a sea star-inspired soft robot

Some marine animals, such as sea stars, have developed versatile adhesive appendages that can be used for a variety of behaviors including sticking to surfaces, manipulating objects, and locomoting. These appendages couple reversible adhesion capabilities with muscular structures that can do work on the world while still being soft enough to conform to various surfaces and to squeeze through tight spaces. We took inspiration from the hydraulic tube feet of sea star to create modules consisting of soft active suction discs and soft pneumatic linear actuators. Tube feet convert fluid motion into linear actuation using soft tubes that are constrained radially. In this work, we study the tradeoff between the stiffness of such radial constraints, and the ability of the linear actuators to apply axial forces. The adhesive force of the suction disc is dependent on both the pressure differential between the suction cavity and the environment and the deformation within the body of the disc while it is being loaded. We show that the tube foot modules are capable of creating locomotion over flat surfaces, up small steps, and in a confined space due to the redundancy caused by an array of actuators. We also show that active suction not only enables the use of softer tube foot actuators, but that sensing this active suction line provides feedback to increase the efficiency of locomotion over obstacles.

5.1 Introduction

Mobile robots are currently used underwater for performing a variety of tasks that are challenging for humans to do, such as exploring the deep ocean or repairing pipelines. However, these existing systems are often large, noisy and disruptive to the environment, and require significant power expenditure to maintain a constant position in flow [186]. This makes it difficult for them to interact with delicate objects like coral reefs [187], to nonintrusively study sensitive organisms [188], or to perform long duration static measurements [189]. Many small benthic animals that live on submerged surfaces such as coral reefs or tide pools use appendages to walk over a variety of terrains and reduce their energy expenditure compared to swimming in tides or currents [109, 190].

We take inspiration for an underwater walking robot from the sea star, an invertebrate that can walk on inclined, inverted, and rough surfaces using numerous tube feet on the under sides of its arms. These tube feet are closed hydraulic systems that can extend when pressurized and bend and point in all directions to create omnidirectional locomotion [191]. Each tube foot has a disc on its distal end that secretes a chemical to attach the disc to the surface and a de-adhesive chemical to detach the disc when the tube foot needs to move [192, 59]. Each individual tube foot can produce on the order of 0.2 N adhesive force and 0.04 N pulling force, and the sea star can coordinate its tube feet to walk up a vertical surface or pry open of shells for feeding [193]. When not using adhesion, the sea star can use a “bouncing gait” in which it uses its tube feet to push its body upward and forward [194] and then contracts its tube feet suddenly to fall forward [195].

Inspired by nature, the subfield of soft robotics leverages the compliance of soft materials to adapt to a variety of environments and situations [196, 197]. Soft robots have infinite degrees-of-freedom and can take advantage of their material properties to adopt a wider range of configurations than would be possible with traditional robotic designs [124]. As a result, robots composed of soft materials have demonstrated advantages for addressing complex tasks such

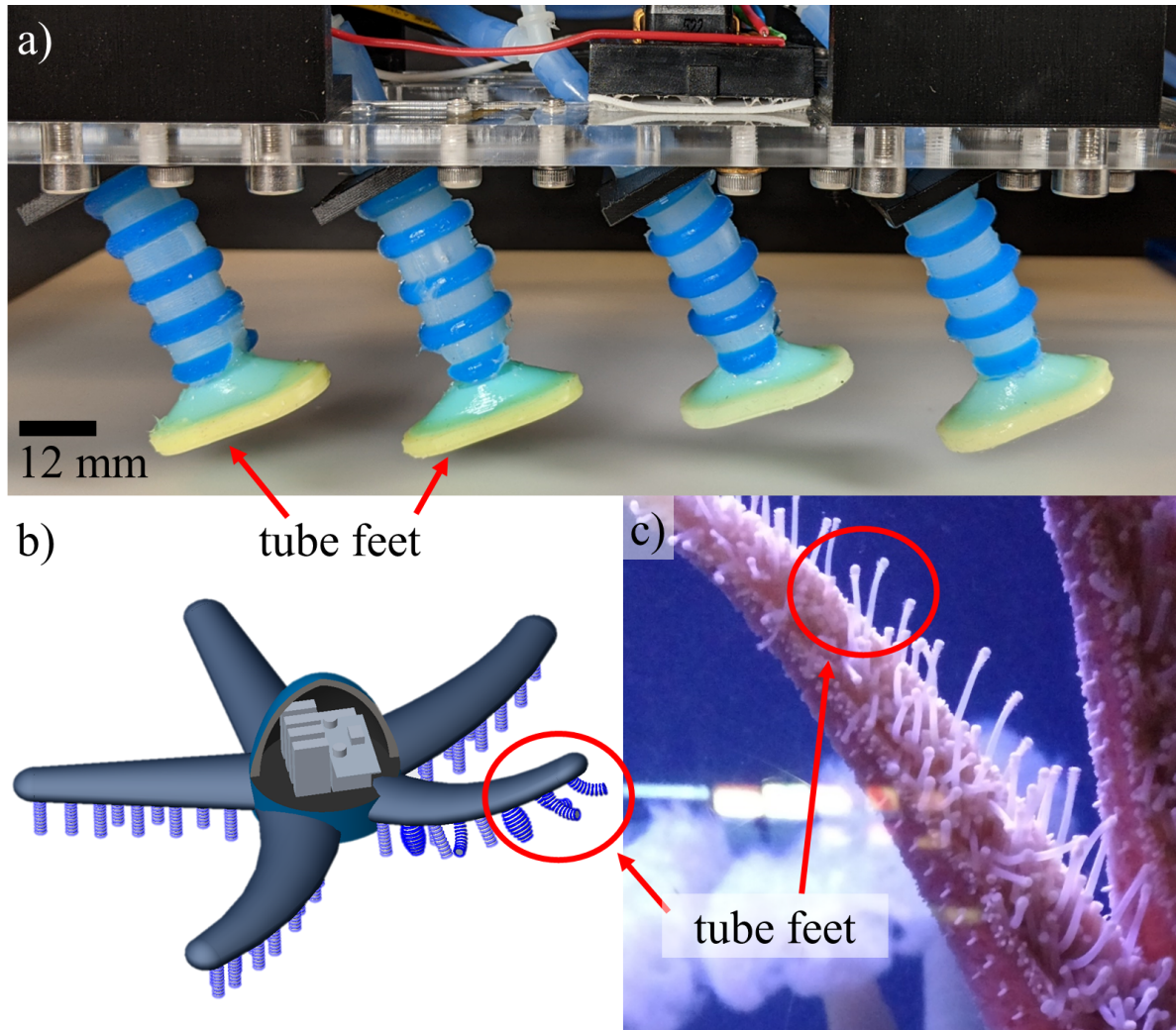


Figure 5.1. Biological inspiration and experimental prototypes for robot capable of locomotion using an array of soft tube feet. a) Our platform for demonstrating sea star inspired robotic locomotion, consisting of four tube foot modules mounted to a rigid body on a tethered rail system. b) Conceptual rendering of the sea star inspired robot that consists of many soft robotic tube foot modules arranged along its arms. c) An arm of the sea star, which was the inspiration behind the soft robotic tube foot modules.

as the manipulation of irregular shapes [125, 198], locomotion through unknown and variable environments [199, 200], and the creation of motions and abilities mimicking those of animals [201, 202]. Soft legs have shown promise for walking robots, as soft actuators can bend into a variety of different configurations that would require many joints to replicate in a rigid system [26]. In particular, a fiber-reinforced actuator, which consists of a hyperelastic material with an internal chamber that deforms when internal fluid pressure is applied [203], is well-suited for replicating the behavior of a tube foot.

Adhesion-based locomotion has been previously demonstrated in mobile robots. Robots inspired by climbing lizards like the gecko use microscale structures that manipulate van der Waals forces to climb smooth surfaces [155, 204]. Electroadhesion has been commonly used in small-scale applications where reducing robot mass is critical [205, 206]. Robots designed for climbing ferrous surfaces, such as the hulls of ships or gas tanks, have used magnets for locomotion [207, 146]. Other mobile robots have generated reversible adhesion using suction cups [151, 152]. However, these previous approaches all have limitations. Artificial gecko-inspired adhesives use van der Waals forces and are not suited for use underwater. Magnets and electroadhesives only adhere to ferrous surfaces and conductive surfaces, respectively. Commercial suction cups adhere best to smooth surfaces like glass or acrylic and not the rough surfaces often found in nature. However, we have previously shown that multimaterial soft passive suction discs are able to conform to some surface asperities, allowing limited adhesion [65].

In this work, we present an investigation into the key components necessary for creating a soft walking robot inspired by the sea star. We combine a soft actuator with a soft active suction disc to create a module similar to the sea star's tube foot that enables adhesion-based locomotion. We study how the design of the soft actuators affects the usage of the suction discs for locomotion. We further examine the advantages of active suction discs over passive ones when used with soft actuators. Finally, we demonstrate that a robot using an array of these actuators can compensate for failures of individual modules to traverse obstacles.

In Section 5.2, we describe the design and fabrication of the tube foot-inspired actuator modules. In Section 5.3, we discuss the mechanical properties of these modules, and in Section 5.1, we demonstrate the capabilities of these actuators and their ability to enable the traversal of varied terrains by creating a sea star-inspired soft robot. Finally, in Section 5.5, we present our conclusions and future work for developing an adhesion-enabled walking robot.

5.2 Actuator Design and Fabrication

Our hypothesis was that we could create adhesive based locomotion by using an extension actuator to reach forward when pressurized to press against the surface and engage adhesion. The actuator would then contract and the adhesive element would react the contractile force to pull the robot forward. Inspired by the tube feet of the sea star, we created a soft tube foot module that consists of a soft suction disc and a soft, pneumatic linear extension actuator (tube foot actuator). Although sea stars use chemical adhesion and not suction to adhere to surfaces [208], we chose to model adhesive-based locomotion with suction to avoid damaging or altering the surface.

5.2.1 Design and fabrication of suction discs

Suction discs produce adhesion by creating a pressure gradient between the internal suction cavity and the ambient pressure around [209]. This pressure gradient creates a net force downward on all surfaces of the disc. The maximum adhesion force of the disc is determined by the pressure gradient, which determines the maximum possible force, and the contact pressure between the disc and the surface, which determines the quality of the seal. If the contact pressure is low, the seal will break and disc will detach because of fluid ingress into the suction chamber before the theoretical maximum force is reached. Here, we investigate the effects of active suction on the performance of a soft suction disc to determine if an active or passive suction disc is more suitable for use with a soft tube foot actuator.

The suction discs were made of two different silicone elastomers. The suction chamber

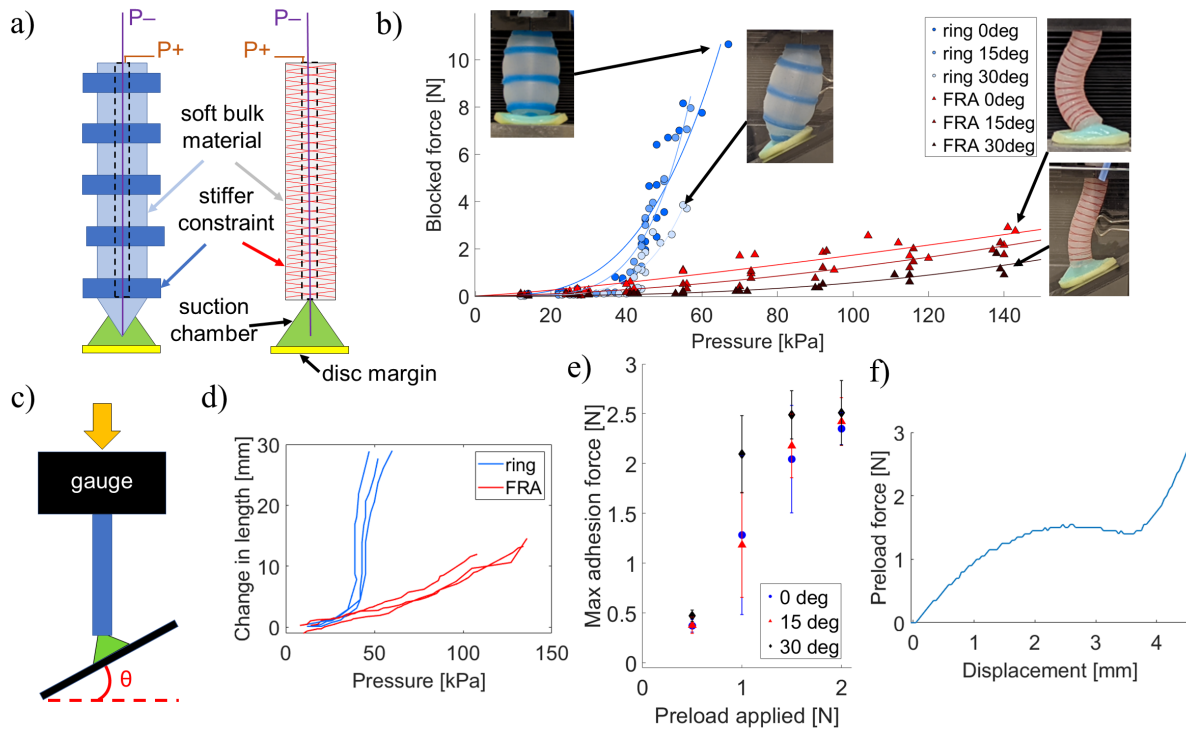


Figure 5.2. Characterization of the two types of tube foot actuators. The ringed actuators provided higher blocked force to preload passive suction discs, but had a nonlinear correlation between pressure and length. a) Schematic of the two extension actuator designs. b) Measured block force for the two actuator types against surfaces of varying inclinations (0° , 15° , 30°). The fiber reinforced actuators buckled much more easily than the ringed actuators, resulting in lower blocked forces, especially at higher pressures. c) Schematic of setup for measuring the blocked force of the actuators against surfaces with varying inclinations. d) Relationship between input pressure and the change in length for the fiber-reinforced actuators (red triangles) and the ringed actuators (blue circles), where each curve is the pressure to length relationship for an individual actuator. e) Relationship between the applied downward preload and the maximum adhesion force of the passive suction disc. Error bars indicate the standard deviation of the $N=3$ data. f) Preload force as a function of disc displacement, indicating that the maximum change in volume of the disc occurs at around 2 N.

was made from a relatively stiff elastomer (DragonSkin 30; Smooth-On, Inc., 100% modulus: 593 kPa) and is 16 mm in diameter and 28 mm in length, lofted to a height of 5.5 mm tall. The softer disc margin (Ecoflex 00-30, Smooth-On, Inc., 100% modulus: 69 kPa), a thin 1 mm strip of material at the bottom of the suction chamber, formed the seal with the substrate. This dual-material design was based on our previous work [65, 210] that showed that a stiff suction chamber created more contact pressure with the substrate to maintain a seal, but a soft disc margin allowed the disc to conform to small-scale roughness of the surface. A cylindrical stem (6 mm diameter) at the top of the suction chamber fit into the end of the tube foot actuator, and a thin tube was routed through the stem to provide active suction pressure. The discs were bilaterally, but not radially, symmetric so that the disc was less likely to deform out of the plane of the walking motion of the robot.

We molded each suction disc in multiple steps, consistent with previous work [65]. First, we molded the suction chamber from the stiff silicone elastomer and let the material fully cure. We then poured the softer elastomer into a different mold for the disc margin. We partially cured this layer in an oven for two minutes and then placed the suction chamber on top, thereby bonding the disc margin to the suction chamber as it fully cured. Lastly, we inserted a thin silicone tube into the top of the suction disc and sealed the tube in place using a silicone adhesive (Silpoxy; Smooth-On, Inc.).

5.2.2 Design of tube foot actuators

We previously showed that the adhesive force of soft, passive suction discs were dependent on the preload applied to force fluid out from the disc [210]. In that work, we used rigid linear actuators to produce a high preload to ensure that we created a sufficient pressure differential at the cost of the compliance and adaptability that soft actuators are known for. In this work, we investigated two different designs of soft tube foot actuators to replace the rigid appendages: a soft tube with stiffer, but still extensible, constraining rings, and a fiber-reinforced actuator.

The extension actuators used in this work extended when positive pressure was applied internally and relied on the elastic restoring force in the soft material to contract to their initial lengths when pressure was removed. Each actuator was 40 mm in length with a 12 mm outer diameter and 6 mm inner diameter. The ringed actuators had a stiffer silicone rubber (DragonSkin 30; Smooth-On, Inc.) cured in rings on the outside of the tube made from the more flexible silicone (Ecoflex 00-50; Smooth-On, Inc.). The distal ends of the actuators were tapered along one plane to create an ankle joint by reducing the bending stiffness of the actuator at that location (Fig. 5.2a). This ensured that when the tube foot actuator approached a surface at an angle, the attached disc rotated with respect to the actuator to seal the disc against the surface.

The fiber-reinforced actuator consisted of a hollow cylinder composed of silicone (DragonSkin 30; Smooth-On, Inc.) with thread wrapped around in a helical winding of 3° . The inner chamber of the fiber-reinforced actuators was offset from the center axis by 0.5 mm, which caused it to bend toward the thinner side when inflated, to improve the seal of its associated suction disc against a surface.

We fabricated the ringed actuators in a two-step process. We first molded and fully cured the inner cylinder and then used a second mold to cast the stiffer rings on the outside. Similarly, we made the fiber-reinforced actuators by first molding and fully curing the soft cylinder before winding threads on the outside to form the radial constraint layer. We then sealed the threads in place by depositing a thin layer of silicone on the outside. For both actuator types, we inserted the stem of the disc into the end of the actuator and sealed it with silicone adhesive. Finally, we routed the thin pneumatic tubing from the suction disc through the center of the actuator and sealed the tube to a wye fitting at the inlet of the actuator. The pneumatic lines for suction to the disc and pressure to the actuator were therefore fully independent.

5.3 Experimental Results and Discussion

5.3.1 Importance of actuator force

We hypothesized that active suction would be necessary to use soft actuators with limited force output such as fiber-reinforced actuators. To determine the force that the soft actuators were able to produce to press the suction disc against a surface, we measured the blocked force of each actuator. During the proposed walking gait (see Section IV), the tube foot actuators were angled forward so that when pressurized, they reached in front of the robot to pull the body of the robot forward. To simulate this angled position, we measured their blocked force against both flat and inclined surfaces. With the disc starting flush against the surface, we input known volumes of air into the actuator and measured both the pressure in the tube foot and the blocked force applied to the surface (Fig. 5.2c).

Because the ringed actuators expanded radially when pressurized, they had a much higher buckling strength (i.e., proportional to their area moment of inertia) than the fiber-reinforced actuators. At pressures around 60 kPa, the ringed actuators transmitted over five times as much force as the fiber-reinforced actuators, which do not expand radially and thus had a lower buckling strength (Fig. 5.2b). We found that, for the fiber-reinforced actuators, over 120 kPa of input pressure was required to generate 2 N of blocked force. In addition, the blocked force of all actuators decreased as the slope increased, indicating that, during a walking motion, it was increasingly difficult to generate forces as the actuators were pointed further forward.

We also measured the length of the actuators as a function of input pressure (Fig. 5.2d). We measured the length of the ringed actuators linearly, and we measured the length of the asymmetric fiber-reinforced actuators as the arclength of the curved profile. We observed that initially, both actuators increased in length similarly, indicating a similar stiffness. However, the ringed actuator exhibited the well-known balloon instability at a pressure around 40 kPa, at which point it continued to extend in length at an almost constant pressure. This behaviour was caused by the simultaneous expansion in both the radial and axial directions which reduced the

wall thickness enough to significantly reduce the effective stiffness of the tube. This balloon instability would introduce challenges for controlling the length of the actuator as it would require very fine control of the pressure to control the length of the actuator. The fiber-reinforced actuator, in contrast, did not expand radially, and thus did not exhibit this ballooning behavior, and consequently had a roughly linear relationship between length and internal pressure.

In previous work, we characterized the preload force required to engage suction while using a suction disc without active suction [210]. To determine if our tube foot actuators could be used with passive suction discs, we measured the adhesion strength of our suction discs without applied vacuum pressure at different preloads. We performed pull tests on a universal testing machine (M7-50 force gauge 250 N capacity, 0.05 N resolution; Mark-10, Inc.) where we lightly touched the disc to the surface so that it was just able to create a seal without deforming the disc. We applied an active vacuum to confirm that the disc created a seal and then detached the vacuum, pinching off the vacuum line and allowing the suction chamber to return to ambient pressure. We zeroed the gauge and used the universal testing machine to press the disc against an angled acrylic surface with a prescribed preload of varying magnitude. The universal testing machine then pulled the disc upward at 25 mm/min and measured the maximum adhesion force before the disc detached from the surface.

We found that the maximum adhesion force of roughly 2.5 N occurred in response to a preload of 2 N for all angles (Fig. 5.2e). During preloading, we observed that initially the preload deformed the structure of the disc, forcing air out of the inside of the suction chamber. However, as the preload increased and the shape of the suction chamber went from concave down to mostly flat, a maximum preload was reached at which point additional preload only compressed the material of the disc. The preload force then rapidly increased as the sensor measured the reaction of the surface rather than deformation in the structure, indicating that further preload did not push more air from the disc (Fig. 5.2f).

From these results, we concluded that when using passive suction discs, the fiber-reinforced actuators required over 120 kPa to generate the 2N preload needed to create the

maximum adhesion of the suction discs. The ringed actuators were able to produce sufficient force at less than half the pressure of the fiber-reinforced actuators but did not have a strong correlation between input pressure and change in length. For applications where more precise length control was needed, the fiber-reinforced actuators coupled with active suction discs would be more suitable.

5.3.2 Characterization of adhesion of suction discs with active suction applied

To determine the adhesive force that the suction discs can provide with active suction, we performed pull tests on a universal testing machine (M7-50 force gauge 250 N capacity, 0.05 N resolution; Mark-10, Inc.), applying negative pressure to the suction disc and then pulling it from the surface. We used the universal testing machine to lightly touch the disc against an acrylic substrate without a preload (i.e., not pressed and deformed against the surface) before we applied a negative pressure through the pneumatic tube. The machine then pulled upward on the disc at 25 mm/min and recorded the adhesive force until the disc detached from the surface. Similar to the measurements of the blocked force of the actuators and the adhesion of the passive suction discs, we simulated the effects of the angled actuators by performing pull tests against angled surfaces. A representative trial has been included in Fig. 5.3c.

We found that the suction disc consistently generated lower maximum force on surfaces with higher angles of inclination relative to the pulling force, consistent with our previous work on passive suction discs [210]. The maximum adhesion force generated was around 2.5 N when we pulled the disc perpendicularly to the surface at a high vacuum pressure (Fig. 5.3a). However, at higher applied vacuum pressures on angled surfaces, the maximum adhesion force before detachment decreased. This finding was inconsistent with our initial hypothesis that a higher pressure differential between the internal suction chamber and the ambient pressure would produce a greater peak force. We believe that this is because the higher applied vacuum pressure produced greater stresses on the disc, reducing the quality of the seal with the surface

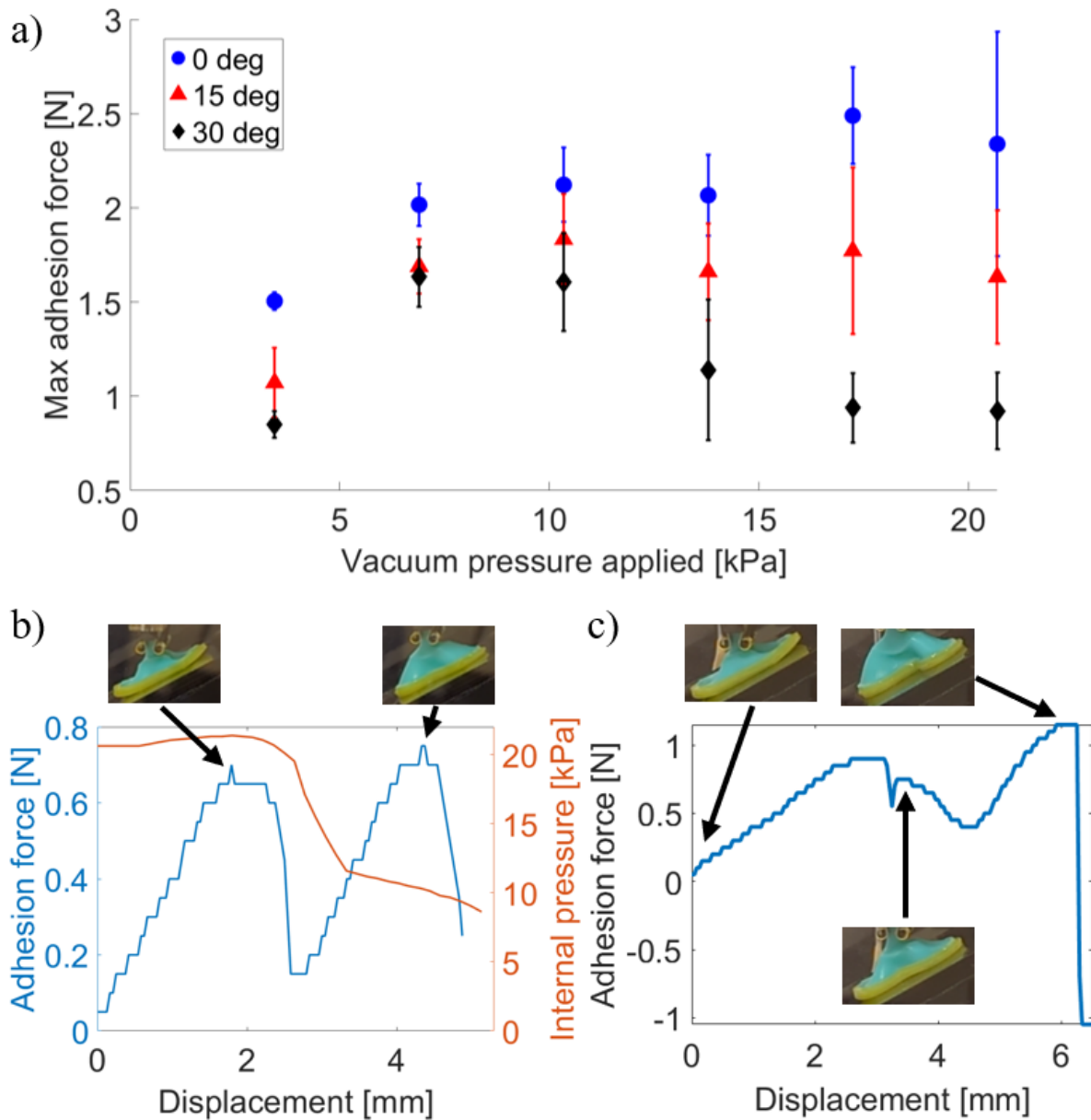


Figure 5.3. Characterization of the adhesion of the active suction discs. a) Relationship between the active vacuum pressure generated in the disc, and the corresponding maximum adhesion force when the discs were pulled at different angles relative to a flat surface. Error bars indicate the standard deviation of the N=9 data. b) Representative trial of adhesion force vs. displacement for a disc being pulled at an angle of 30° relative to a flat surface in the constant-mass case where an active vacuum was generated, and then the vacuum line was sealed. c) Representative trial of adhesion force vs. displacement for a disc being pulled at an angle of 30° relative to a flat surface in the case where an active vacuum was applied throughout the test. The images in b) and c) are of the disc at the indicated displacements in the experiments, illustrating the deformation of the disc while being pulled from the surface.

and increasing the likelihood of air leaking into the suction chamber.

As we pulled the disc upward, the suction chamber increased in volume as 1) the chamber flipped from being mostly flat to concave down and 2) the disc margin flipped from being flared upward along the edges to flush with the surface. To further investigate this behavior, we performed a set pull-tests where we closed a valve in the suction line after we applied a negative pressure inside the disc so that it became a closed-mass system. We pulled the disc upward at a constant rate of 25 mm/min while monitoring the pressure inside of the suction disc and found that while the pressure initially increased by 3.3% as we pulled the disc upward, the pressure quickly dropped to about half the initial applied pressure before the disc detached from the surface (Fig. 5.3b). This finding was consistent with our hypothesis that during the pull test, air leaked through the seal into the suction chamber. If no additional mass entered the suction chamber, as the internal volume increased, the internal pressure would be proportional to the volume change.

Finally, we performed additional pull tests of a single disc on flat surfaces of varying roughnesses to determine how active suction would scale. The smooth surface was a plate of acrylic and the rough surfaces of 68 μm and 269 μm were sandpaper (P220, 3M, Inc. and P60, 3M, Inc. respectively) bonded to acrylic plates. The suction disc exhibited high adhesion force to the smooth surface and some adhesion to the surface with small roughness, though less than the adhesion to the smooth surface (Fig. 5.4). In addition, the adhesion force increased as the applied vacuum pressure increased but dipped at the highest vacuum pressure tested. This non-monotonic behavior was similar to the behavior on smooth surfaces. The suction disc exhibited almost zero adhesion to the roughest surface, indicating that the disc was unable to create a seal with the surface.

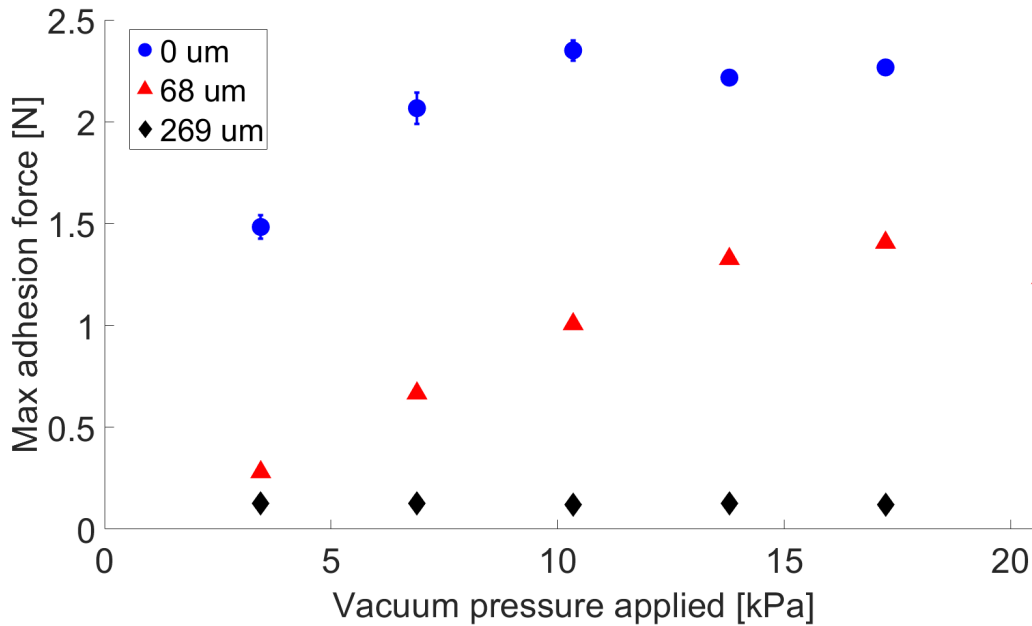


Figure 5.4. Characterization of the adhesion of an active suction discs to a rough surface. a) Relationship between the active vacuum pressure applied to the disc and the corresponding maximum adhesion force when a disc was pulled from flat surfaces of different roughnesses. Error bars indicate the standard deviation of the N=3 data.

5.4 Applications for a Walking Robot

To test the performance of the tube foot modules for locomotion, we attached four of the ringed actuator modules spaced 30 mm apart to a rigid body at a fixed angle of 30 degrees with respect to the body. To create forward locomotion, we mounted the body of the robot to a linear slider with Delrin surfaces (for reduced friction) that moved along an extruded aluminum rail 115 mm above an acrylic surface. The linear slider prevented pitching and rolling of the body so that we could investigate the performance of the actuators in one plane (Fig. 5.5).

We also used a pulley with a 110 g mass to provide a small forward force to compensate for the friction in the slider and the initial stiffness of the pneumatic tubing tether (the stiffness of which increased with displacement, so this compensation was conservative). The pneumatic lines were actuated using pumps and 3/2 solenoid valves controlled by a microcontroller (Arduino Mega) offboard the robot. The pneumatic lines providing positive pressure to the soft actuators

were routed from a pump (D2028B 12V, AIRPO) through a set of four solenoid valves on a manifold while a second pump provided negative pressure to the suction discs through a separate set of valves on a different manifold.

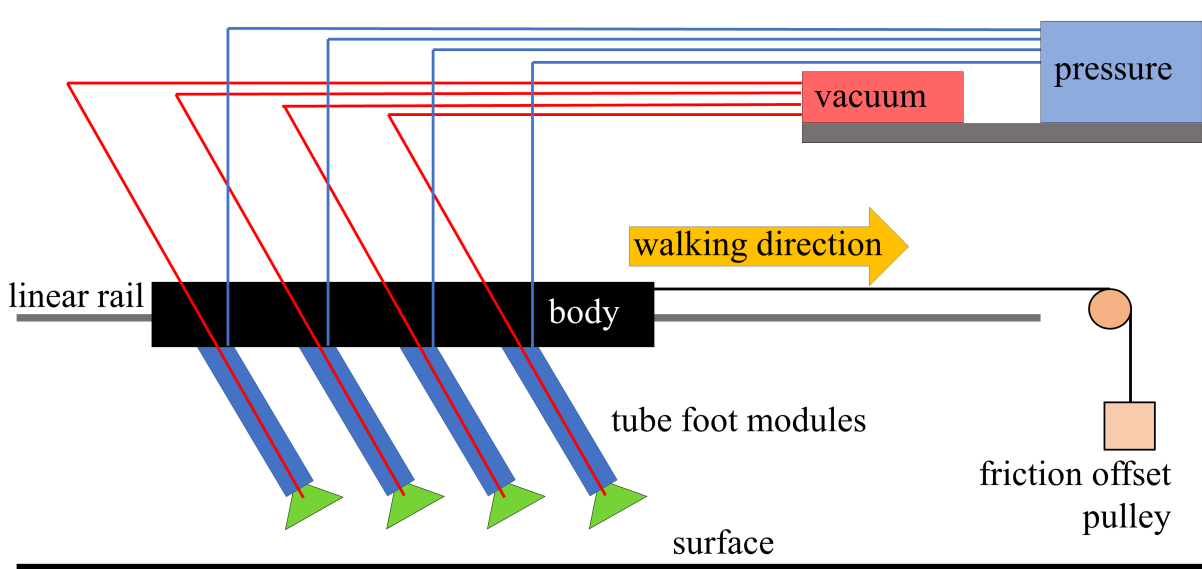


Figure 5.5. Experimental setup for the walking robot. Schematic of the walking system depicting the body of the robot, rails, counterweights, and the pneumatic routing.

The robot used a traveling wave gait where one actuator module was activated at a time in sequence from the rear to the front (see Fig. 5.6a-e). We first inflated the extension actuator and activated the suction line to the disc simultaneously. The tube foot actuator inflated for a constant period of 1 s and pushed the disc toward the surface, where the rear of the suction disc initiated contact. Further inflation of the tube foot actuator caused the disc to rotate at the ankle with respect to the actuator until the disc was flush with the surface. The actuator then deflated and contracted for a constant period of 0.5 s. If the disc was adhered to the surface, the elastic restoring force of the actuator was reacted by the adhesion, resulting in a forward force applied to the body as the actuator contracted.

We also demonstrated that the robot could pull an effective maximum payload of 160 g (Fig. 5.6f). To do this, we removed the 110 g counterweight that was used to offset the friction and the pneumatic tether and added a 50 g counterweight in the opposite direction. As expected,

higher payloads caused the robot to move slower.

We then added feedback control by connecting digital pressure sensors along the negative pressure lines to the suction discs. During the walking sequence, once a disc was sealed against the surface, the pressure sensor on the active suction line read an increase in the negative pressure. If the sensor triggered or if the actuator extended for a prescribed time period (1 s) without the disc achieving a seal, the tube foot then initiated a 0.5 s long contraction period where the air inside the tube foot was vented to atmosphere and the pressure inside the actuator returned to ambient.

Finally, we demonstrated that the compliance of the soft actuators combined with the redundancy of the array of actuators was useful for obstacle traversal. The robot was able to successfully traverse an acrylic step 6.35 mm in height and 70 mm wide (Supplementary Video S1) as well as over a small ramp at a 6.6 degree angle ending at a 9.5 mm high point (Fig. 5.7a). The 9.5 mm obstacle combined with the fixed height of the rail acted as a constrained space, simulating the case of the robot walking through a narrow passageway. At certain points, the friction between the disc margins and the acrylic surface prevented some tube foot modules from slipping against the surface as other actuators pulled the body forward. But because of the compliance in the soft actuators, the tube foot modules were able to deform and squeeze between the constraints, eventually emerging through the passage.

Obstacles above the nominal surface like steps or the ramp also illustrate the advantages of sensing pressure in the suction disc. Because the obstacles were taller than the nominal surface, the discs encountered them earlier in the extension period. Without sensing, the tube foot actuators would continue to be pressurized at constant intervals regardless of the surface contact. Since the closed-loop case reduced these cases of overpressurization, the robot was able to more quickly cycle through the actuation of the tube feet. The maximum period of actuation for each tube foot module was 1.5 s and in the demonstration of squeezing through a confined space, only 16% of steps required the full actuation period. Additionally, the gait with sensor feedback performed the same number of steps as in the open loop case in only 71% of the time

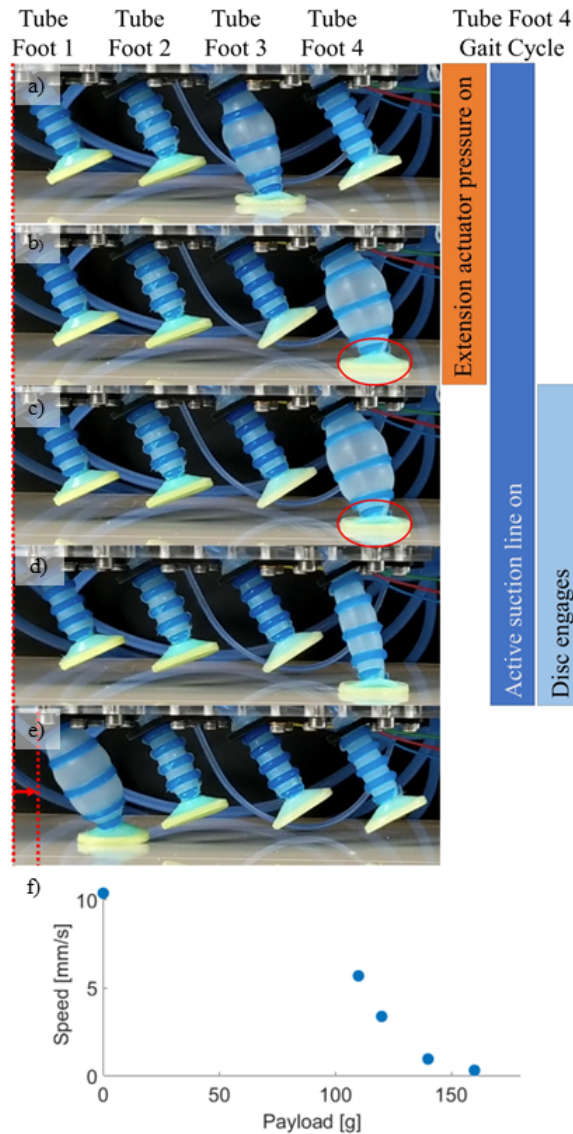


Figure 5.6. Characterization of the walking behavior of the robot with a simple traveling wave gait. a-e) One cycle of the actuation of Tube Foot 4. a) As the previous actuator in the sequence was retracting, Tube Foot 4 extended and vacuum pressure was applied to the disc. b) The suction disc contacted the surface with active vacuum applied. c) Once the circumference of the disc was fully in contact with the surface, its seal was formed. d) If the disc successfully adhered to the surface, the actuator contracted and the elastic restoring force in the actuator pulled the body of the robot and the other tube feet forward. e) Once the actuator was fully contracted, the next tube foot in the sequence began extending. f) Speed of the robot pulling different payloads.

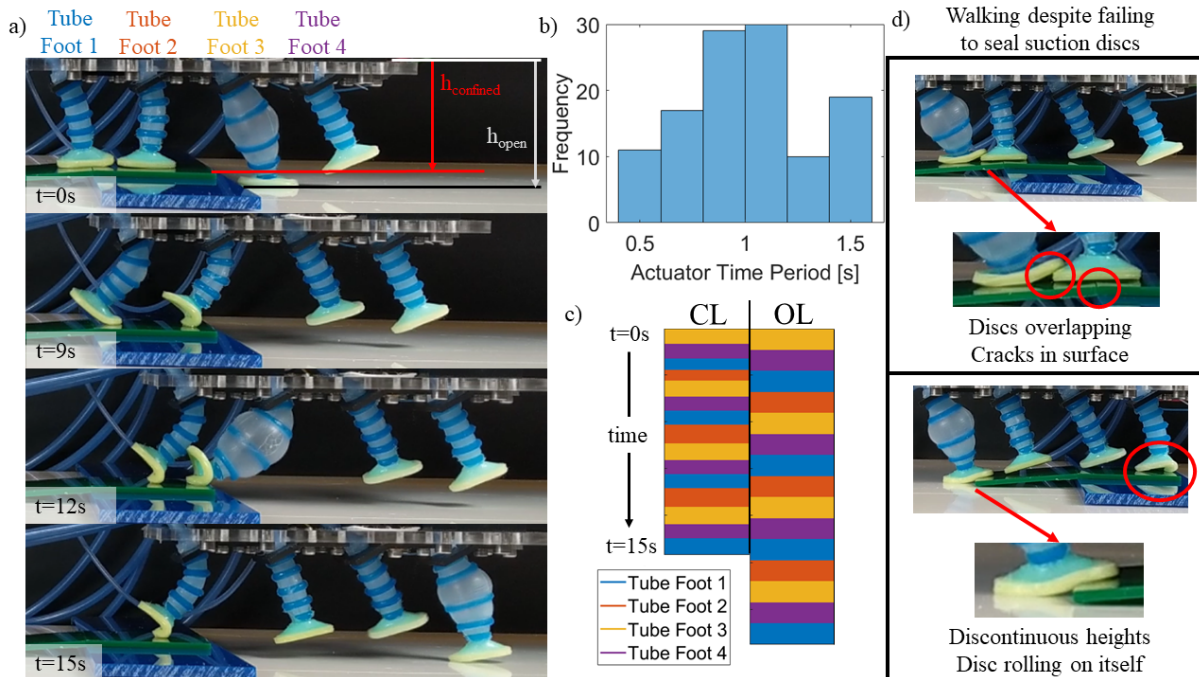


Figure 5.7. Demonstration of the locomoting robot walking through a confined space between a rail above it and an acrylic surface below it. The robot received feedback about the status of adhesion from a pressure sensor connected to the inside of the suction discs. a) The robot was able to traverse through a passageway. The softness of the tube feet resulted in passive bending to squeeze through the opening. b) Histogram describing the distribution of time periods during which each tube foot actuator was active. Without pressure feedback, each tube foot would be active for the maximum time period (1 s pressurization and 0.5 s deflation); with pressure feedback, the actuator was only active for the maximum time period if it was unable to create a seal. c) Comparison of the closed-loop (CL) gait compared to an open-loop (OL) gait. The closed-loop gait performed the same number of steps as the open-loop gait in 71% of the time. d) Examples of situations from this trial where the suction disc could not seal against the surface, such as a thin but long crack, the edge of a step, or when stepping on another suction disc. For all four faults pictured, the robot continued moving because the other actuators were able to compensate.

(Fig 5.7b-c).

Our results also highlight the advantage of an array of low-dimensional actuators. Even when one or more suction discs were unable to form a seal with the edges of the obstacle (Fig. 5.7c), other actuators were able to make contact with nearby surfaces. The unaffected actuators continued the forward motion of the robot until the frustrated actuators were cleared. We hypothesize that this resistance to failure could also compensate for damage in extension actuators or suction discs, noise in the pressure measurements, or other failures related to individual tube feet.

5.5 Conclusions and Future Work

In this work, we have presented soft appendages capable of using adhesion to generate locomotion over flat ground and small obstacles. We have characterized two types of soft extension actuators: a ringed actuator that was able to produce higher forces but was not suitable for length control and a fiber-reinforced actuator that had a strong pressure-to-length correlation but could not produce high forces. We also characterized the soft active suction discs and described their performance when pulled at angles likely to be encountered during locomotion. The use of active suction discs for adhesion created similar performance to the use of passive suction discs without requiring high preload forces, allowing the use of soft materials that were compliant and adaptable for use in variable and constrained environments. We also demonstrated that a robot consisting of several of these actuators uses redundancy to mitigate the effect of individual failures and could traverse small obstacles even when some actuators were unable to seal against the surface. In addition, the softness of the actuators allowed the robot to squeeze through confined spaces without additional actuated degrees of freedom.

Future work could investigate the generalization of this locomotion system to other obstacles and terrains. Further study of potential gaits for the tube foot modules could help in removing the robot from the experimental simplification of the slider setup. The array of

actuators could be expanded to larger quantities by adding more complex pneumatic hardware, which provides the opportunity to create more unique coordination schemes for the tube foot modules. In addition, having valves connected to the same manifold precluded the robot from simultaneously sensing the pressure in multiple suction discs. Isolating these suction lines could help achieve more sophisticated coordination between tube foot modules.

In summary, the coupling of adhesive elements with soft actuators has the potential to create highly versatile robots capable of traversing variable terrain including vertical and inverted surfaces, even when subjected to disturbance forces such as those of ambient flow underwater. Large arrays of these modules may provide robustness of the overall robot to damage and may reduce the path planning and control complexity by allowing built-in tolerance to the faults of individual modules. We anticipate that the envisioned star fish inspired robots will be well-suited for the exploration of underwater environments in flow or for the inspection and monitoring of hard-to-reach locations such as the undersides of ships in motion.

Chapter 5, in full, is a reprint of the material as it appears in: Ishida M., Sandoval J. A., Lee S., Huen S., Tolley M. T. (2022) "Locomotion via active suction in a sea star-inspired soft robot", *IEEE Robotics and Automation Letters/IROS*, 7 (4), 10304-10311. The dissertation author was the primary investigator and author of this paper.

Chapter 6

Vectored thrust of a cephalopod-inspired jetting robot with a soft nozzle

6.1 Introduction

Existing underwater robots are good at moving through open space quickly, but they often use propulsive mechanisms like propellers that are noisy and disruptive to the local environment [188]. These characteristics make it difficult for these existing robots to perform observation tasks of animals or to interact with easily damaged objects and organisms [211, 186]. To mitigate these negative effects on the robots' surroundings, researchers have taken inspiration from biology to create robots that operate with more natural motions [197, 196].

The squid swims using a combination of jet propulsion and the motion of its fins. At low swimming speeds, the squid uses its fins to create both forward motion and upward lift with an undulation motion [212]. At high speeds, the squid can wrap its fins against its body to reduce the drag opposing its swimming motion [213]. In this state, with the fins unable to contribute to lift opposing its net negative buoyancy, the jet must compensate by creating upward thrust, leading to a "climb-and-glide" swimming trajectory [214].

The efficiency of squid-inspired jet propulsion is difficult to assess. The jet itself is more efficient at higher swimming speeds because the slip (difference between jet speed and swimmer speed) decreases as the swimming speed increases [215]. However, the deceleration caused by the refilling of the mantle plays a significant role in the low efficiency of the jet cycle as a

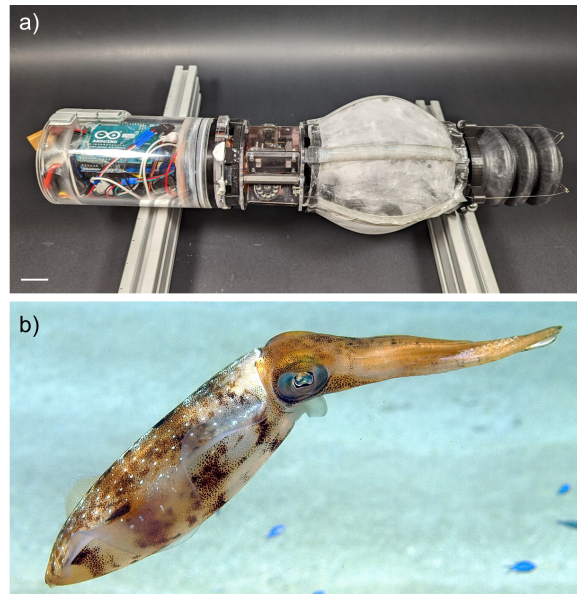


Figure 6.1. Experimental prototype and biological inspiration for a jet-propelled swimmer. a) Our cephalopod-inspired swimming robot with a soft nozzle for creating vectored thrust b) A squid swimming through open water.

whole at high speeds [216]. Previous work has shown that there is an optimal ratio between the diameter of the nozzle and the volume of fluid expelled in the jet, which creates an efficient vortex pattern [217]. While this has been shown in squid [218], other measures of whole-cycle efficiency shows that the squid may need to increase aperture diameter of the nozzle to increase velocity or to alleviate stress in its muscle [219].

While the squid is not the most efficient of the underwater swimming animals, its jet propulsion locomotion has several advantages. The squid is the fastest swimming marine invertebrate [220] and its maximum peak speed [221] is similar to that of the fastest fish. It also has the smallest turning radius normalized to body length of any marine animal [222]. In addition, jet propulsion can be simpler to adapt into a swimming robot rather than the much more complex locomotion of body undulation or paddling using fins.

Since many animals that use jet propulsion to swim are soft invertebrates with highly deformable bodies, underwater jetting robots often fall under the category of soft robotics [223]. A common design of soft jetting robots is to use a smooth elastic shell as a soft water-containing

cavity that can be quickly deformed to force a jet of water out [224]. Other previous research on soft swimming robots using pulsed-jet propulsion have explored different aspects of the jetting process. Changing the ratio of the diameter of the nozzle to the length of the jet of water expelled from the robot can improve the propulsion of the robot [225]. Alternatively, operating a robot at the natural frequency of the flexible cavity can increase the robot's speed and efficiency, although this frequency is much higher than the jetting frequency exhibited by animals [226]. Another approach to creating a shape-changing body is to use origami techniques to create small folds in a sheet, forming a 3D cavity. These folds can transition the structure from a high-volume state to a low-volume state to create a jetting action [227]. Other jetting robots with soft structures include a deployable structure based on a Hoberman sphere covered by an elastic membrane [228] and a rigid cavity containing an elastic sac that rapidly expands due to the combustion of a gas, quickly pushing fluid out of the rigid cavity to create a jet [229]. Furthermore, there are other soft robots inspired by jellyfish [230, 231, 232], though the motion of a jellyfish is also dependent on the kinematics of the velum that interacts with the fluid [233].

The majority of these approaches demonstrate locomotive ability only and leave questions of steering the robot to future work. The trajectory of the robot can be controlled by angling the jet aperture with respect to the centerline of the robot, creating vectored thrust that turns the robot, but this work does not demonstrate the use of a deformable nozzle or active changing of the trajectory during swimming [234]. Other works have demonstrated the use of soft materials and soft actuators for both directing the nozzle and changing the aperture of the nozzle without demonstrating the mechanism on a swimming robot [235]. The vectored thrust capability of a soft, pulsed jet swimmer has been explored in simulation [236].

In this work, we present a jet-propelled swimming robot inspired by cephalopods with a soft actuated nozzle that bends to direct flow out of the robot. We show that the nozzle takes little force to actuate because of the bellows structure and that the bellows geometry has only a minor effect on the flow through it. We also explore the design space of the drivetrain mechanism to alter the time varying properties related to compression and release of the body. Finally, we

demonstrate the steering mechanism and the drivetrain on a physical swimming robot.

In Section 6.2, we describe the design of the actuated soft nozzle and the cam and follower mechanism used in the drivetrain. In Section 6.3, we characterize the properties of these subsystems and their effects on the operation of the robot. Finally, we present our conclusions and future work for further development of a shape-changing, steerable jet-propelled swimming robot in 6.4.

6.2 Robot Design and Fabrication

The cephalopod-inspired robot consists of four main elements: an elastic skin that forms the cavity containing water to create the jet, a mechanism that deforms the soft body for intake of fluid and jetting of fluid, an actuated soft nozzle that directs the jet, and a waterproof enclosure for the electronics. Similar to our previous work [225], the elastic skin is made from a clear, stretchable tape (3M, VHB 4905) reinforced with six flexible but inextensible strips of fiberglass 0.015 in in thickness spaced equidistantly around the axis of the robot.

6.2.1 Actuated Flexible Nozzle

We fabricated the soft nozzle from a commercially available rubber bellows (McMaster-Carr, 5298K29) with an inner diameter of 2 in. The bellows are radially symmetric, which allows the nozzle to bend in any direction with similar bending stiffness. Our previous work [225] has shown that the robot can pivot in place with a nozzle angle of 34 degrees with respect to the robot's axis. We measured the minimum number of bellows segments necessary to achieve the desired 34 degree bend angle and that determined the length of the soft nozzle (74 mm) and the other nozzles used for comparison.

The ventral end of the nozzle was rigidly attached to the rigid framing of the body of the squid. Three tendons are attached to the distal end of the nozzle, spaced radially equidistant from each other and are routed through tubes adhered to the reinforcing ribs along the body. Since the ribs are flexible but inextensible, using this method for routing the tendons ensured that the

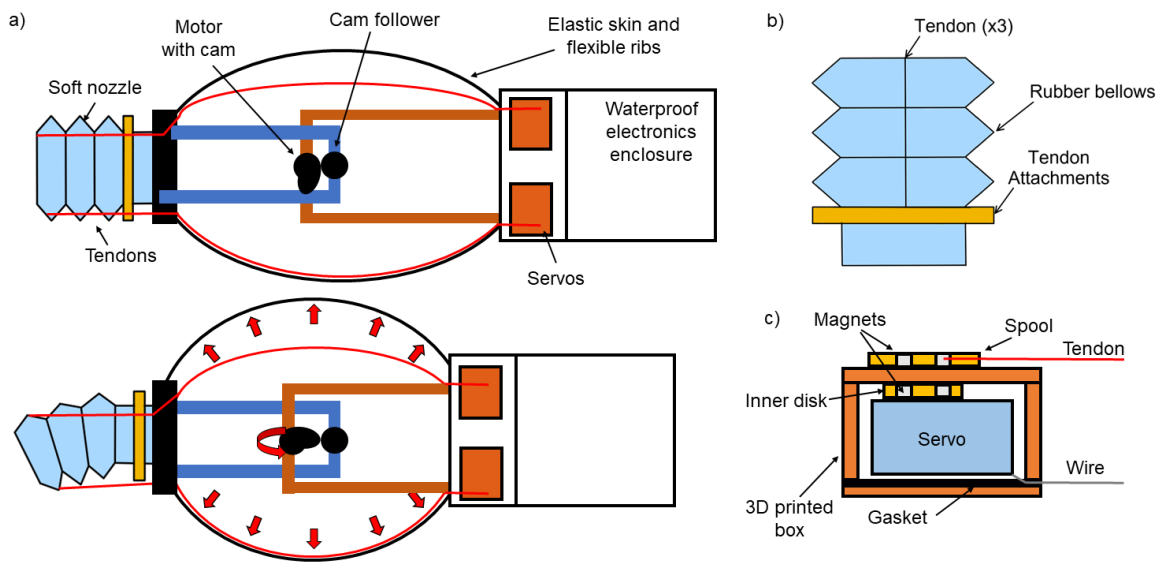


Figure 6.2. Schematic of the robot, soft nozzle, and waterproof motor enclosures. a) The robot consisted of a soft body made of an elastic skin with six flexible ribs compressed by a cam and follower mechanism. It has a soft nozzle made of a neoprene rubber bellows actuated by tendons. The tendons were routed through the body along the flexible ribs to servos and a waterproof enclosure on the other side of the body. b) The tendons were spaced at 120 degree intervals around the circumference of the rubber bellows and routed through a rigid tendon attachment at the base of the bellows. c) Each servo was enclosed in a 3D printed waterproof box. Rotation of the servo inside the box was coupled to rotation outside of the box through discs with magnets.

tendon did not become slack when the body compresses during the refill period.

The tendons were actuated using miniature servos (RGBZONE, ES08MA II) chosen for their small size to fit within the existing radial footprint of the robot. To use these servos in the fully submerged environment, we created waterproof housings for each of the servos. We 3D printed the housings out of a solid photopolymer resin (Stratasys, VeroClear) and sealed using a neoprene rubber gasket and a waterproof adhesive.

To transmit rotation from the servo inside the sealed watertight housing to a mechanism in the flooded environment, we used a magnetic coupling through the thin wall of the housing. We connected a plastic disc with twelve embedded neodymium magnets (K&J Magnetics) each 1/8 in in diameter to the output shaft of the servo inside the housing. A similar disc with magnets was attached on the outside of the housing. We arranged the magnets with alternating polarity along the circumference of the disc. A small amount of rotation by the disc attached to the motor output drives the magnets away from alignment; the repelling magnetic forces then rotate the disc on the outside of the box.

6.2.2 Drivetrain

To produce the jet of water for locomotion, the squid robot increased the volume of its body, creating a pressure gradient that pulled water into the body. The robot had a DC motor that actuates a nautilus cam and follower mechanism to pull the two ends of the body toward each other, buckling the elastic skin and reinforcement strips. This made the body more spherical, increasing the internal volume. Then, when the rotation of the nautilus cam reached the flat region of the cam, the body rapidly returned to its initial, elongated shape via the elastic restoring force of the skin and reinforcement strips. This sudden change in volume expelled water in a jet out of the nozzle, creating thrust for swimming.

The use of a cam for creating the linear actuation enabled a nonlinear relationship between the angular position of the motor shaft and the length of the body, which was directly related to the internal volume of the robot as defined by the diameter of the cam. We used this to define the

ratio of time spent coasting (i.e., no change in the length or volume of the robot) and refilling (i.e., increasing the volume of the robot), which greatly affected the robot's swimming performance. The robot was in a low drag configuration (low frontal area) when it was coasting and in a high drag configuration (high frontal area) when it was refilling its body, so it was advantageous to increase the coasting period relative to the refilling period. However, the minimum length of the refilling period was determined by the maximum power of the drivetrain motor that compresses the elastic elements.

6.3 Experimental Results and Discussion

6.3.1 Characterization of the Nozzle

We measured the force required to bend the soft nozzle to different angles to determine the stiffness of the nozzle using a universal testing machine (Mark-10). We rigidly attached the soft nozzle to a test frame in the horizontal frame to reduce the effects of gravity on its actuation. We then routed the tendon for actuation around a pulley and connected it to the universal testing machine. The machine pulled the tendon upward at 20 mm/min and measured the force on the tendon while a camera tracked the angle of the nozzle.

We found that it takes 0.19 N to actuate the nozzle to the expected maximum angle (34 degree angle with respect to the robot's axis). The relationship between force applied and angle of the nozzle was roughly linear through most of the range of achievable angles, but sharply increased toward the maximum 34 degree angle.

We also characterized the losses through the nozzle as a function of flow rate to compare the efficiency of the flow through the soft nozzle with flow through other designs with smooth interiors. The soft nozzle had a bellows structure that allows it to bend continuously under relatively low force, but this meant that the inner surface of the nozzle was not smooth, which could potentially create disadvantageous interactions with flow exiting the nozzle.

To find the flow rate through the nozzle, we released 0.75 L of water through the nozzle

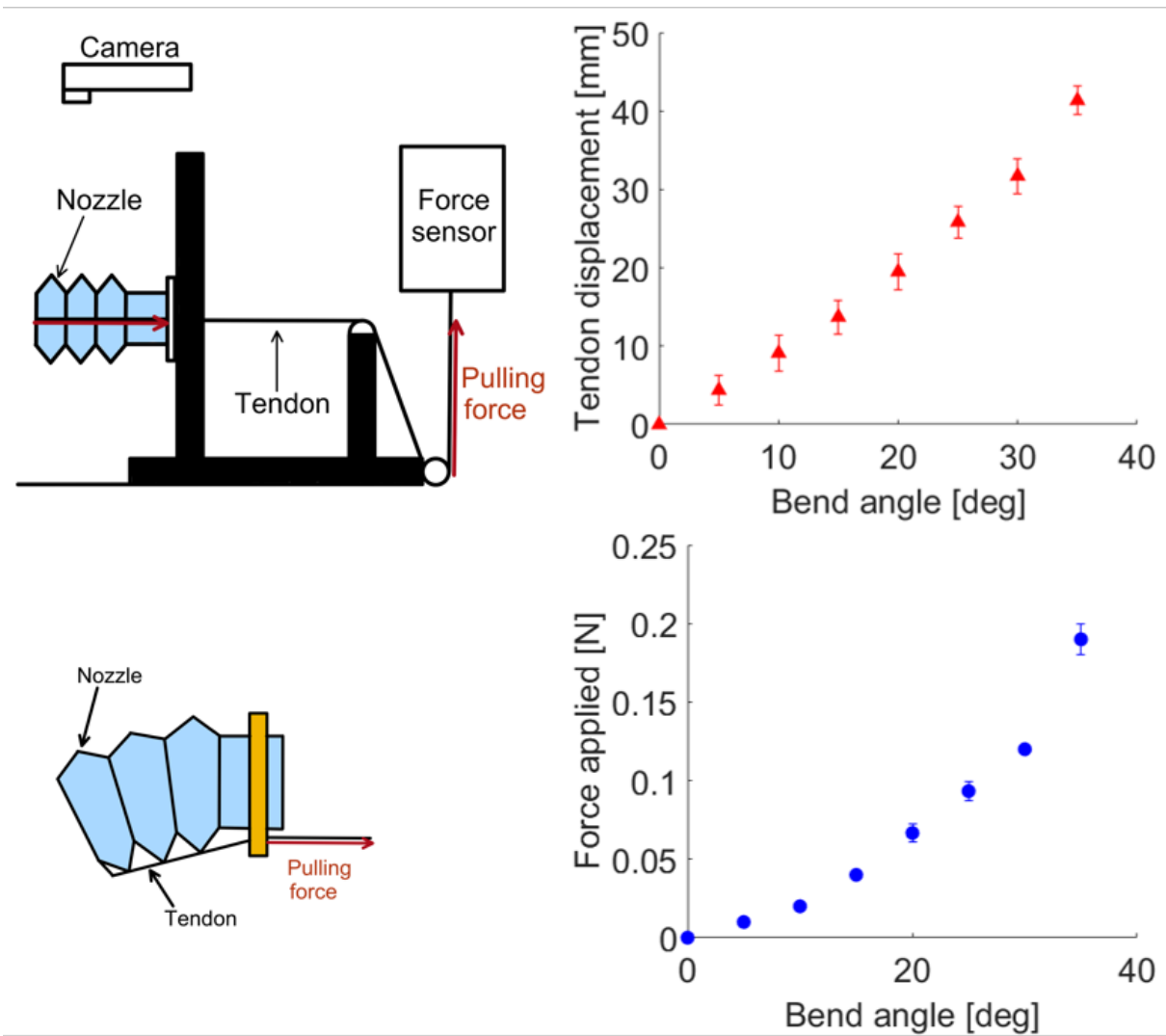


Figure 6.3. Characterization of the bending of the nozzle. a) Experimental setup to measure the bending using a universal tensile testing machine. b) Force necessary to bend the nozzle to given angles. c) Displacement of the tendon necessary to bend the nozzle to given angles.

and measured the time it took for all the water to flow out. We compared the performance of the soft nozzle to the performance of rigid nozzle designs printed out of PLA with the nozzles in line with the body of the robot (i.e., 0 degree angle with respect to the robot's axis) and with the expected maximum nozzle angle (34 degree angle with respect to the robot's axis). We tested a generic controllable nozzle with a rigid piece that rotates with respect to a ball joint and a pair of structures that were static at 0 degree and 34 degree angles.

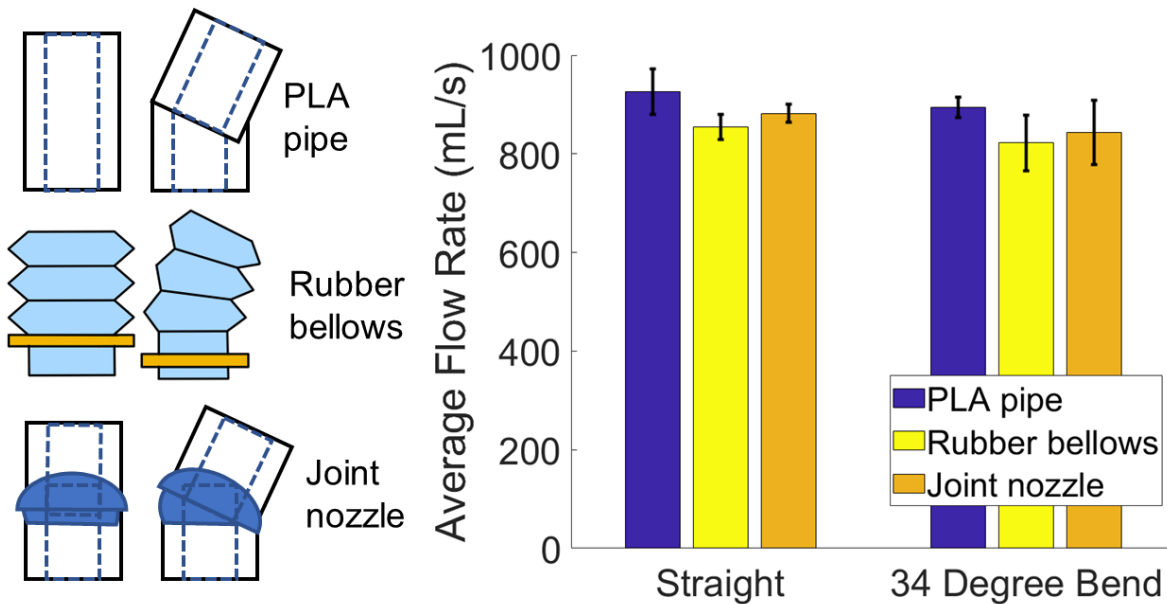


Figure 6.4. Quantification of losses in flow through the soft nozzle and other designs. a) Schematics of the three different nozzle designs we tested to compare both the losses from geometries and from materials. b) Comparison of flow rate through the different nozzle geometries in a straight orientation and at the maximum bend angle.

We noticed a reduced flow rate through the soft bellows nozzle compared to the static nozzles. We also saw that the flow rate through the soft bellows was lower than the flow rate through the rigid nozzle with the ball joint in the straight configuration. However, when oriented in the 34 degree configuration, the flow rate through the nozzle with the ball joint was similar to the flow rate through the soft nozzle. The internal diameter of the rigid nozzle decreased when the nozzle rotated because the rotation closed off part of the flow path, whereas the internal

diameter of the soft nozzle remained the same. The losses due to the bellows geometry were on the same order as the losses due to actuating the rigid nozzle.

Finally, we measured the force necessary to create failure in the magnetic drive coupling used in the waterproof servo box. If the force applied to the magnetic coupling was sufficiently high, the disc on the outside would rotate and slip with respect to the disc on the inside of the box. When the disc slipped enough that the magnets inside and outside the box repelled each other, the coupling could no longer transmit rotation between the two discs.

We found that the number of magnets and the placement of the magnets on the disc affected the performance of the magnetic drive coupling. More magnets increased the force necessary to cause failure. In addition, moving the magnets toward the outside of the disc also increased the force necessary for failure because there was a lower radial distance between the magnets and the tendon on the spool. Failure occurred when the discs had slipped enough that the magnets began to repel each other. For the discs with fewer magnets and larger angular spacing, we found that the discs would slip through a larger angle with lower force applied before failure than the discs with more magnets.

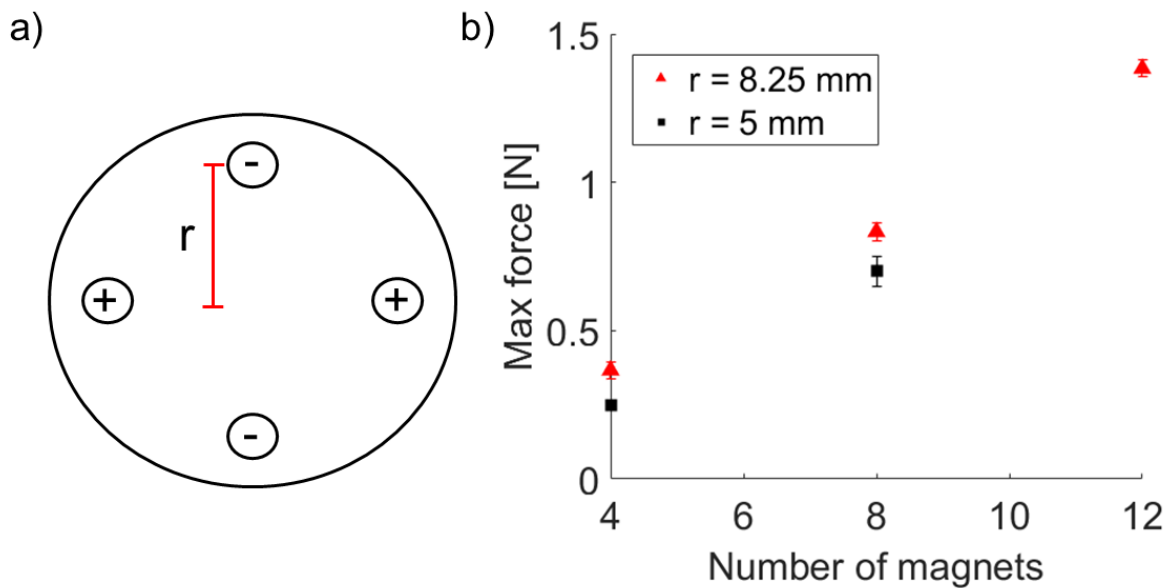


Figure 6.5. Characterization of the magnetic coupling for the waterproof servo enclosures. a) Schematics of the magnet mounts. b) Force necessary to cause failure of the magnetic coupling.

6.3.2 Characterization of the Transmission System

We measured the maximum power draw of the transmission system compressing and releasing the elastic force of the shape-changing mechanism in air. To do this, we recorded the voltage and current draw of the electrical system during 40 s of operation with a frequency of 0.94 Hz and calculated the instantaneous power draw. We performed some low-pass filtering on the signal and took the maximum of the filtered data.

We found that the maximum instantaneous power draw of the motor increased dramatically as the rise displacement decreased (i.e., as we shortened the refill period). This was consistent with the idea that the limit for the minimum refilling period was defined by the maximum power draw achievable of the motor. While the instantaneous power draw appeared to increase when we lengthened the refill period, it was not statistically significant.

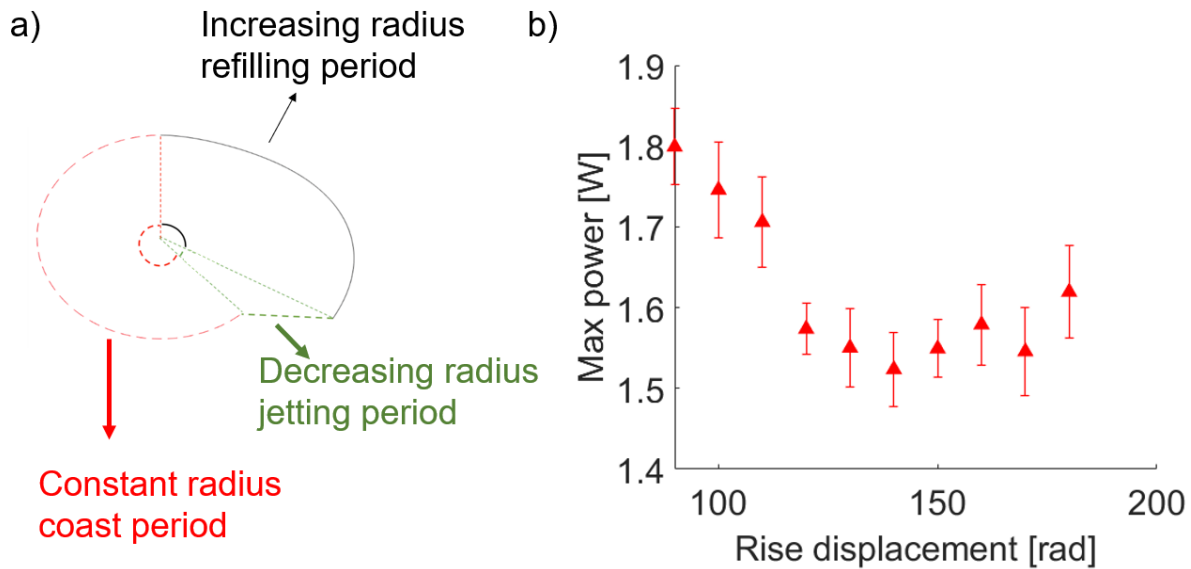


Figure 6.6. Characterization of the cam that drove the compression of the body. a) Schematic describing how the regions of the cam affect different phases of the robot’s motion. The region of constant radius created a coasting motion (i.e., forward momentum but no thrust), the region of increasing radius filled the with water, and the region of decreasing radius expelled the water. b) Maximum instantaneous power draw from the motor attached to the cam for different refilling periods.

6.3.3 Mechanisms Incorporated on a Robot

Finally, we combined the mechanisms together into one robotic system. We showed that we could actuate the cam system driving the compression of the body independently from the steering system and that the nozzle could actuate in all directions.

6.4 Conclusions and Future Work

In this work, we have presented a cephalopod-inspired robot capable of steering using a soft nozzle that can be angled to produce vectored thrust. The bellows used for the nozzle have a low structural bending stiffness and the losses in flow efficiency due to the bellows geometry are on par with that of other designs. We also developed a cam and follower for the drivetrain of the robot and showed that the geometry of the cam affects the efficiency of the robot. Finally, we showed an example of these mechanisms combined in a full robot.

Future work could investigate other ways to improve control of the swimming motion. Because the robot can only change its heading during each pulse and not during the coast or refill periods, future work could explore more complex control algorithms for path planning of a pulsed jet robot. Adjusting other variables in the design of the cam such as creating a nonlinear displacement profile could further reduce the maximum power drawn from the motor. In addition, more optimization of the stiffness of the robot or the frequency of the pulses could create more efficient locomotion. Creating a steerable jet propelled swimming robot has the potential to improve highly maneuverable robots for exploring a variety of underwater environments.

Chapter 6, in part, is currently being prepared for submission for publication of the material: Ishida M., Wood J., Gaggar A., Tolley, Michael T. "Vectored thrust of a cephalopod-inspired jetting robot with a soft nozzle". The dissertation author was the primary investigator and author of this paper.

Chapter 7

Conclusions

This dissertation has explored aspects of soft robotics unique to operation in underwater environments. Fluid forces affect the operation of robots more significantly in underwater environments than in land-based environments because the greater density of water over air significantly affects the drag force (opposes the motion of the robot), the lift force, and the buoyancy force (affects the traction of a walking robot).

Examining previous work shows that soft materials can support complex motions that closely mimic the crawling or swimming behaviors of underwater animals and create continuous curvatures well-suited for interactions with underwater flow. These soft actuators may be actuated with tendons, fluid pressure, heat, or high voltage, producing various levels of power and efficiency. Although friction-based crawling is a common approach to underwater robots, this method of locomotion is greatly influenced by fluid forces such as lift and buoyancy, requiring these crawlers to adjust shape or posture for optimal performance. Limited work on distributed adhesion-based crawling has been completed to-date and we consider this a promising area of research that has the potential to create significantly more robust robots. In the swimming domain, we see that jellyfish jetting produces the highest efficiency and slowest velocity, whereas squid jetting produces the highest velocity albeit with lower efficiency. These variations of jet propulsion leverage the elastic restoring force of the soft structures more than drag-based swimming or vortex shedding swimming and we think that working to refine the

trade-off between efficiency and speed using soft materials is another promising avenue for future development.

Chapter 3 presented an underwater walking robot with a soft structure that helps mitigate unfavorable interactions with flow. This work showed that even a simple inflatable structure added to the top of a soft walking robot could significantly improve its performance in flow. The inflated morphing structure could increase the downward lift by 50% while only marginally increasing its drag. When paired with a sensing element to detect the direction or strength of the flow, the robot can react to flow conditions and transition to the more effective body shape. Having shape-changing elements that can create large changes to the hydrodynamic profile of a robot can be beneficial in real-world applications involving variable flow environments.

Chapter 4 investigated a method for creating directional, reversible adhesion that can enable locomotion of an underwater walking robot. We demonstrated that a soft, asymmetric suction disc can create adhesion that is dependent on the direction of the applied load. The exact behavior of the discs is dependent on a number of factors, such as geometry, material stiffness, and contact pressure between the disc and the surface. We demonstrated this embedded intelligence by attaching the suction discs to rigid linear actuators that achieved a pulling locomotion via adhesion with automatic detachment from the surface at certain angles of load. By programming the attachment and detachment behaviors of the disc into its morphology, we could eliminate some of the actuated degrees of freedom in a mechanism for adhesion-based walking.

Chapter 5 demonstrated the integration of soft suction discs with soft actuators in an array of modules inspired by the tube feet of sea stars to create a walking motion. We demonstrated that including an active suction line in these modules enables the use of softer actuators by eliminating the need to apply a significant preload force to the disc to engage adhesion. The use of soft materials in the tube foot actuators then enables the robot to squeeze through constrained environments. We demonstrated that a robot consisting of an array of tube foot modules can traverse certain classes of obstacles because the redundancy of the array could compensate for

the failures of individual actuators. Furthermore, the robot could sense the vacuum pressure inside the suction discs and use that feedback as a proxy for whether or not each disc was adhered to the surface, creating a more efficient walking motion. These considerations are important for a robot that uses adhesion to create locomotion to ensure that the behavior can degrade gracefully and that a small failure of a single adhesive element does not create a catastrophic failure of the entire system.

Chapter 6 explored the creation of vectored thrust for a jet-propelled, shape-changing swimming robot. We designed a soft nozzle with a bellows shape actuated by tendons that can direct the jet flow of the robot. The bellows shape reduces the force necessary to bend the nozzle compared to a straight tube and we showed that the losses through the bellows geometry are on the same order as other previous actuated nozzle designs. We also developed a cam mechanism for actuating the shape change of the body to mechanically program different ratios between coasting, refilling, and jetting periods. Finally, we demonstrated the independent operation of these mechanisms integrated into one robot.

7.1 Future Directions

One promising area of research is to progress toward a greater combination of locomotion efficiency and total velocity. Although even nature displays a trade-off between efficiency and overall velocity, current techniques still generally lag behind their biological counterparts. Since fluid forces are more significant underwater than in air due to the higher density of water, soft actuators that are well-suited for operation in air are not necessarily optimal for operation in water. Soft actuators can take advantage of lift and buoyancy to modify upward forces on the robot and to reduce the effective weight. In addition, rather than incrementally improving and optimizing existing soft actuators, new soft actuators can be developed specifically for the underwater environment to create advantageous interactions with the surrounding fluid.

One advantage of soft and bioinspired designs are their capabilities for multifunctionality.

Animals are able to use their body features for multiple purposes (e.g., the sea star using its tube feet both for locomotion as well as for prying open shells to eat) or to combine multiple body features for a single purpose (e.g., the squid using both the fins on its head and its jet siphon to swim). Animals also are optimized for survival, using these same body features to create high instantaneous acceleration for escaping predators while being efficient to conserve metabolic energy. Similarly, soft and bioinspired robots have the potential to be adaptable to many different situations rather than being hyper specialized for specific tasks. While this axis of multifunctionality can be difficult to quantify, versatility is very valuable in a robot facing unknown tasks in a variable environment.

One underexplored area of research for underwater locomotion is using reversible underwater adhesion to drive motion. Adhesion can be used to aid locomotion by creating greater traction with a substrate to apply a propulsive force. While many soft underwater organisms like the octopus and the sea star are capable of suction or chemical adhesion, existing robotics techniques have not been very successful in replicating these aspects of underwater animals. Modern techniques for increasing traction against a surface such as gecko adhesive do not function underwater and carrying and excreting an on-board adhesive and de-adhesive for each foot is not practical for a mobile robot. Commercial suction cups are unsuccessful at adhering to real-life surfaces that are not smooth, so exploring suction geometries used by animals could produce new insights into engineering solutions. Continuing to develop an underwater reversible adhesion method will benefit robots by increasing their locomotion efficiency as well as their ability to manipulate objects.

Along these lines, underwater soft robots that use fluidic actuators can be greatly improved with the development of new valving and fluid control paradigms. Current soft fluidic actuators are generally controlled using a bulky pump or valve for each independently controlled fluid line and it is difficult to scale up the number of actuated degrees of freedom with this constraint. Some approaches to solving this problem include fluidic circuits that autonomously move fluid in predetermined patterns or soft valves that use fluid pressure to open or block other fluid channels,

but there is still room to improve the scaling and adaptability of these systems. This has limited our ability to create and control large arrays of soft actuators in a large robot. For example, we often saw that when the robot was pressing an actuator into the surface to create a seal between the suction disc and the surface, this reaction force would push the robot away from a surface. Having a larger array of soft actuators adhered to the surface would help react that force, which is simply not possible with a smaller array. Overcoming this challenge will be a big step forward to creating more complex soft fluidic robots, such as the arrays of parallel appendages described in this work.

Finally, there are many tradeoffs to be optimized when creating a soft robot inspired by biological systems. For example, robotic mechanisms can not, as of yet, fully replicate the behavior and capabilities of a sea star's tube feet. The biological counterparts exhibit continuum bending in all directions with very simple control and coordination ability of each appendage individually and between the appendages in the array. Each appendage can elongate to a high degree while stiffening to support the mass of the body and react forces from the other tube feet, and the chemical adhesion of each tube foot is much stronger than most engineered reversible adhesion systems. Soft engineered systems can exhibit each of these characteristics, but combining all of them into one system is an open area of research. It is because of these impressive capabilities that we believe soft robots capable of redundant actuation and multifunctionality will be critical for solving challenges in the underwater domain.

Chapter 7, in part, is a reprint of the material as it appears in: Hermes, M.*, Ishida, M.*, Luhar, M., Tolley, M. T. (2020), "Bioinspired Shape-Changing Soft Robots for Underwater Locomotion: Actuation and Optimization for Crawling and Swimming", In Paley, D. A., Wereley, N. M. (Eds.), *Bioinspired Sensing, Actuation, and Control in Underwater Soft Robotic Systems* (pp. 7-39). The dissertation author was the co-primary investigator and co-first author of the sections of the paper that are reprinted in this chapter.

Bibliography

- [1] T. E. Laidig, L. M. Kringsman, and M. M. Yoklavich, “Reactions of fishes to two underwater survey tools, a manned submersible and a remotely operated vehicle,” *Fishery Bulletin*, vol. 111, no. 1, pp. 54–67, 2013.
- [2] G. M. Whitesides, “Soft robotics,” *Angewandte Chemie International Edition*, vol. 57, no. 16, pp. 4258–4273, 2018.
- [3] D. Rus and M. T. Tolley, “Design, fabrication and control of soft robots,” *Nature*, vol. 521, no. 7553, p. 467, 2015.
- [4] J.-Y. Kim and B.-H. Jun, “Design of six-legged walking robot, little crabster for underwater walking and operation,” *Advanced Robotics*, vol. 28, no. 2, pp. 77–89, 2014.
- [5] M. A. Bell, I. Pestovski, W. Scott, K. Kumar, M. K. Jawed, D. A. Paley, C. Majidi, J. C. Weaver, and R. J. Wood, “Echinoderm-inspired tube feet for robust robot locomotion and adhesion,” *IEEE Robotics and Automation Letters*, vol. 3, no. 3, pp. 2222–2228, 2018.
- [6] R. K. Katzschmann, J. DelPreto, R. MacCurdy, and D. Rus, “Exploration of underwater life with an acoustically controlled soft robotic fish,” *Science Robotics*, vol. 3, no. 16, p. eaar3449, 2018.
- [7] C. Christianson, N. N. Goldberg, D. D. Deheyn, S. Cai, and M. T. Tolley, “Translucent soft robots driven by frameless fluid electrode dielectric elastomer actuators,” *Science Robotics*, vol. 3, no. 17, p. eaat1893, 2018.
- [8] R. L. Baines, J. W. Booth, F. E. Fish, and R. Kramer-Bottiglio, “Toward a bio-inspired variable-stiffness morphing limb for amphibious robot locomotion,” in *2019 2nd IEEE International Conference on Soft Robotics (RoboSoft)*, pp. 704–710, IEEE, 2019.
- [9] M. A. Robertson, F. Efremov, and J. Paik, “Roboscallop: A bivalve inspired swimming robot,” *IEEE Robotics and Automation Letters*, vol. 4, no. 2, pp. 2078–2085, 2019.
- [10] F. Gibouin, C. Raufaste, Y. Bouret, and M. Argentina, “Study of the thrust–drag balance with a swimming robotic fish,” *Physics of Fluids*, vol. 30, no. 9, p. 091901, 2018.
- [11] M. Ishida, D. Drotman, B. Shih, M. Hermes, M. Luhar, and M. T. Tolley, “Morphing structure for changing hydrodynamic characteristics of a soft underwater walking robot,” *IEEE Robotics and Automation Letters*, vol. 4, no. 4, pp. 4163–4169, 2019.

- [12] C. Christianson, N. Goldberg, S. Cai, and M. T. Tolley, “Fluid electrodes for submersible robotics based on dielectric elastomer actuators,” in *Electroactive Polymer Actuators and Devices (EAPAD) 2017*, vol. 10163, p. 101631O, International Society for Optics and Photonics, 2017.
- [13] S. Mao, E. Dong, H. Jin, M. Xu, S. Zhang, J. Yang, and K. H. Low, “Gait study and pattern generation of a starfish-like soft robot with flexible rays actuated by smas,” *Journal of Bionic Engineering*, vol. 11, no. 3, pp. 400–411, 2014.
- [14] Q. He, Z. Wang, Y. Wang, A. Minori, M. T. Tolley, and S. Cai, “Electrically controlled liquid crystal elastomer-based soft tubular actuator with multimodal actuation,” *Science Advances*, vol. 5, no. 10, p. eaax5746, 2019.
- [15] M. Calisti, M. Giorelli, G. Levy, B. Mazzolai, B. Hochner, C. Laschi, and P. Dario, “An octopus-bioinspired solution to movement and manipulation for soft robots,” *Bioinspiration & biomimetics*, vol. 6, no. 3, p. 036002, 2011.
- [16] P. Ohta, L. Valle, J. King, K. Low, J. Yi, C. G. Atkeson, and Y.-L. Park, “Design of a lightweight soft robotic arm using pneumatic artificial muscles and inflatable sleeves,” *Soft Robotics*, vol. 5, no. 2, pp. 204–215, 2018.
- [17] H. Jin, E. Dong, G. Alici, S. Mao, X. Min, C. Liu, K. Low, and J. Yang, “A starfish robot based on soft and smart modular structure (sms) actuated by sma wires,” *Bioinspiration & biomimetics*, vol. 11, no. 5, p. 056012, 2016.
- [18] A. A. Stanley, K. Hata, and A. M. Okamura, “Closed-loop shape control of a haptic jamming deformable surface,” in *2016 IEEE International Conference on Robotics and Automation (ICRA)*, pp. 2718–2724, IEEE, 2016.
- [19] P. Polygerinos, N. Correll, S. A. Morin, B. Mosadegh, C. D. Onal, K. Petersen, M. Cianchetti, M. T. Tolley, and R. F. Shepherd, “Soft robotics: Review of fluid-driven intrinsically soft devices; manufacturing, sensing, control, and applications in human-robot interaction,” *Advanced Engineering Materials*, vol. 19, no. 12, p. 1700016, 2017.
- [20] F. Ilievski, A. D. Mazzeo, R. F. Shepherd, X. Chen, and G. M. Whitesides, “Soft robotics for chemists,” *Angewandte Chemie International Edition*, vol. 50, no. 8, pp. 1890–1895, 2011.
- [21] T. Wallin, J. Pikul, and R. Shepherd, “3d printing of soft robotic systems,” *Nature Reviews Materials*, vol. 3, no. 6, p. 84, 2018.
- [22] D. Drotman, S. Jadhav, M. Karimi, P. Dezonias, and M. T. Tolley, “3d printed soft actuators for a legged robot capable of navigating unstructured terrain,” in *2017 IEEE International Conference on Robotics and Automation (ICRA)*, pp. 5532–5538, IEEE, 2017.
- [23] B. Mosadegh, P. Polygerinos, C. Keplinger, S. Wennstedt, R. F. Shepherd, U. Gupta, J. Shim, K. Bertoldi, C. J. Walsh, and G. M. Whitesides, “Pneumatic networks for soft

- robotics that actuate rapidly,” *Advanced functional materials*, vol. 24, no. 15, pp. 2163–2170, 2014.
- [24] F. Connolly, P. Polygerinos, C. J. Walsh, and K. Bertoldi, “Mechanical programming of soft actuators by varying fiber angle,” *Soft Robotics*, vol. 2, no. 1, pp. 26–32, 2015.
- [25] M. A. Robertson, M. Murakami, W. Felt, and J. Paik, “A compact modular soft surface with seconfigurable shape and stiffness,” *IEEE/ASME Transactions on Mechatronics*, vol. 24, no. 1, pp. 16–24, 2018.
- [26] D. Drotman, M. Ishida, S. Jadhav, and M. T. Tolley, “Application-driven design of soft, 3d printed, pneumatic actuators with bellows,” *IEEE/ASME Transactions on Mechatronics*, 2018.
- [27] B. N. Peele, T. J. Wallin, H. Zhao, and R. F. Shepherd, “3d printing antagonistic systems of artificial muscle using projection stereolithography,” *Bioinspiration & biomimetics*, vol. 10, no. 5, p. 055003, 2015.
- [28] R. V. Martinez, J. L. Branch, C. R. Fish, L. Jin, R. F. Shepherd, R. M. Nunes, Z. Suo, and G. M. Whitesides, “Robotic tentacles with three-dimensional mobility based on flexible elastomers,” *Advanced materials*, vol. 25, no. 2, pp. 205–212, 2013.
- [29] R. Niiyama, X. Sun, C. Sung, B. An, D. Rus, and S. Kim, “Pouch motors: Printable soft actuators integrated with computational design,” *Soft Robotics*, vol. 2, no. 2, pp. 59–70, 2015.
- [30] C. Majidi, “Soft-matter engineering for soft robotics,” *Advanced Materials Technologies*, vol. 4, no. 2, p. 1800477, 2019.
- [31] R. Pelrine, R. Kornbluh, and G. Kofod, “High-strain actuator materials based on dielectric elastomers,” *Advanced materials*, vol. 12, no. 16, pp. 1223–1225, 2000.
- [32] S. Hsien Low, L. Lynn Shiau, and G.-K. Lau, “Large actuation and high dielectric strength in metallized dielectric elastomer actuators,” *Applied Physics Letters*, vol. 100, no. 18, p. 182901, 2012.
- [33] C. Christianson, N. N. Goldberg, and M. T. Tolley, “Elastomeric diaphragm pump driven by fluid electrode dielectric elastomer actuators (fedeads),” in *Electroactive Polymer Actuators and Devices (EAPAD) XX*, vol. 10594, p. 105940O, International Society for Optics and Photonics, 2018.
- [34] C. Christianson, C. Bayag, G. Li, S. Jadhav, A. Giri, C. Agba, T. Li, and M. T. Tolley, “Jellyfish-inspired soft robot driven by fluid electrode dielectric organic robotic actuators,” *Frontiers in Robotics and AI*, vol. 6, p. 126, 2019.
- [35] D. Chen and Q. Pei, “Electronic muscles and skins: a review of soft sensors and actuators,” *Chemical reviews*, vol. 117, no. 17, pp. 11239–11268, 2017.

- [36] M. Sreekumar, T. Nagarajan, M. Singaperumal, M. Zoppi, and R. Molfino, “Critical review of current trends in shape memory alloy actuators for intelligent robots,” *Industrial Robot: An International Journal*, vol. 34, no. 4, pp. 285–294, 2007.
- [37] C. Ohm, M. Brehmer, and R. Zentel, “Liquid crystalline elastomers as actuators and sensors,” *Advanced Materials*, vol. 22, no. 31, pp. 3366–3387, 2010.
- [38] J. Sun and J. Zhao, “An adaptive walking robot with reconfigurable mechanisms using shape morphing joints,” *IEEE Robotics and Automation Letters*, vol. 4, no. 2, pp. 724–731, 2019.
- [39] M. A. McEvoy and N. Correll, “Shape-changing materials using variable stiffness and distributed control,” *Soft robotics*, vol. 5, no. 6, pp. 737–747, 2018.
- [40] E. Steltz, A. Mozeika, N. Rodenberg, E. Brown, and H. M. Jaeger, “Jsel: Jamming skin enabled locomotion,” in *2009 IEEE/RSJ International Conference on Intelligent Robots and Systems*, pp. 5672–5677, IEEE, 2009.
- [41] T. M. Simon, R. T. Smith, and B. H. Thomas, “Wearable jamming mitten for virtual environment haptics,” in *Proceedings of the 2014 ACM International Symposium on Wearable Computers*, pp. 67–70, ACM, 2014.
- [42] A. A. Stanley and A. M. Okamura, “Controllable surface haptics via particle jamming and pneumatics,” *IEEE transactions on haptics*, vol. 8, no. 1, pp. 20–30, 2015.
- [43] Z. Varga, G. Filipcsei, and M. Zrínyi, “Magnetic field sensitive functional elastomers with tuneable elastic modulus,” *Polymer*, vol. 47, no. 1, pp. 227–233, 2006.
- [44] B. J. Gemmell, J. H. Costello, S. P. Colin, C. J. Stewart, J. O. Dabiri, D. Tafti, and S. Priya, “Passive energy recapture in jellyfish contributes to propulsive advantage over other metazoans,” *Proceedings of the National Academy of Sciences*, vol. 110, no. 44, pp. 17904–17909, 2013.
- [45] V. van Ginneken, E. Antonissen, U. K. Müller, R. Booms, E. Eding, J. Verreth, and G. van den Thillart, “Eel migration to the sargasso: remarkably high swimming efficiency and low energy costs,” *Journal of Experimental Biology*, vol. 208, no. 7, pp. 1329–1335, 2005.
- [46] D. Webber and R. O’dor, “Monitoring the metabolic rate and activity of free-swimming squid with telemetered jet pressure,” *Journal of Experimental Biology*, vol. 126, no. 1, pp. 205–224, 1986.
- [47] R. K. Katzschmann, A. D. Marchese, and D. Rus, “Hydraulic autonomous soft robotic fish for 3d swimming,” in *Experimental Robotics*, pp. 405–420, Springer, 2016.
- [48] J. Zhu, C. White, D. Wainwright, V. Di Santo, G. Lauder, and H. Bart-Smith, “Tuna robotics: A high-frequency experimental platform exploring the performance space of swimming fishes,” *Science Robotics*, vol. 4, no. 34, p. eaax4615, 2019.

- [49] N. Live, “Rov hercules,” 2022.
- [50] U. Navy, “Attack submarines - ssn.”
- [51] J. Ayers, “Underwater walking,” *Arthropod structure & development*, vol. 33, no. 3, pp. 347–360, 2004.
- [52] H. C. Astley, “Getting around when you’re round: quantitative analysis of the locomotion of the blunt-spined brittle star, *ophiocomma echinata*,” *Journal of Experimental Biology*, vol. 215, no. 11, pp. 1923–1929, 2012.
- [53] M. Weissburg, C. James, D. Smee, and D. Webster, “Fluid mechanics produces conflicting, constraints during olfactory navigation of blue crabs, *callinectes sapidus*,” *Journal of Experimental Biology*, vol. 206, no. 1, pp. 171–180, 2003.
- [54] S. H. Maude and D. D. Williams, “Behavior of crayfish in water currents: hydrodynamics of eight species with reference to their distribution patterns in southern ontario,” *Canadian Journal of Fisheries and Aquatic Sciences*, vol. 40, no. 1, pp. 68–77, 1983.
- [55] K. J. Hayne and A. R. Palmer, “Intertidal sea stars (*pisaster ochraceus*) alter body shape in response to wave action,” *Journal of Experimental Biology*, vol. 216, no. 9, pp. 1717–1725, 2013.
- [56] J. Akizono, T. Tanaka, K. Nakagawa, T. Tsuji, and M. Iwasaki, “Seabottom roughness measurement by aquatic walking robot,” in *OCEANS’97. MTS/IEEE Conference Proceedings*, vol. 2, pp. 1395–1398, IEEE, 1997.
- [57] M. Cianchetti, M. Calisti, L. Margheri, M. Kuba, and C. Laschi, “Bioinspired locomotion and grasping in water: the soft eight-arm octopus robot,” *Bioinspiration & biomimetics*, vol. 10, no. 3, p. 035003, 2015.
- [58] D. Dodou, P. Breedveld, J. De Winter, J. Dankelman, and J. van Leeuwen, “Mechanisms of temporary adhesion in benthic animals,” *Biological Reviews*, vol. 86, no. 1, pp. 15–32, 2011.
- [59] R. Santos, S. Gorb, V. Jamar, and P. Flammang, “Adhesion of echinoderm tube feet to rough surfaces,” *Journal of Experimental Biology*, vol. 208, no. 13, pp. 2555–2567, 2005.
- [60] J. Von Byern and W. Klepal, “Adhesive mechanisms in cephalopods: a review,” *Biofouling*, vol. 22, no. 5, pp. 329–338, 2006.
- [61] W. M. Kier and A. M. Smith, “The structure and adhesive mechanism of octopus suckers,” *Integrative and Comparative Biology*, vol. 42, no. 6, pp. 1146–1153, 2002.
- [62] H. Albitar, K. Dandan, A. Ananiev, and I. Kalaykov, “Underwater robotics: surface cleaning technics, adhesion and locomotion systems,” *International Journal of Advanced Robotic Systems*, vol. 13, no. 1, p. 7, 2016.

- [63] M. Follador, F. Tramacere, and B. Mazzolai, “Dielectric elastomer actuators for octopus inspired suction cups,” *Bioinspiration & biomimetics*, vol. 9, no. 4, p. 046002, 2014.
- [64] A. Sadeghi, L. Beccai, and B. Mazzolai, “Design and development of innovative adhesive suckers inspired by the tube feet of sea urchins,” in *2012 4th IEEE RAS & EMBS International Conference on Biomedical Robotics and Biomechatronics (BioRob)*, pp. 617–622, IEEE, 2012.
- [65] J. A. Sandoval, S. Jadhav, H. Quan, D. D. Deheyn, and M. T. Tolley, “Reversible adhesion to rough surfaces both in and out of water, inspired by the clingfish suction disc,” *Bioinspiration & Biomimetics*, vol. 14, no. 6, p. 066016, 2019.
- [66] T. Paschal, M. A. Bell, J. Sperry, S. Sieniewicz, R. J. Wood, and J. C. Weaver, “Design, fabrication, and characterization of an untethered amphibious sea urchin-inspired robot,” *IEEE Robotics and Automation Letters*, vol. 4, no. 4, pp. 3348–3354, 2019.
- [67] M. Calisti, G. Picardi, and C. Laschi, “Fundamentals of soft robot locomotion,” *Journal of The Royal Society Interface*, vol. 14, no. 130, p. 20170101, 2017.
- [68] J. O. Dabiri, S. P. Colin, and J. H. Costello, “Fast-swimming hydromedusae exploit velar kinematics to form an optimal vortex wake,” *Journal of Experimental Biology*, vol. 209, no. 11, pp. 2025–2033, 2006.
- [69] J. O. Dabiri, “Optimal vortex formation as a unifying principle in biological propulsion,” *Annual review of fluid mechanics*, vol. 41, pp. 17–33, 2009.
- [70] S. Steele, G. Weymouth, and M. Triantafyllou, “Added mass energy recovery of octopus-inspired shape change,” *Journal of Fluid Mechanics*, vol. 810, pp. 155–174, 2017.
- [71] F. Giorgio-Serchi and G. D. Weymouth, “Drag cancellation by added-mass pumping,” *Journal of fluid Mechanics*, vol. 798, 2016.
- [72] W. Johnson, P. Soden, and E. Trueman, “A study in jet propulsion: an analysis of the motion of the squid, *loligo vulgaris*,” *Journal of Experimental Biology*, vol. 56, no. 1, pp. 155–165, 1972.
- [73] J. M. Gosline and M. E. DeMont, “Jet-propelled swimming in squids,” *Sci. Am*, vol. 252, no. 1, pp. 96–103, 1985.
- [74] C. Wardle, “Limit of fish swimming speed,” *Nature*, vol. 255, no. 5511, p. 725, 1975.
- [75] S. Iacoponi, G. Picardi, M. Chellapurath, M. Calisti, and L. Cecilia, “Underwater soft jet propulsion based on a hoberman mechanism,” in *2018 IEEE International Conference on Soft Robotics (RoboSoft)*, pp. 449–454, IEEE, 2018.
- [76] G. Weymouth, V. Subramaniam, and M. Triantafyllou, “Ultra-fast escape maneuver of an octopus-inspired robot,” *Bioinspiration & biomimetics*, vol. 10, no. 1, p. 016016, 2015.

- [77] F. G. Serchi, A. Arienti, and C. Laschi, “Biomimetic vortex propulsion: toward the new paradigm of soft unmanned underwater vehicles,” *IEEE/ASME Transactions On Mechatronics*, vol. 18, no. 2, pp. 484–493, 2012.
- [78] J. Frame, N. Lopez, O. Curet, and E. D. Engeberg, “Thrust force characterization of free-swimming soft robotic jellyfish,” *Bioinspiration & biomimetics*, vol. 13, no. 6, p. 064001, 2018.
- [79] A. Villanueva, C. Smith, and S. Priya, “A biomimetic robotic jellyfish (robojelly) actuated by shape memory alloy composite actuators,” *Bioinspiration & biomimetics*, vol. 6, no. 3, p. 036004, 2011.
- [80] T. Cheng, G. Li, Y. Liang, M. Zhang, B. Liu, T.-W. Wong, J. Forman, M. Chen, G. Wang, Y. Tao, *et al.*, “Untethered soft robotic jellyfish,” *Smart Materials and Structures*, vol. 28, no. 1, p. 015019, 2018.
- [81] F. E. Fish, “Transitions from drag-based to lift-based propulsion in mammalian swimming,” *American Zoologist*, vol. 36, no. 6, pp. 628–641, 1996.
- [82] S. Vogel, *Life in moving fluids: the physical biology of flow*. Princeton University Press, 1994.
- [83] C. M. Pace, R. W. Blob, and M. W. Westneat, “Comparative kinematics of the forelimb during swimming in red-eared slider (*trachemys scripta*) and spiny softshell (*apalone spinifera*) turtles,” *Journal of Experimental Biology*, vol. 204, no. 19, pp. 3261–3271, 2001.
- [84] X. Jia, Z. Chen, A. Riedel, W. R. Hamel, and M. Zhang, “Energy-efficient propulsion inspired by whirligig beetles,” in *2014 IEEE International Conference on Robotics and Automation (ICRA)*, pp. 2463–2468, IEEE, 2014.
- [85] Y. Tang, L. Qin, X. Li, C.-M. Chew, and J. Zhu, “A frog-inspired swimming robot based on dielectric elastomer actuators,” in *2017 IEEE/RSJ International Conference on Intelligent Robots and Systems (IROS)*, pp. 2403–2408, IEEE, 2017.
- [86] X. Jia, Z. Chen, A. Riedel, T. Si, W. R. Hamel, and M. Zhang, “Energy-efficient surface propulsion inspired by whirligig beetles,” *IEEE Transactions on Robotics*, vol. 31, no. 6, pp. 1432–1443, 2015.
- [87] H.-J. Kim, S.-H. Song, and S.-H. Ahn, “A turtle-like swimming robot using a smart soft composite (ssc) structure,” *Smart Materials and Structures*, vol. 22, no. 1, p. 014007, 2012.
- [88] P. W. Webb, “Form and function in fish swimming,” *scientific American*, vol. 251, no. 1, pp. 58–68, 1984.

- [89] M. Sfakiotakis, D. M. Lane, and J. B. C. Davies, “Review of fish swimming modes for aquatic locomotion,” *IEEE Journal of oceanic engineering*, vol. 24, no. 2, pp. 237–252, 1999.
- [90] R. Godoy-Diana, J.-L. Aider, and J. E. Wesfreid, “Transitions in the wake of a flapping foil,” *Physical Review E*, vol. 77, no. 1, p. 016308, 2008.
- [91] O. Akanyeti, J. Putney, Y. R. Yanagitsuru, G. V. Lauder, W. J. Stewart, and J. C. Liao, “Accelerating fishes increase propulsive efficiency by modulating vortex ring geometry,” *Proceedings of the National Academy of Sciences*, vol. 114, no. 52, pp. 13828–13833, 2017.
- [92] P. G. Saffman, *Vortex dynamics*. Cambridge university press, 1992.
- [93] Kochin, *Theoretical hydromechanics*. Interscience publishers, 1964.
- [94] C. Eloy, “Optimal strouhal number for swimming animals,” *Journal of Fluids and Structures*, vol. 30, pp. 205–218, 2012.
- [95] D. Tzeranis, E. Papadopoulos, and G. Triantafyllou, “On the design of an autonomous robot fish,” in *Proc. of the 11th IEEE Mediterranean Conf. on Control and Automation*, pp. 17–20, 2003.
- [96] D. Barrett, M. Triantafyllou, D. Yue, M. Grosenbaugh, and M. Wolfgang, “Drag reduction in fish-like locomotion,” *Journal of Fluid Mechanics*, vol. 392, pp. 183–212, 1999.
- [97] A. Punning, M. Anton, M. Kruusmaa, and A. Aabloo, “A biologically inspired ray-like underwater robot with electroactive polymer pectoral fins,” in *International IEEE conference on mechatronics and robotics*, vol. 2004, pp. 241–245, 2004.
- [98] M. S. Triantafyllou and G. S. Triantafyllou, “An efficient swimming machine,” *Scientific american*, vol. 272, no. 3, pp. 64–70, 1995.
- [99] W. Zhao, J. Yu, Y. Fang, and L. Wang, “Development of multi-mode biomimetic robotic fish based on central pattern generator,” in *2006 IEEE/RSJ International Conference on Intelligent Robots and Systems*, pp. 3891–3896, IEEE, 2006.
- [100] A. Thomas, M. Milano, M. G. G’Sell, K. Fischer, and J. Burdick, “Synthetic jet propulsion for small underwater vehicles,” in *Robotics and Automation, 2005. ICRA 2005. Proceedings of the 2005 IEEE International Conference on*, pp. 181–187, IEEE, 2005.
- [101] F. Azis, M. Aras, M. Rashid, M. Othman, and S. Abdullah, “Problem identification for underwater remotely operated vehicle (rov): A case study,” *Procedia Engineering*, vol. 41, pp. 554–560, 2012.
- [102] J. Siekmann, “On a pulsating jet from the end of a tube, with application to the propulsion of certain aquatic animals,” *Journal of Fluid Mechanics*, vol. 15, no. 3, pp. 399–418, 1963.

- [103] M. Sfakiotakis, D. M. Lane, and J. B. C. Davies, “Review of fish swimming modes for aquatic locomotion,” *IEEE Journal of oceanic engineering*, vol. 24, no. 2, pp. 237–252, 1999.
- [104] J. Ayers, “Underwater walking,” *Arthropod structure & development*, vol. 33, no. 3, pp. 347–360, 2004.
- [105] G. Kerkut, “The forces exerted by the tube feet of the starfish during locomotion,” *Journal of Experimental Biology*, vol. 30, no. 4, pp. 575–583, 1953.
- [106] M. M. Martinez, R. Full, and M. Koehl, “Underwater punting by an intertidal crab: a novel gait revealed by the kinematics of pedestrian locomotion in air versus water,” *Journal of Experimental Biology*, vol. 201, no. 18, pp. 2609–2623, 1998.
- [107] M. A. Ashley-Ross, R. Lundin, and K. L. Johnson, “Kinematics of level terrestrial and underwater walking in the california newt, *taricha torosa*,” *Journal of Experimental Zoology Part A: Ecological and Integrative Physiology*, vol. 311, no. 4, pp. 240–257, 2009.
- [108] K. Karakasiliotis, R. Thandiackal, K. Melo, T. Horvat, N. Mahabadi, S. Tsitkov, J. Caberguen, and A. Ijspeert, “From cineradiography to biorobots: an approach for designing robots to emulate and study animal locomotion,” *Journal of The Royal Society Interface*, vol. 13, no. 119, p. 20151089, 2016.
- [109] M. Weissburg, C. James, D. Smee, and D. Webster, “Fluid mechanics produces conflicting, constraints during olfactory navigation of blue crabs, *callinectes sapidus*,” *Journal of Experimental Biology*, vol. 206, no. 1, pp. 171–180, 2003.
- [110] S. Steele, J. Dahl, G. Weymouth, and M. Triantafyllou, “Shape of retracting foils that model morphing bodies controls shed energy and wake structure,” *Journal of Fluid Mechanics*, vol. 805, pp. 355–383, 2016.
- [111] E. G. Drucker and G. V. Lauder, “A hydrodynamic analysis of fish swimming speed: wake structure and locomotor force in slow and fast labriform swimmers,” *Journal of Experimental Biology*, vol. 203, no. 16, pp. 2379–2393, 2000.
- [112] A. Packard, “Jet propulsion and the giant fibre response of loligo,” *Nature*, vol. 221, no. 5183, p. 875, 1969.
- [113] A. Arienti, M. Calisti, F. Giorgio-Serchi, and C. Laschi, “Poseidrone: design of a soft-bodied roV with crawling, swimming and manipulation ability,” in *Oceans-San Diego, 2013*, pp. 1–7, IEEE, 2013.
- [114] F. Corucci, M. Calisti, H. Hauser, and C. Laschi, “Novelty-based evolutionary design of morphing underwater robots,” in *Proceedings of the 2015 annual conference on Genetic and Evolutionary Computation*, pp. 145–152, ACM, 2015.

- [115] J. Pikul, S. Li, H. Bai, R. Hanlon, I. Cohen, and R. Shepherd, “Stretchable surfaces with programmable 3d texture morphing for synthetic camouflaging skins,” *Science*, vol. 358, no. 6360, pp. 210–214, 2017.
- [116] H.-J. Kim, S.-H. Song, and S.-H. Ahn, “A turtle-like swimming robot using a smart soft composite (ssc) structure,” *Smart Materials and Structures*, vol. 22, no. 1, p. 014007, 2012.
- [117] J. Colorado, A. Barrientos, C. Rossi, and K. S. Breuer, “Biomechanics of smart wings in a bat robot: morphing wings using sma actuators,” *Bioinspiration & biomimetics*, vol. 7, no. 3, p. 036006, 2012.
- [118] D. Rus and M. T. Tolley, “Design, fabrication and control of soft robots,” *Nature*, vol. 521, no. 7553, p. 467, 2015.
- [119] A. D. Marchese, C. D. Onal, and D. Rus, “Autonomous soft robotic fish capable of escape maneuvers using fluidic elastomer actuators,” *Soft Robotics*, vol. 1, no. 1, pp. 75–87, 2014.
- [120] A. D. Marchese, R. K. Katzschmann, and D. Rus, “A recipe for soft fluidic elastomer robots,” *Soft Robotics*, vol. 2, no. 1, pp. 7–25, 2015.
- [121] F. Connolly, C. J. Walsh, and K. Bertoldi, “Automatic design of fiber-reinforced soft actuators for trajectory matching,” *Proceedings of the National Academy of Sciences*, vol. 114, no. 1, pp. 51–56, 2017.
- [122] B. Mosadegh, P. Polygerinos, C. Keplinger, S. Wennstedt, R. F. Shepherd, U. Gupta, J. Shim, K. Bertoldi, C. J. Walsh, and G. M. Whitesides, “Pneumatic networks for soft robotics that actuate rapidly,” *Advanced functional materials*, vol. 24, no. 15, pp. 2163–2170, 2014.
- [123] C.-P. Chou and B. Hannaford, “Measurement and modeling of mckibben pneumatic artificial muscles,” *IEEE Transactions on robotics and automation*, vol. 12, no. 1, pp. 90–102, 1996.
- [124] R. V. Martinez, J. L. Branch, C. R. Fish, L. Jin, R. F. Shepherd, R. Nunes, Z. Suo, and G. M. Whitesides, “Robotic tentacles with three-dimensional mobility based on flexible elastomers,” *Advanced materials*, vol. 25, no. 2, pp. 205–212, 2013.
- [125] P. Glick, S. Suresh, D. Ruffatto III, M. Cutkosky, M. T. Tolley, and A. Parness, “A soft robotic gripper with gecko-inspired adhesive,” *IEEE Robotics and Automation Letters*, 2018.
- [126] M. Calisti, F. Corucci, A. Arienti, and C. Laschi, “Dynamics of underwater legged locomotion: modeling and experiments on an octopus-inspired robot,” *Bioinspiration & biomimetics*, vol. 10, no. 4, p. 046012, 2015.

- [127] H. Greiner, A. Sheckman, C. Won, R. Elsley, and P. Beith, “Autonomous legged underwater vehicles for near land warfare,” in *Autonomous Underwater Vehicle Technology, 1996. AUV’96., Proceedings of the 1996 Symposium on*, pp. 41–48, IEEE, 1996.
- [128] M. Calisti, E. Falotico, and C. Laschi, “Hopping on uneven terrains with an underwater one-legged robot,” *IEEE Robotics and Automation Letters*, vol. 1, no. 1, pp. 461–468, 2016.
- [129] G. Wang, X. Chen, S. Yang, P. Jia, X. Yan, and J. Xie, “Subsea crab bounding gait of leg-paddle hybrid driven shoal crablike robot,” *Mechatronics*, vol. 48, pp. 1–11, 2017.
- [130] D. Drotman, M. Ishida, S. Jadhav, and M. T. Tolley, “Application-driven design of soft, 3d printed, pneumatic actuators with bellows,” *IEEE/ASME Transactions on Mechatronics*, 2018.
- [131] D. Drotman, S. Jadhav, M. Karimi, M. T. Tolley, *et al.*, “3d printed soft actuators for a legged robot capable of navigating unstructured terrain,” in *Robotics and Automation (ICRA), 2017 IEEE International Conference on*, pp. 5532–5538, IEEE, 2017.
- [132] T. Kalisky, Y. Wang, B. Shih, D. Drotman, S. Jadhav, E. Aronoff-Spencer, and M. T. Tolley, “Differential pressure control of 3d printed soft fluidic actuators,” in *2017 IEEE/RSJ International Conference on Intelligent Robots and Systems (IROS)*, pp. 6207–6213, IEEE, 2017.
- [133] P. M. Favi, S. Yi, S. C. Lengahan, L. Xia, and M. Zhang, “Inspiration from the natural world: from bio-adhesives to bio-inspired adhesives,” *Journal of Adhesion Science and Technology*, vol. 28, no. 3–4, pp. 290–319, 2011.
- [134] S. Kim, M. Spenko, S. Trujillo, B. Heyneman, D. Santos, and M. R. Cutkosky, “Smooth vertical surface climbing with directional adhesion,” *IEEE Transactions on Robotics*, vol. 24, no. 1, pp. 65–74, 2008.
- [135] M. R. Cutkosky, “Climbing with adhesion: from bioinspiration to biounderstanding,” *Interface Focus*, vol. 5, p. 20150015, 2015.
- [136] K. Autumn, Y. A. Liang, S. T. Hsieh, W. Zesch, W. P. Chan, T. W. Kenny, R. Fearing, and R. J. Full, “Adhesive force of a single gecko foot-hair,” *Nature*, vol. 405, pp. 681–685, 2000.
- [137] J. M. Bullock, P. Drechsler, and W. Federle, “Comparison of smooth and hairy attachment pads in insects: friction, adhesion and mechanisms for direction-dependence,” *Journal of Experimental Biology*, vol. 211, pp. 3333–3343, 2008.
- [138] S. Heydari, A. Johnson, O. Ellers, M. J. McHenry, and E. Kanso, “Sea star inspired crawling and bouncing,” *Journal of the Royal Society Interface*, vol. 17, no. 162, p. 20190700, 2020.

- [139] L. F. Boesel, C. Greiner, E. Arzt, and A. del Campo, “Gecko-inspired surfaces: A path to strong and reversible dry adhesives,” *Advanced Materials*, vol. 22, pp. 2125–2137, 2010.
- [140] S. Kalouche, N. Wiltsie, H.-J. Su, and A. Parness, “Inchworm style gecko adhesive climbing robot,” in *2014 IEEE/RSJ International Conference on Intelligent Robots and Systems (IROS)*, pp. 2319–2324, IEEE, 2014.
- [141] K. Daltorio, T. Wei, A. Horchler, L. Southard, G. Wile, R. Quinn, S. Gorb, and R. Ritzmann, “Mini-whegs tm climbs steep surfaces using insect-inspired attachment mechanisms,” *I. J. Robotic Res.*, vol. 28, pp. 285–302, 02 2009.
- [142] P. Manoonpong, D. Petersen, A. Kovalev, F. Wörgötter, S. N. Gorb, M. Spinner, and L. Heepe, “Enhanced locomotion efficiency of a bio-inspired walking robot using contact surfaces with frictional anisotropy,” *Scientific Reports*, vol. 6, p. 39455, 2016.
- [143] J. Cao, L. Qin, J. Liu, Q. Ren, C. C. Foo, H. Wang, H. P. Lee, and J. Zhu, “Untethered soft robot capable of stable locomotion using soft electrostatic actuators,” *Extreme Mechanics Letters*, vol. 21, pp. 9–16, 2018.
- [144] S. D. de Rivaz, B. Goldberg, N. Doshi, K. Jayaram, J. Zhou, and R. J. Wood, “Inverted and vertical climbing of a quadrupedal microrobot using electroadhesion,” *Science Robotics*, vol. 3, no. 25, p. eaau3038, 2018.
- [145] Y. Hou, X. Deng, and C. Xie, “Biomaterial surface modification for underwater adhesion,” *Smart Materials in Medicine*, vol. 1, pp. 77–91, 2020.
- [146] M. A. Bell, I. Pestovski, W. Scott, K. Kumar, M. K. Jawed, D. A. Paley, C. Majidi, J. C. Weaver, and R. J. Wood, “Echinoderm-inspired tube feet for robust robot locomotion and adhesion,” *IEEE Robotics and Automation Letters*, vol. 3, no. 3, pp. 2222–2228, 2018.
- [147] X. Tang, D. Zhang, Z. Li, and J. Chen, “An omni-directional wall-climbing microrobot with magnetic wheels directly integrated with electromagnetic micromotors,” *International Journal of Advanced Robotic Systems*, vol. 9, no. 16, 2012.
- [148] Z. Ye, G. Z. Lum, S. Song, S. Rich, and M. Sitti, “Phase change of gallium enables highly reversible and switchable adhesion,” *Advanced Materials*, vol. 28, pp. 5088–5092, 2016.
- [149] W. P. Weston-Dawkes, I. Adibnazari, Y.-W. Hu, M. Everman, N. Gravish, and M. T. Tolley, “Gas-lubricated vibration-based adhesion for robotics,” *Advanced Intelligent Systems*, p. 2100001, 2021.
- [150] S. Kawasaki and K. Kikuchi, “Development of a small legged wall climbing robot with passive suction cups,” in *The 3rd International Conference on Design Engineering and Science, ICDES*, vol. 2014, pp. 112–116, 2014.
- [151] G. Lee, H. Kim, K. Seo, J. Kim, and H. S. Kim, “Multitrack: A multi-linked track robot with suction adhesion for climbing and transition,” *Robotics and Autonomous Systems*, vol. 72, pp. 207–216, 2015.

- [152] Y. Tang, Q. Zhang, G. Lin, and J. Yin, “Switchable adhesion actuator for amphibious climbing soft robot,” *Soft Robotics*, vol. 5, no. 5, pp. 592–600, 2018.
- [153] T. Miyake, H. Ishihara, and M. Yoshimura, “Basic studies on wet adhesion system for wall climbing robots,” in *2007 IEEE/RSJ International Conference on Intelligent Robots and Systems (IROS)*, pp. 1920–1925, IEEE, 2007.
- [154] D. Santos, S. Kim, M. Spenko, A. Parness, and M. Cutkosky, “Directional adhesive structures for controlled climbing on smooth vertical surfaces,” in *Proceedings of the 2007 IEEE International Conference on Robotics and Automation*, pp. 1262–1267, IEEE, 2007.
- [155] D. Santos, M. Spenko, A. Parness, S. Kim, and M. Cutkosky, “Directional adhesion for climbing: theoretical and practical considerations,” *Journal of Adhesion Science and Technology*, vol. 21, no. 12-13, pp. 1317–1341, 2007.
- [156] H. Hauser, A. J. Ijspeert, R. M. Fuchslin, R. Pfeifer, and W. Maass, “Towards a theoretical foundation for morphological computation with compliant bodies,” *Biological Cybernetics*, vol. 105, pp. 355–370, 2011.
- [157] M. McEnvoy and N. Correll, “Materials that couple sensing, actuation, computation, and communication,” *Science*, vol. 347, no. 6228, p. 1261689, 2015.
- [158] C. Laschi and B. Mazzolai, “Lessons from animals and plants: The symbiosis of morphological computation and soft robotics,” *IEEE Robotics Automation Magazine*, vol. 23, no. 3, pp. 107–114, 2016.
- [159] R. Pfeifer, M. Lungarella, and I. Fumiya, “Self-organization, embodiment, and biologically inspired robotics,” *Science*, vol. 318, no. 5853, pp. 1088–1093, 2007.
- [160] W. Federle and D. Labonte, “Dynamic biological adhesion: mechanisms for controlling attachment during locomotion,” *Philosophical Transactions of the Royal Society B*, vol. 374, p. 20190199, 2019.
- [161] H. Gai, X. Wang, H. Yao, S. Gorb, and E. Arzt, “Mechanics of hierarchical adhesion structures of geckos,” *Mechanics of Materials*, vol. 37, pp. 275–285, 2005.
- [162] K. Autumn, M. Sitti, Y. A. Liang, A. A. Peattie, W. R. Hansen, S. Sponberg, T. W. Kenny, R. Fearing, J. N. Israelachvili, and R. J. Full, “Evidence for van der waals adhesion in gecko setae,” *PNAS*, vol. 99, no. 19, pp. 12252–12256, 2002.
- [163] G. C. Hill, D. R. Soto, A. M. Peattie, R. J. Full, and T. Kenny, “Orientation angle and the adhesion of single gecko setae,” *Journal of the Royal Society Interface*, vol. 8, pp. 926–933, 2011.
- [164] M. P. Murphy, B. Aksak, and M. Sitti, “Gecko-inspired directional and controllable adhesion,” *Small*, vol. 5, no. 2, pp. 170–175, 2009.

- [165] A. Parness, D. Soto, N. Esparza, N. Gravish, M. Wilkinson, K. Autumn, and M. Cutkosky, “A microfabricated wedge-shaped adhesive array displaying gecko-like dynamic adhesion, directionality and long lifetime,” *Journal of the Royal Society Interface*, vol. 6, pp. 1223–1232, 2009.
- [166] L. Heepe, A. E. Kovalev, and S. N. Gorb, “Direct observation of microcavitation in underwater adhesion of mushroom-shaped adhesive microstructure,” *Beilstein Journal of Nanotechnology*, vol. 5, pp. 903–909, 2014.
- [167] H. Lee, B. Lee, and P. Messersmith, “A reversible wet/dry adhesive inspired by mussels and geckos,” *Nature*, vol. 448, no. 7151, pp. 338–341, 2007.
- [168] H. Yi, S. H. Lee, M. Seong, M. K. Kwak, and H. E. Jeong, “Bioinspired reversible hydrogel adhesives for wet and underwater surfaces,” *Journal of Materials Chemistry B*, vol. 6, pp. 8064–8070, 2018.
- [169] Y. Wang, V. Kang, E. Arzt, W. Federle, and R. Hensel, “Strong wet and dry adhesion by cupped microstructures,” *ACS Applied Materials and Interfaces*, vol. 11, pp. 26483–26490, 2019.
- [170] D. Dodou, P. Breedveld, J. De Winter, J. Dankelman, and J. Van Leeuwen, “Mechanisms of temporary adhesion in benthic animals,” *Biological Reviews*, vol. 86, no. 1, pp. 15–32, 2011.
- [171] K. M. Gamel, A. M. Garner, and B. E. Flammang, “Bioinspired remora adhesive disc offers insight into evolution,” *Bioinspiration & Biomimetics*, vol. 14, no. 5, p. 056014, 2019.
- [172] H. Bagheri, A. Hu, S. Cummings, C. Roy, R. Casleton, A. Wan, N. Erjavic, S. Berman, M. M. Peet, D. M. Aukes, *et al.*, “New insights on the control and function of octopus suckers,” *Advanced Intelligent Systems*, vol. 2, no. 6, p. 1900154, 2020.
- [173] P. Ditsche, D. K. Wainwright, and A. P. Summers, “Attachment to challenging substrates—fouling, roughness and limits of adhesion in the northern clingfish (*gobiesox maeandricus*),” *Journal of Experimental Biology*, vol. 217, no. 14, pp. 2548–2554, 2014.
- [174] M. Elbadawi, G. Andrikopoulos, G. Nikolakopoulos, and T. Gustafsson, “Bio-inspired climbing robots in wet environments: Recent trends in adhesion methods and materials,” in *2018 IEEE International Conference on Robotics and Biomimetics (ROBIO)*, pp. 2347–2353, IEEE, 2018.
- [175] Y. Wang, X. Yang, Y. Chen, D. K. Wainwright, C. P. Kenaley, Z. Gong, Z. Liu, H. Liu, J. Guan, T. Wang, *et al.*, “A biorobotic adhesive disc for underwater hitchhiking inspired by the remora suckerfish,” *Science Robotics*, vol. 2, no. 10, p. ean8072, 2017.
- [176] P. Ditsche and A. Summers, “Learning from northern clingfish (*gobiesox maeandricus*): bioinspired suction cups attach to rough surfaces,” *Philosophical Transactions of the Royal Society B*, vol. 374, no. 1784, p. 20190204, 2019.

- [177] S. Sareh, K. Althoefer, M. Li, Y. Noh, F. Tramacere, P. Sareh, B. Mazzolai, and M. Kovac, “Anchoring like octopus: biologically inspired soft artificial sucker,” *Journal of the Royal Society Interface*, vol. 14, no. 135, p. 20170395, 2017.
- [178] Z. Xie, A. G. Domel, N. An, C. Green, Z. Gong, T. Wang, E. M. Knubben, J. C. Weaver, K. Bertoldi, and L. Wen, “Octopus arm-inspired tapered soft actuators with suckers for improved grasping,” *Soft robotics*, vol. 7, no. 5, pp. 639–648, 2020.
- [179] S. Wang, L. Li, W. Sun, D. Wainwright, H. Wang, W. Zhao, B. Chen, Y. Chen, and L. Wen, “Detachment of the remora suckerfish disc: kinematics and a bio-inspired robotic model,” *Bioinspiration & Biomimetics*, vol. 15, p. 056018, 2020.
- [180] H. Tsukagoshi and Y. Osada, “Soft hybrid suction cup capable of sticking to various objects and environments,” in *Actuators*, vol. 10, p. 50, Multidisciplinary Digital Publishing Institute, 2021.
- [181] Z. Zhakypov, F. Heremans, A. Billard, and J. Paik, “An origami-inspired reconfigurable suction gripper for picking objects with variable shape and size,” *IEEE Robotics and Automation Letters*, vol. 3, no. 4, pp. 2894–2901, 2018.
- [182] D. M. Green and D. L. Barber, “The ventral adhesive disc of the clingfish *Gobiesox maeandricus*: integumental structure and adhesive mechanisms,” *Canadian Journal of Zoology*, vol. 66, pp. 1610–1619, 1988.
- [183] A. Tiwari and B. Persson, “Physics of suction cups,” *Soft Matter*, vol. 15, no. 46, pp. 9482–9499, 2019.
- [184] J. Y. Han, “Low-cost multi-touch sensing through frustrated total internal reflection,” in *Proceedings of the 18th Annual ACM Symposium on User Interface Software and Technology*, pp. 115–118, 2005.
- [185] O. Eilers, A. Johnson, and T. Motokawa, “Do general theories of locomotion apply to underwater walkers?,” in *Integrative and Comparative Biology*, vol. 58, pp. E57–E57, Oxford University Press, 2018.
- [186] S. Aracri, F. Giorgio-Serchi, G. Suaria, M. E. Sayed, M. P. Nemitz, S. Mahon, and A. A. Stokes, “Soft robots for ocean exploration and offshore operations: A perspective,” *Soft Robotics*, vol. 8, no. 6, pp. 625–639, 2021.
- [187] K. C. Galloway, K. P. Becker, B. Phillips, J. Kirby, S. Licht, D. Tchernov, R. J. Wood, and D. F. Gruber, “Soft robotic grippers for biological sampling on deep reefs,” *Soft robotics*, vol. 3, no. 1, pp. 23–33, 2016.
- [188] T. E. Laidig, L. M. Krigsman, and M. M. Yoklavich, “Reactions of fishes to two underwater survey tools, a manned submersible and a remotely operated vehicle,” *Fishery Bulletin*, vol. 111, no. 1, pp. 54–67, 2013.

- [189] B. Bingham, B. Foley, H. Singh, R. Camilli, K. Delaporta, R. Eustice, A. Mallios, D. Mindell, C. Roman, and D. Sakellariou, “Robotic tools for deep water archaeology: Surveying an ancient shipwreck with an autonomous underwater vehicle,” *Journal of Field Robotics*, vol. 27, no. 6, pp. 702–717, 2010.
- [190] S. H. Maude and D. D. Williams, “Behavior of crayfish in water currents: hydrodynamics of eight species with reference to their distribution patterns in southern ontario,” *Canadian Journal of Fisheries and Aquatic Sciences*, vol. 40, no. 1, pp. 68–77, 1983.
- [191] J. Smith, “The activities of the tube feet of *asterias rubens* l: I. the mechanics of movement and of posture,” *Journal of Cell Science*, vol. 3, no. 1, pp. 1–14, 1947.
- [192] P. Flammang, A. Michel, A. Cauwenberge, H. Alexandre, and M. Jangoux, “A study of the temporary adhesion of the podia in the sea star *asterias rubens* (echinodermata, asteroidea) through their footprints,” *The Journal of experimental biology*, vol. 201, no. 16, pp. 2383–2395, 1998.
- [193] E. Hennebert, D. Haesaerts, P. Dubois, and P. Flammang, “Evaluation of the different forces brought into play during tube foot activities in sea stars,” *Journal of Experimental Biology*, vol. 213, no. 7, pp. 1162–1174, 2010.
- [194] S. Heydari, A. Johnson, O. Ellers, M. J. McHenry, and E. Kanso, “Sea star inspired crawling and bouncing,” *Journal of The Royal Society Interface*, vol. 17, no. 162, p. 20190700, 2020.
- [195] O. Ellers, M. Khoriaty, and A. S. Johnson, “Kinematics of sea star legged locomotion,” *Journal of Experimental Biology*, vol. 224, no. 22, p. jeb242813, 2021.
- [196] D. Trivedi, C. D. Rahn, W. M. Kier, and I. D. Walker, “Soft robotics: Biological inspiration, state of the art, and future research,” *Applied bionics and biomechanics*, vol. 5, no. 3, pp. 99–117, 2008.
- [197] D. Rus and M. T. Tolley, “Design, fabrication and control of soft robots,” *Nature*, vol. 521, no. 7553, p. 467, 2015.
- [198] Z. Xie, A. G. Domel, N. An, C. Green, Z. Gong, T. Wang, E. M. Knubben, J. C. Weaver, K. Bertoldi, and L. Wen, “Octopus arm-inspired tapered soft actuators with suckers for improved grasping,” *Soft robotics*, vol. 7, no. 5, pp. 639–648, 2020.
- [199] M. T. Tolley, R. F. Shepherd, B. Mosadegh, K. C. Galloway, M. Wehner, M. Karpelson, R. J. Wood, and G. M. Whitesides, “A resilient, untethered soft robot,” *Soft robotics*, vol. 1, no. 3, pp. 213–223, 2014.
- [200] M. Calisti, F. Corucci, A. Arienti, and C. Laschi, “Dynamics of underwater legged locomotion: modeling and experiments on an octopus-inspired robot,” *Bioinspiration & biomimetics*, vol. 10, no. 4, p. 046012, 2015.

- [201] C. Christianson, N. N. Goldberg, D. D. Deheyn, S. Cai, and M. T. Tolley, “Translucent soft robots driven by frameless fluid electrode dielectric elastomer actuators,” *Science Robotics*, vol. 3, no. 17, p. eaat1893, 2018.
- [202] T. Li, G. Li, Y. Liang, T. Cheng, J. Dai, X. Yang, B. Liu, Z. Zeng, Z. Huang, Y. Luo, *et al.*, “Fast-moving soft electronic fish,” *Science advances*, vol. 3, no. 4, p. e1602045, 2017.
- [203] J. Bishop-Moser and S. Kota, “Design and modeling of generalized fiber-reinforced pneumatic soft actuators,” *IEEE Transactions on Robotics*, vol. 31, no. 3, pp. 536–545, 2015.
- [204] O. Unver, A. Uneri, A. Aydemir, and M. Sitti, “Geckobot: A gecko inspired climbing robot using elastomer adhesives,” in *Proceedings 2006 IEEE International Conference on Robotics and Automation, 2006. ICRA 2006.*, pp. 2329–2335, IEEE, 2006.
- [205] H. Prahlad, R. Pelrine, S. Stanford, J. Marlow, and R. Kornbluh, “Electroadhesive robots—wall climbing robots enabled by a novel, robust, and electrically controllable adhesion technology,” in *2008 IEEE international conference on robotics and automation*, pp. 3028–3033, IEEE, 2008.
- [206] G. Gu, J. Zou, R. Zhao, X. Zhao, and X. Zhu, “Soft wall-climbing robots,” *Science Robotics*, vol. 3, no. 25, p. eaat2874, 2018.
- [207] W. Fischer, F. Tâche, and R. Siegwart, “Inspection system for very thin and fragile surfaces, based on a pair of wall climbing robots with magnetic wheels,” in *2007 IEEE/RSJ International Conference on Intelligent Robots and Systems*, pp. 1216–1221, IEEE, 2007.
- [208] E. Hennebert, R. Santos, and P. Flammang, “Echinoderms don’t suck: evidence against the involvement of suction in tube foot attachment,” *Zoosymposia*, vol. 7, pp. 25–32, 2012.
- [209] A. Tiwari and B. Persson, “Physics of suction cups,” *Soft matter*, vol. 15, no. 46, pp. 9482–9499, 2019.
- [210] J. A. Sandoval, M. Ishida, S. Jadhav, S. Huen, and M. T. Tolley, “Tuning the morphology of suction discs to enable directional adhesion for locomotion in wet environments,” *Soft Robotics*, 2022, accepted.
- [211] K. C. Galloway, K. P. Becker, B. Phillips, J. Kirby, S. Licht, D. Tchernov, R. J. Wood, and D. F. Gruber, “Soft robotic grippers for biological sampling on deep reefs,” *Soft robotics*, vol. 3, no. 1, pp. 23–33, 2016.
- [212] W. J. Stewart, I. K. Bartol, and P. S. Krueger, “Hydrodynamic fin function of brief squid, *lolliguncula brevis*,” *Journal of Experimental Biology*, vol. 213, no. 12, pp. 2009–2024, 2010.
- [213] E. Anderson and M. E. Demont, “The locomotory function of the fins in the squid *loligo pealei*,” *Marine and Freshwater Behaviour and Physiology*, vol. 38, no. 3, pp. 169–189, 2005.

- [214] R. O'dor, "The forces acting on swimming squid," *Journal of Experimental Biology*, vol. 137, no. 1, pp. 421–442, 1988.
- [215] E. J. Anderson and M. A. Grosenbaugh, "Jet flow in steadily swimming adult squid," *Journal of Experimental Biology*, vol. 208, no. 6, pp. 1125–1146, 2005.
- [216] E. J. Anderson and M. E. Demont, "The mechanics of locomotion in the squid loligo pealei: locomotory function and unsteady hydrodynamics of the jet and intramantle pressure," *Journal of Experimental Biology*, vol. 203, no. 18, pp. 2851–2863, 2000.
- [217] G. Pawlak, C. M. Cruz, C. M. Bazán, and P. G. Hrdy, "Experimental characterization of starting jet dynamics," *Fluid dynamics research*, vol. 39, no. 11-12, p. 711, 2007.
- [218] I. K. Bartol, P. S. Krueger, W. J. Stewart, and J. T. Thompson, "Hydrodynamics of pulsed jetting in juvenile and adult brief squid lolliguncula brevis: evidence of multiple jetmodes' and their implications for propulsive efficiency," *Journal of Experimental Biology*, vol. 212, no. 12, pp. 1889–1903, 2009.
- [219] D. J. Staaf, W. F. Gilly, and M. W. Denny, "Aperture effects in squid jet propulsion," *Journal of Experimental Biology*, vol. 217, no. 9, pp. 1588–1600, 2014.
- [220] S. Vogel, "Flow-assisted mantle cavity refilling in jetting squid," *The Biological Bulletin*, vol. 172, no. 1, pp. 61–68, 1987.
- [221] C. Wardle, "Limit of fish swimming speed," *Nature*, vol. 255, no. 5511, pp. 725–727, 1975.
- [222] R. A. Jastrebsky, I. K. Bartol, and P. S. Krueger, "Turning performance in squid and cuttlefish: unique dual-mode, muscular hydrostatic systems," *Journal of Experimental Biology*, vol. 219, no. 9, pp. 1317–1326, 2016.
- [223] M. Hermes, M. Ishida, M. Luhar, and M. T. Tolley, "Bioinspired shape-changing soft robots for underwater locomotion: Actuation and optimization for crawling and swimming," *Bioinspired Sensing, Actuation, and Control in Underwater Soft Robotic Systems*, pp. 7–39, 2021.
- [224] F. G. Serchi, A. Arienti, and C. Laschi, "Biomimetic vortex propulsion: toward the new paradigm of soft unmanned underwater vehicles," *IEEE/ASME Transactions On Mechatronics*, vol. 18, no. 2, pp. 484–493, 2012.
- [225] C. Christianson, Y. Cui, M. Ishida, X. Bi, Q. Zhu, G. Pawlak, and M. T. Tolley, "Cephalopod-inspired robot capable of cyclic jet propulsion through shape change," *Bioinspiration & Biomimetics*, vol. 16, no. 1, p. 016014, 2020.
- [226] T. Bujard, F. Giorgio-Serchi, and G. D. Weymouth, "A resonant squid-inspired robot unlocks biological propulsive efficiency," *Science Robotics*, vol. 6, no. 50, p. eabd2971, 2021.

- [227] Z. Yang, D. Chen, D. J. Levine, and C. Sung, “Origami-inspired robot that swims via jet propulsion,” *IEEE Robotics and Automation Letters*, vol. 6, no. 4, pp. 7145–7152, 2021.
- [228] S. Iacoponi, G. Picardi, M. Chellapurath, M. Calisti, and L. Cecilia, “Underwater soft jet propulsion based on a hoberman mechanism,” in *2018 IEEE International Conference on Soft Robotics (RoboSoft)*, pp. 449–454, IEEE, 2018.
- [229] D. Keithly, J. Whitehead, A. Voinea, D. Horna, S. Hollenberg, M. Peck, J. Pikul, and R. F. Shepherd, “A cephalopod-inspired combustion powered hydro-jet engine using soft actuators,” *Extreme Mechanics Letters*, vol. 20, pp. 1–8, 2018.
- [230] C. Christianson, C. Bayag, G. Li, S. Jadhav, A. Giri, C. Agba, T. Li, and M. T. Tolley, “Jellyfish-inspired soft robot driven by fluid electrode dielectric organic robotic actuators,” *Frontiers in Robotics and AI*, vol. 6, p. 126, 2019.
- [231] A. Villanueva, C. Smith, and S. Priya, “A biomimetic robotic jellyfish (robojelly) actuated by shape memory alloy composite actuators,” *Bioinspiration & biomimetics*, vol. 6, no. 3, p. 036004, 2011.
- [232] T. Cheng, G. Li, Y. Liang, M. Zhang, B. Liu, T.-W. Wong, J. Forman, M. Chen, G. Wang, Y. Tao, *et al.*, “Untethered soft robotic jellyfish,” *Smart Materials and Structures*, vol. 28, no. 1, p. 015019, 2018.
- [233] J. O. Dabiri, S. P. Colin, and J. H. Costello, “Fast-swimming hydromedusae exploit velar kinematics to form an optimal vortex wake,” *Journal of experimental Biology*, vol. 209, no. 11, pp. 2025–2033, 2006.
- [234] T. Wang, A. K. Lidtke, F. Giorgio-Serchi, and G. D. Weymouth, “Manoeuvring of an aquatic soft robot using thrust-vectoring,” in *2019 2nd IEEE International Conference on Soft Robotics (RoboSoft)*, pp. 186–191, IEEE, 2019.
- [235] R. Zhang, Z. Shen, H. Zhong, J. Tan, Y. Hu, and Z. Wang, “A cephalopod-inspired soft-robotic siphon for thrust vectoring and flow rate regulation,” *Soft Robotics*, vol. 8, no. 4, pp. 416–431, 2021.
- [236] Y. Luo, Q. Xiao, Q. Zhu, and G. Pan, “Thrust and torque production of a squid-inspired swimmer with a bent nozzle for thrust vectoring,” *Bioinspiration & Biomimetics*, vol. 17, no. 6, p. 066011, 2022.